Automation improvement of indirect gravure printing with a focus on the mechanical characteristics of silicone rubber pads

vom Fachbereich Maschinenbau
der Technischen Universität Darmstadt

zur Erlangung des Grades
Doktor-Ingenieur
(Dr.-Ing.)

D i s s e r t a t i o n

von

Arash Hakimi Tehrani, M.Sc.

Erstgutachter: Prof. Dr.-Ing. Edgar Dörsam

Zweitgutacher: Prof. Dr.-Ing. Eberhard Abele

Darmstadt 2018

Hakimi Tehrani, Arash: „Automation improvement of indirect gravure printing with a focus on the mechanical characteristics of silicone rubber pads“
Darmstadt, Technische Universität Darmstadt,
Jahr der Veröffentlichung der Dissertation auf TUprints: 2019
URN: urn:nbn:de:tuda-tuprints-83222
Tag der mündlichen Prüfung: 12.12.2018

Kurzfassung

Das Hauptziel dieser Dissertation war die Verbesserung der Automatisierungsebene des indirekten Tiefdruckverfahrens. Eine Methode des indirekten Tiefdrucks, der translatorische Tampondruck, wurde in dieser Dissertation als eigenes Druckverfahren betrachtet. Diese Art des Druckens wird zum Bedrucken von 3D-Objekten mit konkaven und konvexen Oberflächen verwendet. Zum Beispiel kann es verwendet werden, um elektrolumineszente (EL) Paneles auf der gekrümmten Oberfläche eines Glases zu drucken. Im ersten Schritt dieser Arbeit wurde die Automatisierungsebene einer indirekten Tiefdruckmaschine verbessert. Hier wurde der Aufbau der indirekten Tiefdruckmaschine nach der Struktur eines mechatronischen Systems klassifiziert. Als Hardwarekomponenten der Steuereinheit wurden National Instruments CompactRio 9074 und Kollmorgen AKD-Servoantriebe benutzt. LabVIEW und DIAdem wurden zur Steuerung des Prozesses und der Überwachung der Datenverarbeitung (online und offline) eingesetzt. Im zweiten Schritt wurde eine Automatisierungsentwicklung durch die Implementierung von Manufacturing Execution System (MES) und Computer Aided Engineering (CAE) erreicht. In diesem Fall wurde das Silikonkautschuk-Materialmodell als hyperelastisches Material für unterschiedliche Härten gemäß Testergebnissen von einachsigen Zug-, Druck- und Planarversuchen für Härten von 3, 6, 12 und 18 Shore A erreicht. Das Silikonkautschuk-Materialmodell wurde für verschiedene Härten verwendet, um Simulationen des Druckprozesses durchzuführen. Außerdem wurde auf Basis mathematischer Gleichungen die Tampongeometrie berechnet. Danach wurde erstmalig ein Tampon-Rechner zur Berechnung der Tampon-Parameter programmiert. Es wurden ein Entwurfsverfahren für ein Tampon und ein kosteneffizientes Verfahren zur Formherstellung eines Tampons erarbeitet. Als innovative Methode wurde ein stereolithografischer 3D-Drucker zur Herstellung der Tampon-Formen verwendet. Diese Methode führte zu einer kosteneffizienteren Formvorbereitung und der Herstellung von einzigartigen Tampons entsprechend den Druckbedingungen. Des Weiteren wurde der Druckprozess in der Finite-Elemente-Methode (FEM) Software ABAQUS simuliert. Dies soll die Optimierung der Druckparameter für unterschiedliche Druckbedingungen ermöglichen. Die Fähigkeit zur kosteneffizienten, individuellen Tampon-Produktion und zur Simulation des Druckprozesses führte zu einer Optimierung entsprechend der Druckbedingungen. Diese Merkmale führten zu einer Erhöhung des Automatisierungsgrads im indirekten Tiefdruck von Stufe 1 (vor dieser Arbeit) auf Stufe 3.

Abstract

The main goal of this dissertation was an improvement in the automation level of the indirect gravure printing process. A type of indirect gravure printing with the name translational pad printing was considered in this dissertation as the printing process. This type of printing is used to print on 3D objects with concave and convex surfaces. For example, it can be used to print electroluminescent (EL) panels on the curved surface of a glass jar. In the first step, the automation level of the indirect gravure printing machine was improved. In this case, the structure of the indirect gravure printing machine was classified according to the structure of a mechatronic system. National Instrument CompactRio 9074 and Kollmorgen AKD servo drives were used as hardwares of control unit. LabVIEW and DIAdem software were applied to control the process and monitoring of data (online and offline), respectively. In the second step, an automation development was achieved according to implementation of manufacturing execution system (MES) and computer aided engineering (CAE). In this case, the silicone rubber material model as a hyperelastic material for different hardnesses was achieved according to test results of uniaxial tensile, compression and planar tests for hardnesses of 3, 6, 12 and 18 Shore A. The silicone rubber material model for different hardnesses was used to perform the simulation of the printing process. Mathematical equations of the pad geometry were calculated. Afterwards, a pad calculator to calculate the pad parameters was programmed for the first time. Also, a designing method of pad and a cost-efficient method for mold production of pad were described. As an innovative method, a stereolithografic 3D printer was used to prepare the pad molds. This method made the mold preparation more cost-efficient than before. So, this feature leads to manufacturing of unique pads according to printing conditions. Further, the printing process was simulated in finite element method (FEM) software ABAQUS. The simulation of the printing process helps to achieve suitable printing parameters for different conditions of printing. The ability of cost-efficient unique pad production and simulation of printing led to optimization of the printing process according to printing conditions. These features led to increase the automation level of indirect gravure printing from level 1 (before this thesis) to level 3.

Acknowledgements

I would like to express my sincere gratitude to my supervisor Prof. Edgar Dörsam, who gave me this opportunity to do present research in IDD (Institut für Druckmaschinen und Druckverfahren, Technische Universität Darmstadt). His guidance supported me in all the time of research and writing of this thesis.

I would also like to kindly thank Prof. Eberhard Abele from PTW (Institut für Produktionsmanagement, Technologie und Werkzeugmaschinen, Technische Universität Darmstadt) as the co-supervisor of my dissertation and his insights in my field of research.

I would like to thank Dr. Jann Neumann and Dr. Dieter Spiehl as my team leaders in the automation and measurement technique group.

Also, special thanks to my colleagues, Dr. Dieter Spiehl and M.Sc. Thorsten Bitsch who their feedbacks on my manuscript helped me to improve the quality of my dissertation.

I am grateful to my colleagues in IDD for their support, specially M.Eng. Christina Bodenstein and M.Sc. Vinzenz Nienhause for useful scientific discussions with them.

In addition, I would also like to specially thank the “Dr. Ing. Wilhelm und Maria Kirmser” scholarship council for their support.

I would like to say my thanks to Mr. Jens-Peter Lück, the directing manager of Tampo-Technik company for the manufacturing of silicone rubber test specimens and pads.

At the end, I would like to acknowledge my family for supporting me spiritually throughout my life.

Table of Contents

Notations

Greek Symbols

Symbol	Unit	Description
ε_a	(-)	Axial strain
ε_t	(-)	Transverse strain to the corresponding for average of test results
α_i	(K^{-1})	Thermal expansion coefficients
ϑ	(-)	Poisson's ratio
$\lambda_1, \lambda_2, \lambda_3$	(-)	Stretch invariants
μ_i	(Pa)	Shear modulus
σ	(Pa)	Stress
$\sigma_i^{avg\_test}$	(Pa)	Stress values in i^{th} element of strain
σ_i^{model}	(Pa)	Stress values in i^{th} element of strain for model results
σ_i^{test}	(Pa)	Stress values in i^{th} element of strain for test results
φ_2	(deg) or (°)	Angle between the plane located on side of the pad and a perpendicular plane to bottom plane of the pad
Ω (r)	(-)	Probability distribution of the molecular chain
Θ_2	(deg) or (°)	Angle located on side of the pad

Latin Symbols

Symbol	Unit	Description
a	(mm)	Pad length
A	(mm)	Length of the narrow part of test specimen
A_0	(mm^2)	Original cross-sectional area of a test specimen
a_1, a_2, a_3	(-)	Nonlinear fitting function indexes

A_1, A_2, A_3, A_4	(mm)	Coordinates of edges of the bottom plane of base segment of the pad
b	(mm)	Pad width
B_1, B_2, B_3, B_4	(mm)	Coordinates of edges of the upper plane of base segment of the pad
c	(mm)	Print area length
C_{ij}	(-)	Material parameters in strain energy function
d	(mm)	Print area width
D_2	(mm)	Coordinate of an intersection point of the arc and surface segments of the pad
D_i	(-)	Compressibility factor
e_0	(J)	Internal energy per unit reference volume
F	(N)	Applied force
G_2	(mm)	Coordinate of the highest point on arc segment of the pad
h	(mm)	Print area height
H	(mm)	Pad height
HA	(Shore A)	Hardness
I_1, I_2, I_3	(-)	Strain invariants
k	(Pa)	Bulk modulus
KB	($J \cdot K^{-1}$)	Boltzmann constant
L	(mm)	Total length of test specimen
MSE	(-)	Mean square error
N	(-)	Chain number in the unit volume
N	(-)	Polynomial order in strain energy function
O	(mm)	Coordinates of center on the bottom plane of base segment of the pad
O′	(mm)	Coordinates of center on the upper plane of base segment of the pad
O″	(mm)	Coordinate of the highest point of the pad
R	(mm)	Amplitude of a point in a polar coordinate system
R_d	(mm)	Displacement in amplitude of a point on the pad surface
R_o	(mm)	Original amplitude of a point on the pad surface

RMSE	(-)	Root mean square error
R-squared (R^2)	(-)	Coefficient of determination
S_0	($J \cdot K^{-1}$)	Entropy per unit reference volume
SS_{reg}	(-)	Summation of square errors
SS_{total}	(-)	Sum of the square deviation around average
T_0	(K)	Reference temperature
Theta	(deg) or (°)	Angle of a point in a polar coordinate system
Theta_d	(mm)	Displacement in angle of a point on the pad surface
Theta_o	(mm)	Original angle of a point on the pad surface
TL	(mm)	Test length of test specimens
TW	(mm)	Test width of test specimen
W	(J)	Strain energy function
W	(mm)	Total width of test specimen
Z	(mm)	Displacement in the Z direction

Abbreviations

Abbreviation	**Description**
2D	Two dimensional
3D	Three dimensional
ABAQUS	A software suite for finite element analysis and computer-aided engineering, from Simulia
ASTM	Association for Testing Materials
CAD	Computer Aided Design
CAE	Computer Aided Engineering
CAM	Computer Aided Manufacturing
cRIO	CompactRio
DIAdem	A software suite for locating, inspect, analyze and report on measurement data, from National Instruments
DIN	Deutsches Institut für Normung

EtherCAT	Ethernet for Control Automation Technology
FEM	Finite Element Method , which is also referred to as finite element analysis (FEA)
HLE	High Level Error
IDD	Institut für Druckmaschinen und Druckverfahren (Institute of Printing Science and Technology), Technische Universität Darmstadt
ISO	International Organization for Standardization
LabVIEW	Laboratory Virtual Instrument Engineering Workbench is a system-design platform and development environment for a visual programming language, from National Instruments
LLE	Low Level Error
MES	Manufacturing Execution System
O_UI	Operational User Interface
Poly	Polynomial
R_Poly	Reduced Polynomial
RTEI	Real-Time Embedded Industrial
RTV	Room Temperature Vulcanized
R-UI	Report User Interface
SC_n	Test specimen number “n” for uniaxial compression test with a hardness of “S”
SP_n	Test specimen number “n” for planar tensile test with a hardness of “S”
SP_UI	Set Point User Interface
ST_n	Test specimen number “n” for uniaxial tensile test with a hardness of “S”
UI	User Interface

1 Introduction

1.1 Motivation

By expanding the use of 3D printers, the importance of printing on 3D surfaces as a post process is increasing. Further, the request to print on non-smooth surfaces in different fields such as printed electronics is increasing which leads to growth of demand for printing on 3D surfaces.

The indirect gravure printing is a printing process where a pad as a transferring part transfers the ink from a gravure printing form to a substrate. In some cases, it is mentioned as pad printing (Hahne, 2001; Kipphan, 2000). It is a fast and cost effective printing method. It is a suitable method to print on 3D objects with uneven surfaces and a large variety of object size. It is an appropriate method to print on the surface of mechanically sensitive objects (TampoCanada, 2018). The indirect gravure printing method has an acceptable accuracy and resolution of 20 µm to print high accurate electronic devices (Pudas et al, 2004). There is a unique feature in the indirect gravure printing, which can print a layer of ink with constant thickness all over the surface with preservation of the 3D objects surface topology. So, the structure of the surface will not be changed after printing (Hahne, 2001). The described abilitities of the indirect gravure printing method lead to use this method widely in different fields such as electrical devices, automotive industry, printed electronics, medical instruments and so on (Golovanov et al, 1996; Hahne et al, 2001; Hakimi Tehrani et al, 2016; Knobloch, 2003; Krebs, 2009; Levassort et al, 2006a; Merilampi et al, 2011; Sharp, 2013; Ye & Zengchao, 2011).

Most of the scientific researches in the field of indirect gravure printing are related to its application to use in functional printing such as printing of solar cells or electroluminescent (EL) on different substrates. There is a lack of literatures especially scientific literatures in the field of its printing process and technology. So, there is a loss of scientific works in this area that should be covered with further scientific researches.

Level 0 to level 4 are five different automation levels to describe the automation condition of a process (Kiel, 2008; Robles et al, 2015; Xenos et al, 2015). The automation level of conventional indirect gravure printing process is located in a low level which is level 0 and level 1. According to the importance of this printing method in recent years which is widely used in scientific and research fields in different industries, the improvement of its automation level has an important role to get better results with more controllability of different printing parameters. Further, it leads to lower production costs and waste production. The role of automation improvement of the indirect gravure printing becomes more important when considering the expensive costs of raw materials in printed electronic devices or the reliability needed when printing biological or medical devices. Further, the repeatability of prints in different iterations with considering the control of the printing parameters in scientific researches are important issues that can be achieved by an automation improvement. So, there is a motivation to improve the automation level.

Further than substrate structure, the parameters with the most effect on the printing process are the force of printing (pad), velocity, ink density and pad hardness (Ücüncü, 2015). The parameters such as pad hardness and force of printing applied by pad relate to silicone rubber pad specifications. So, the silicone rubber pad specifications play an important role in the printing process with high priority in comparison with other printing parameters.

There is a large amount of pads with different geometries, hardnesses and sharpnesses available on the market, but there is no scientific references about the calculation of their structure. For example, the companies Tampoprint, Morlock, and Tampo-Technik are introducing nearly 192, 570, and 984 different types of pads, respectively, and their hardness varies in a wide range (Lück, 2017b; Morlock, 2018; Tampoprint, 2018). Therefore, there is a huge number of options for selecting a pad from different companies and it is very hard to make a decision to choose a pad according to user demands. Because of that, an investigation of mechanical specifications of pads is important to detect the pad behavior in the printing process and choosing the suitable pad.

Briefly, the general goal is the improvement of the indirect gravure printing automation level with a concentration in silicone rubber mechanical characteristics in the printing process. The mechanical characteristics of silicone rubber focus on the mechanical behavior of the silicone rubber pad during the printing process. As part of this

mechanical behavior, the pad surface displacement in different hardnesses and geometries (sharpness) will be discussed.

1.2 Objectives

In this dissertation, the general goal is the improvement of the indirect gravure printing automation level with a concentration on silicone rubber mechanical characteristics in the printing process. A pad, as part of the printing unit, has a duty of ink transferring in the printing process. The optimization and control of mechanical behavior of the pad affect on the optimization of the printing process which is one part of automation improvement in the indirect gravure printing process.

According to this goal, two challenging questions arise in the mind. First, is it practicable to improve the automation level of indirect gravure printing in the described direction? Second, is it possible to investigate the mechanical behavior of pad in the printing process?

To find the answer of the second question, the simulation of printing process will be used in this dissertation. To simulate the printing process some questions come up. What are the mechanical characteristics of the material of the pad (silicone rubber)? What is the geometry of the pad? Or how should the pad geometry and model be designed? The response to these questions makes it possible to simulate the printing process. The mechanical behavior of the pad can be investigated by use of the simulation results.

1.3 Overview of the dissertation

The chapters are structured according to the steps of improvement of the automation level of indirect gravure printing process.

In chapter 2, the general information about indirect gravure pad printing and pad features are explained. Further, the classification of direct and indirect gravure printing and state of the art in the automation level of indirect gravure printing are described in this chapter.

In chapter 3, the development of indirect gravure printing machine is presented. It is developed to improve the automation level of indirect gravure printing machines. In this

chapter, the printing machine structure is classified as a mechatronic system. Then, software, controller, actuators and sensors are developed in this structure.

In chapter 4, the silicone rubber characteristics are explained. It is used in the simulation process to define the material properties. Here, the mechanical testing methods are described. Then, after explanation of measurement setup, the test results are achieved. Afterwards, the silicone rubber material model for different hardnesses are attained.

In chapter 5, a method to design the pad geometry is presented for the first time. It is needed to design unique pads. Further, it is required in the simulation process to define the pad geometry as a part. The mathematical equations for designing a rectangular pad are calculated. Thereafter, they are applied to design four pads with different heights. In this chapter, a production method to manufacture molds of pads by use of stereolithografic 3D printer is explained. Then, the pads are manufactured. They are applied in chapter 6 to perform experiments and validation of simulation results.

In chapter 6, the simulation of the indirect gravure printing process is described. The printing process is simulated to investigate the mechanical behavior of the pad with the goal of optimization of the printing process. Here, the printing process for four different pads with four different hardnesses are executed. The effect of the pad height in different hardnesses on the displacement of pad surface is considered as a case study in this chapter. Then, the role of simulation of the indirect gravure printing process for the improvement of automation level is explained.

In chapter 7, the dissertation closes with a brief conclusion containing the scientific outputs. Here, the automation level improvement of printing process is summarized by considering the developments performed in this dissertation. Further, some ideas for future works as an outlook are explained.

2 Fundamentals

The fundamentals contain the theoretical and basic issues of this dissertation. First, the state of the art in the indirect gravure printing with a focus on the classification of gravure printing technology, basics of translational pad printing and its automation level are described. Second, it concentrates on the silicone rubber pad used in indirect gravure printing. It elucidates the silicone rubber pad features which are the material, hardness, shape and surface tension.

2.1 State of the art of indirect gravure printing

In this part, a general description about gravure printing process is presented. Then, a translational pad printing process is described in detail as the printing method in this dissertation. Finally, current automation level of translational pad printing will be introduced as part of the state of the art of translational pad printing.

2.1.1 Classification of gravure printing technology

Gravure printing is a technology which a motif is engraved into the surface of a printing form (Kipphan, 2000). So, the name of this technology comes from the printing form structure. The gravure printing is divided into two types of direct gravure printing and indirect gravure printing.

A gravure printing form transfers directly the ink to the substrate in the direct gravure printing. A rotogravure printing with a cylindrical printing form is introduced in (Kipphan, 2000) as a direct gravure printing technology.

In the indirect gravure printing, the gravure printing form transfers indirectly the ink to the substrate by use of an intermediate carrier. The indirect gravure printing is divided into two types according to its intermediate carrier. They are gravure offset printing and pad printing which their intermediate carriers are blanket and pad, respectively.

There are different types of gravure offset printing such as soft blanket gravure offset printing or SBG (Izumi et al, 2018), roller gravure offset printing (Shen et al, 2017) and plate to plate gravure off set printing (Konami et al, 2017; Taik-Min et al, 2010).

The pad printing can be divided to rotary pad printing (Kipphan, 2000), round pad printing (Micro Print, 2012) and translational pad printing. This classification is achieved according to the type of motion of a pad to transfer the ink on the substrate as an intermediate carrier. The motion of pad is rotational in the rotary and round pad printing process and the pad type is called roller type. The translational pad printing process executes with a translational motion of pad for ink transferring. In this case the pad types are classified into round, rectangular, saddle, longitudinal and special forms.

The indirect gravure printing has a unique advantage in comparison with the direct gravure printing. It is its ability to execute the printing process without pressing the substrate against the hard gravure printing form (Pudas, 2002). It prevents damage to the surface of sensitive substrates.

The different types of gravure printing can be used to print on planar substrates (Ga Eul et al, 2016; Konami et al, 2017; Pudas et al, 2004). The SBG gravure offset printing can be used to print on some types of non planar substrates (Izumi et al, 2018), while pad printing can be used to print on different types of non planar substrates such as concave or convex surfaces. So, the ability of printing on different types of non planar and curved substrates is the unique feature of pad printing process.

The round pad printing is used to print around the substrate with a cylindrical geometry. The rotary type is useful to print on large quantities of substrates with special and similar forms. It is usually applied to print on moving substrates while the translational type is used for stationary substrates (Kipphan, 2000; Putnam et al, 1988).

Table 2-1: The characteristics of three different pad printing types, the rotary, round and translational. It compares motion of printing parts in the rotary, round and translational pad printing methods during the printing process.

Printing parts	Rotary pad printing	Round pad printing	Translational pad printing
Pad	Rotational motion	Rotational motion	Translational motion
Printing form	Rotational motion	Translational motion	Translational motion
Substrate	Translational motion	Rotational motion	Stationary

Table 2-1 presents the motion of printing parts in the rotary, round and translational types of pad printing methods. The printing parts are pad, printing form and substrate. The pad and printing form motion in rotary type are rotational in two different directions and the substrate has a linear motion. In round pad printing type, the pad moves rotationally on the printing form and then transfer the ink on the substrate with a rotational motion. A printing around the substrate surface is performed by rotationally motion of the substrate during printing. In this case, the printing form table with a planar geometry has a translational motion. In the translational pad printing method, the pad and printing form motion are linear and translational. In translational type, usually, the substrate is fixed. This dissertation will focus on the translational pad printing between the described methods in above. In this dissertation, translational pad printing is called indirect gravure printing because translational pad printing is a type of indirect gravure printing.

2.1.2 Basics of translational pad printing

There are only a few ways to print on very rough substrates or substrates with concave or convex surfaces and it is still a challenge to print on complex 3D shaped surfaces. One possibility is the indirect gravure printing technique (Krebs, 2009).

More than 200 years ago, hand transfer printing as the first generation of the indirect gravure printing method was used to print on plates and dinnerware for the first time (DECO, 2018). Later the first mechanical type of printing tool was used to print watch faces. Thereafter, the mechanical type of indirect gravure printing machine was developed for the first time to print the doll's eyes (DECO, 2018).

Figure 2-1 shows translational indirect gravure printing elements. The printing form, printing form table, doctor blade, ink cup, pad and substrate are displayed here. The printing form and pad motion directions during printing process are mentioned in the figure. Printing steps in the translational type of indirect gravure printing process will be described at the end of chapter 3.1 in detail.

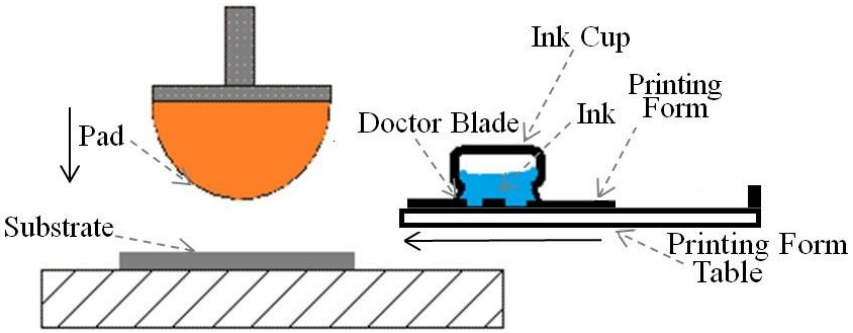

Figure 2-1: The schematic illustration of a translational pad printing elements. The important elements of a translational type are doctor blade, printing form and pad. The arrows show the motion direction of the pad and the printing form table during ink transferring.

According to the type of ink system (inking unit), the indirect gravure printing is divided into open and closed systems which are presented in Figure 2-2. The open ink system is the classical method of inking system. In this system the used solvents have a higher evaporation rate because of the direct contact of ink with the surrounding atmosphere. That leads to less control of the ink viscosity. In closed systems, the ink cup is completely sealed and the solvent evaporation rate is smaller compared to an open system (Hahne, 2001; Kipphan, 2000).

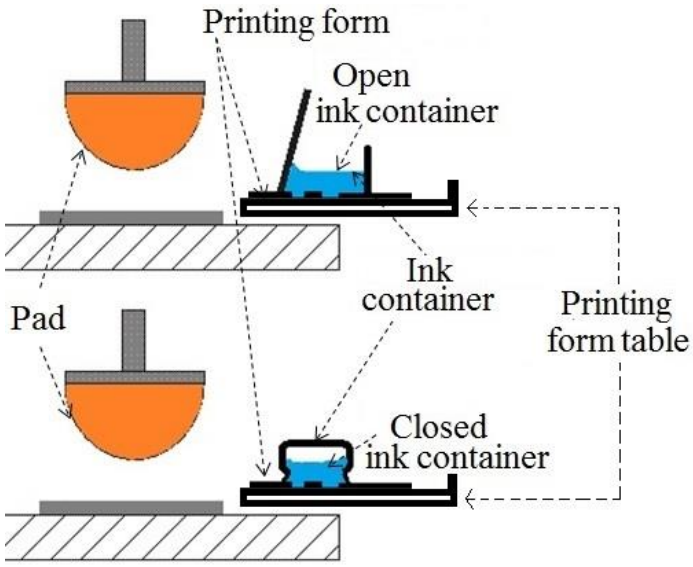

Figure 2-2: The open (above) and closed (below) inking systems are presented here. In the open inking system, the ink in the ink container is in contact with the outside air of the ink container.

A competitive advantage of indirect gravure printing that separates it from other methods of printing is its ability to print on substrates with high variation of shapes, roughness, fragility, thicknesses and dimension. For example, Figure 2-3 displays the

result of the indirect gravure printing method in the field of printed electronics to print electroluminescent (EL) films on curved surfaces with different mechanical features such as glass and conductive copper surfaces.

(a) (b)

Figure 2-3: The printed electroluminescent (EL) panels by the use of indirect gravure printing. (a) shows a printed EL panel on a curved surface of a glass jar. (b) shows a EL display in a capacitive sensor which was printed with an indirect gravure printing technology. The figures were presented in (Bodenstein, 2018; Bodenstein et al, 2018).

Figure 2-4 shows the print results on different types of material with different mechanical features, like glass as a fragile and smooth substrate, stone as a very hard and rough substrate and 3D printed polylactic acid (PLA) parts. It is the practical advantage of indirect gravure printing in comparison with other methods to print on a wide range of 3D substrates.

Figure 2-4: The samples with different mechanical features printed on by the use of indirect gravure printing. The substrates materials are fragile glasses with smooth surfaces, hard stones with very rough surfaces and 3D printed objects made of PLA. The printed elements are letters, logos, numbers, high accurate beakers marked lines and fine lines with different thicknesses.

In addition to usual cases, the indirect gravure printing is used in some unique fields. For example, to print 40 micrometers thick piezoelectric films on a cylindrically-concaved substrate in the field of medical imaging (Levassort et al, 2006b; Li et al, 2017) and print gas sensors (Golovanov et al, 1996) and flexible sensors (e. g. micro-Fluxgate sensors) (Schoinas et al, 2017). Because of its unique abilities, indirect gravure printing gained a big part of the screen printing and hot stamping markets within the last 50 years (DECO, 2018).

2.1.3 Automation levels

Automation has the goal of decreasing human's role in the production process, to improve the process efficiency, and to decrementing the production losses, usually by the use of a process control system (Azolibe et al, 2015; Hakimi Tehrani et al, 2016). The use of automation in the production process optimizes manufacturing with lower cost, higher quality, increased accuracy in process, and shorter production time (Araújo et al, 2018).

Figure 2-5 shows automation levels in an automation pyramid. There are four different levels in an automation pyramid.

According to (Kiel, 2008; Robles et al, 2015; Xenos et al, 2015) the different levels of the automation pyramid are described in following. Level 0 is reached when the sensors and actuators are used to control the system. The system signals are processed and controlled in the field level (level 1). The process monitoring and interface issues are related to level 2 (cell level). In some cases, the level 0 till level 2 consider in the same level. Then, the dashed lines are used in Figure 2-5 to clarify this issue and make this model more comprehensive.

Level 3 (plant level) is related to optimization of production processes by use of manufacturing execution system (MES) and Management information system (MIS). The production control and programming at a company level, such as enterprise resource planning (ERP) are performed at level 4.

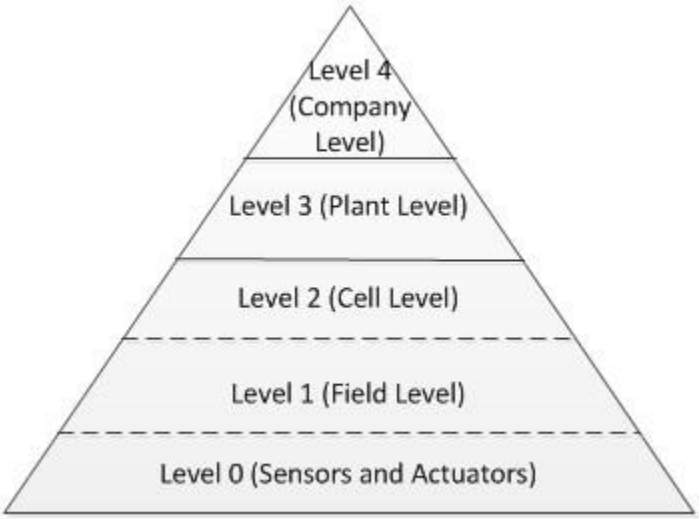

Figure 2-5: The automation pyramid. There are four different levels in above automation pyramid. The automation levels start from level 0 (the lowest level) and can be developed till level 4 (Highest level). This figure is based on (Kiel, 2008; Robles et al, 2015; Xenos et al, 2015).

Level 0 is the base level and level 4 is the top level. The method to reach higher levels is completely different in different processes and systems. In some cases, it is very hard, or impractical to get into a higher level.

As described in (DECO, 2018; Micro Print, 2012), a hand transfer printing was the first type of indirect gravure printing machine to print on plates (more than 200 years ago). It was working without any sensors and actuators and it did not provide the preliminary necessities to get the level 0. So, the first generation of indirect gravure printing machine had no automation level (lower than level 0). Later, the first industrial type which was used to print watch faces was designed with mechanical parts such as springs. In this type, the human hand applied the force to move the pad axis, but it came back to the origin with spring force. So, it had no automation level. Afterwards, the first automated type was designed by use of actuators and pneumatic force to move the axes. Hence, it got the automation level 0.

Nowadays, sensors, actuators and controller devices such as programmable logic controllers (PLCs) are used in most conventional indirect gravure printing machines. The controllers control the maximum position of the pad for printing (Micro Print, 2014; Morlock, 2012; Tampoprint, 2014). Recently, a new type was designed with ability of speed control and save the set point values (Kuscharski, 2017). The new generation of indirect gravure printing machines reached the level 1 according to their

components. Because they do not monitor the printing process, their automation level was not increased to level 2 until now.

2.2 Silicone rubber pad features

In the indirect gravure printing method, a pad is an ink transporter from printing form to the substrate. The pad is an influential parameter in the indirect gravure printing process (Ücüncü, 2015).

2.2.1 Current condition of pads

Nowadays, there is a large amount of different pad types which are manufactured in different companies. For example, in the pad catalogue of Morlock company, more than 570 different types of pads are listed and the hardness of each can be selected. Hardness variation reaches from 2 to 24 Shore A and their material color can be chosen between red and orange. So, only one single company offers more than 13680 different product options (Morlock, 2018). Tampoprint company offers more than 192 different types, in 5 different hardnesses and 4 different materials. The total amount of pads is more than 3840 options (Tampoprint, 2018). Tampo-Technik company have designed more than 984 different pad types with hardness sets up to 25 Shore A (more than 12 different hardnesses) and 4 different materials. The total amounts of pads in Tampo-Technik company are more than 47232 different options (Lück, 2017b). It should be mentioned, the pad types and shapes vary in different companies. Usually, the dimensions of different companies pads are not equal. So, here the different material, hardnesses and shapes of pads are described and arranged to sort the structure of pad parameters.

2.2.2 Design

A pad is mounted on a base plate in its production process. The base plate material is aluminium or wood (Tampoprint, 2018). There is a hole in the base plate called pad fixture. The pad is assembled on the indirect gravure printing machine by means of a pad fixture. Figure 2-6 shows the elements of a pad.

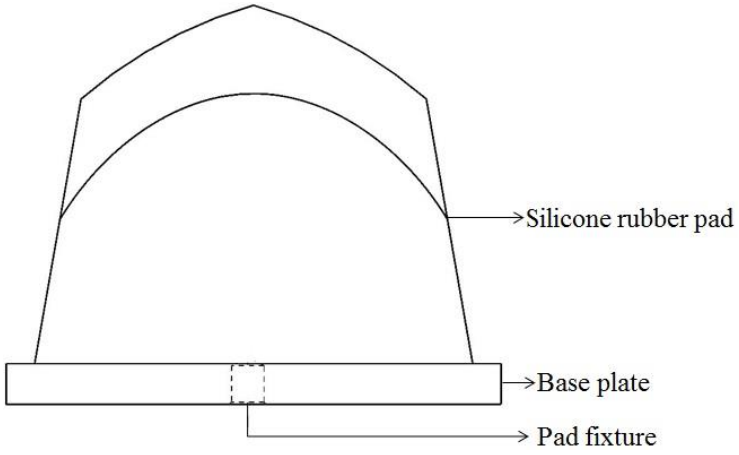

Figure 2-6: The schematic illustration of pad elements.

The inside of a pad can be completely full or can be designed with an internal hole. A pad with an internal hole is called hollow pad (Lück, 2017a).

A top view of a pad form is called pad shape. The pad shape is affected by two important parameters. They are pad angle (from side to print area) and pad surface (Proell, 2014). Figure 2-7 (2) shows the pad angle (Θ), pad length (a), pad width (b), print area length (c), print area width (d). A pad surface is the surface over the print area (c and d) which was highlighted by orange color. The print area is related to the pad surface according to solid geometry.

Different references and producers define their own names for pad types according to pad shapes, but all the concepts are the same. For example (Anon., 2014) says that all common pads types should be divided into cylindrical, square, linear or compound. According to this, a shape of a pad from top view is divided into round (circle) and rectangular shape as the most common shapes and also other formats. Generally, it can be concluded that the pad shape can be divided into five groups. They are called round, rectangular (and/or square), saddle (oval or fish belly), longitudinal and special form (such as keyboard form) (Lück, 2017b; Morlock, 2018; Tampoprint, 2018).

The approximate distributions of different groups of pad shapes (rectangular, longitudinal, round, saddle and special forms) are nearly 34%, 32%, 18%, 8% and 8% (respectively) of total introduced pads in companies' sales pitch. These values were approximately calculated according to distribution of different groups of pad shapes in (Lück, 2017b; Morlock, 2018; Tampoprint, 2018) companies' sales pitch.

Figure 2-7 shows samples from different groups of pad shape. Usually, the group name comes from the pad base geometry. Also, it can be concluded that the longitudinal shape group is one of the other shape groups (usually rectangular) which extended in the horizontal direction in its design process and it can be ignored in the group assortment and the number of groups can be limited to four different groups.

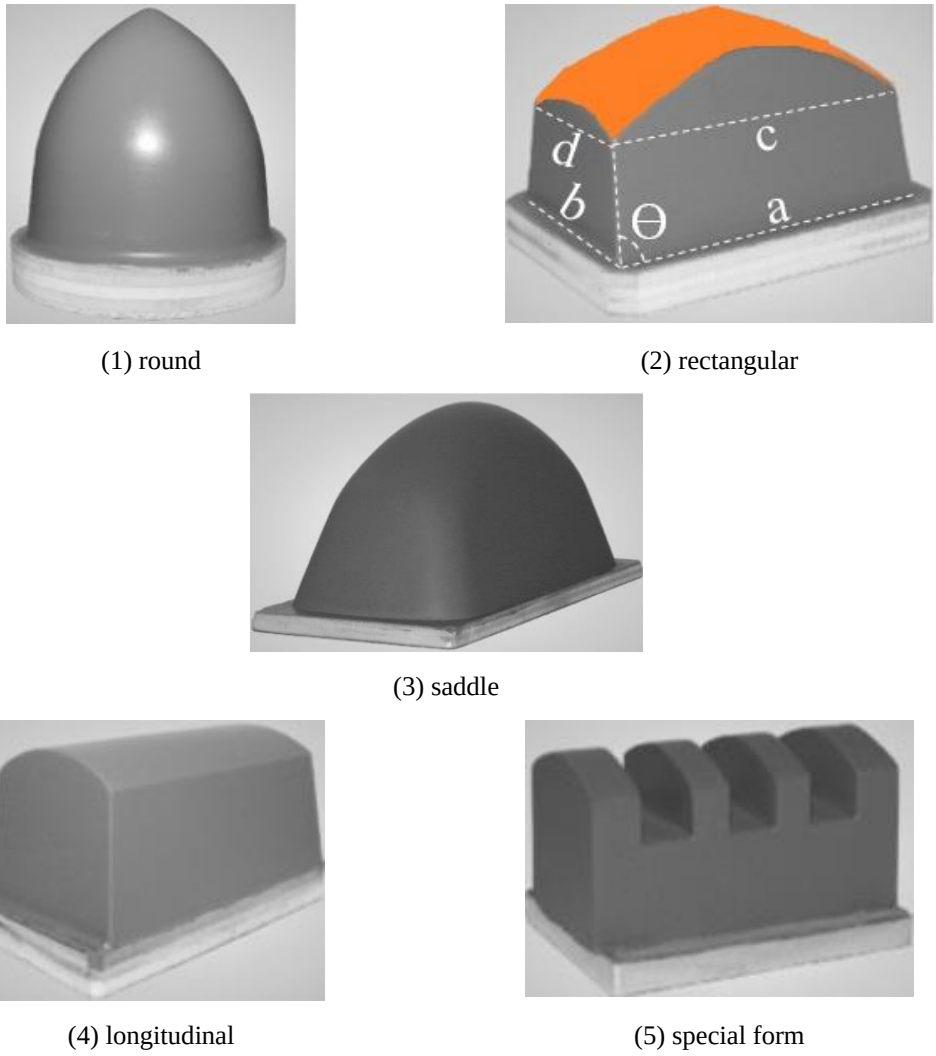

(1) round (2) rectangular

(3) saddle

(4) longitudinal (5) special form

Figure 2-7: The samples from different groups of pad shape (Lück, 2017b). The pad shape is divided into five different groups. They are round, rectangular, saddle, longitudinal and special form which are clarified with (1), (2), (3), (4) and (5) numbers, here. The pad base and surface geometry lead to their group name. As an example, the pad surface (orange color), pad angle (Θ), pad length (a), pad width (b), print area length (c) and print area width (d) of a rectangular pad were highlighted in segment (2).

The pad size is a parameter of the pad which gets affected by the pad shape. It has a big influence on print results. The pad size should be as large as possible and the print

results of bigger pad are more accurate, based on the experts' experience in the indirect gravure printing (Anon., 2014). It is recommended to choose pad dimensions at least 10-20% greater than printing form motif (Anon., 2014).

A pad which its surface is flatter than another, is more prone to electrostatic problems in the printing process. For example, in Figure 2-7, the pad surface in (4) is flatter than the pad surface in (1). So, more electrostatic problems can be observed when the pad in Figure 2-7 (4) is used to print in comparison with the use of the pad in Figure 2-7 (1). The electrostatic problem can be recognized as the ink spreads around of the printed image, which is called hair effect in print results in some cases. The electrostatic effect between the pad surface and ink causes this problem. More curvature in the pad shape can be one of the solutions to solve the electrostatic problem during print (Lück, 2017a). Sometimes, steeper pads need to be pressed more and it leads to displacement errors in the center (Lück, 2017a). In addition to above issues, it is important to mention that there are different limitations to select a pad such as maximum pad height, size and substrate material.

The pad shape depends on the substrate’s shape. In the following, some of the experimental cases which are related to this issue are described. To print on the edge of a substrate, a tapered pad (very high hardness e.g. 18 Shore A) with bevel edge of nearly 45 degrees is suggested. For printing in a deep concave substrate, the pad diameter should become slightly smaller. To print ring shapes, the pad should be hard (e.g. 12 Shore A). In this case, the sides of the pad print the motif and the pad tip should not be sharp and a concave structure of the pad surface is preferred. Spherical substrates need round pads because of their symmetric shape. In this case, a pad with a cavity in the tip is suggested. A bigger pad which is soft or very soft should be selected. For structured substrates harder pads and sharper pads are more effective (Lück, 2017a).

Recently, hollow pads were introduced to market. The hollow pads with longitudinal or transverse holes reduce the contact pressure on the substrate and thus additionally protect mechanically sensitive products. This type of pad is useful for strongly curved substrates, because of the hollow structure, the pad tip goes back easier and the pad behavior in printing seems the same as the pad behavior with lower hardness. This method is possible for different shape groups of pads (Lück, 2017a).

2.2.3 Material

In the 18th century, the pad material was gelatin (made from bone meal) to transfer the ink. Nowadays, the room temperature vulcanized (RTV) silicone rubber is used. (DECO, 2018; Lück, 2017a; Micro Print, 2012). Normally, the based silicone rubber and silicone oil get mixed to produce the pads. Manufacturers present pads with different hardnesses by unit of Shore A to distinguish between the different mixtures of the based silicone rubber and silicone oil. Shortly, the pad material is called silicone rubber with a Shore A hardness.

Adding the silicone oil to silicone rubber raw materials before vulcanization decreases the hardness of the final product (silicone rubber) to a value less than the maximum hardness. Table 2-2 presents the relation of added silicone oil in final product hardness. In this case, the maximum hardness is 31 Shore A, and adding of silicone oil changes it to lower hardnesses. These data are related to a special product of Wacker company (Wacker, 2018) and is described here only as an example.

Table 2-2: The example for effects of the silicone oil percentage on silicone rubber hardness (Wacker, 2018).

Silicone oil (%)	0	30	50	70	100	120
Shore A	31	14	8	4	1	0

Some silicone rubber producers present two-component silicone rubber that vulcanizes at room temperature (Wacker, 2018). This type of silicone rubber after vulcanization without adding any silicone oil leads to a final product (silicone rubber) with a maximum Shore A hardness.

Sometimes anti-static silicone rubbers are used to avoid static charging when the print results with normal pads are not suitable. It should be considered that the anti-static pads are not the unique solution to solve this problem. Other parameters such as humidity, ionized air, pad shape, ink viscosity and ink type effect on the static charging (Lück, 2017a).

2.2.4 Hardness Shore A

Shore hardness, named after Albert Ferdinand Shore, is a unit to define the material hardness (Anon., 2018). It is mainly used for elastomers and rubber elastic polymers. It is directly related to the penetration depth. There are different types of Shore such as A, C and D. Shore A is suitable for soft rubber and Shore C and D are applied for elastomers and soft thermoplastics (Anon., 2018). There are ISO 868, DIN 53505 and ASTM 2240 standards to measure the hardness of materials. Their differences were described in (Anon., 2018). In this dissertation the ASTM D2240 standard (ASTM D2240, 2015) are used. Different methods of hardness measurement are described in ASTM D2240 (2015). The common measurement unit of pad hardness is Shore A. Figure 2-8 shows the hardness measurement device (Durometer) of type A. The indentor test height is 2.5 mm and the contact diameter is 0.79 mm. A spring connects the indentor to indicator. The spring calibration tolerance is ±1 Shore A. The described indentor should be pressed on a test specimen vertically. A sufficient pressure should be performed on the test specimen to create a firm contact. It is recommended to affix a load of 1 kg to the durometer to improve repeatability of measurements (ASTM D2240, 2015). The load is used to become sure about the complete connection between a presser foot and the test specimen surface. So, Durometer is pressed on the measurement surface in perpendicular direction. Afterwards, this situation is kept constant for a while which is called holding time. A holding time of 1 ± 0.1 s is used to read the Durometer value. The holding time can be changed according to the agreement between supplier and user (ASTM D2240, 2015). It is recommended to select a test specimen with a thickness of more than 6 mm (ASTM D2240, 2015). The equation (2-1) shows the relationship between measured Shore A hardness (HA) and the applied force on the spring (F) during the test for the indentor type A. More detailed data about the test can be achieved in the ASTM D2240 standard (ASTM D2240, 2015).

$$HA = \frac{F - 0.55}{0.075} \tag{2-1}$$

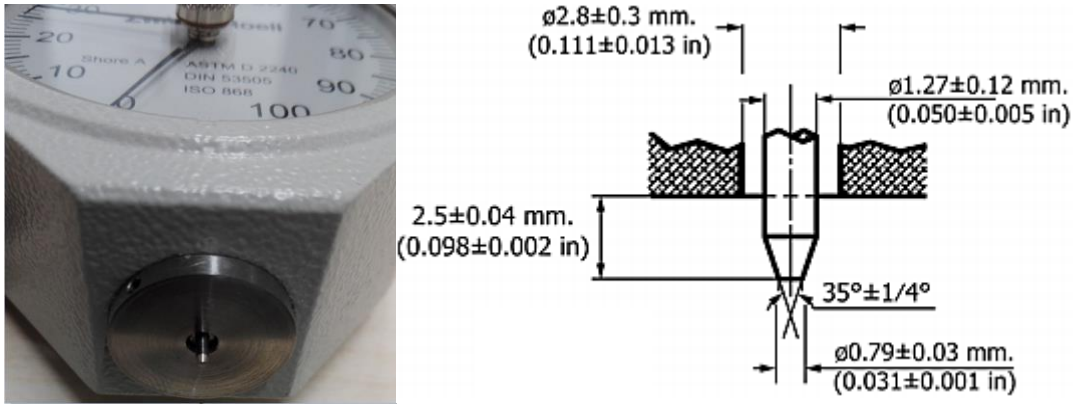

Figure 2-8: The hardness measurement device (durometer) type A (ASTM D2240, 2015). The indentor shape and dimensions are clarified here. It is pressed vertically on the test piece to measure the Shore A hardness. The hand held gauge durometer is shown here.

The pad hardness influences printing force and ink transferring to the substrate. Based on the experts' experience in the indirect gravure printing, usually, the print results of stiffer (harder) pads are more acceptable than others (Lück, 2017a). The pads with hardness ranges of 0 to 5, 6 to 11 and higher than 12 Shore A can be described as soft, medium and hard pads. A harder pad is more precise and a softer pad transfers more ink. The unit of hardness is Shore A that for very soft pads (less than 0 Shore A) is changed to Shore 00. For example 25 Shore 00 is considered as a very soft pad (less than 0 Shore A) (Lück, 2017a).

But also the substrate features limit the selection of pad hardness. For example, to print on a substrate with high grade of fragility the pad hardness must be less than the substrate with low fragility grade. Further, pad hardness selection has a relationship with substrate shape and roughness. For instance, softer pads (less hardness) are selected to print on sphere substrates, while harder pads are used to print on structured substrates. Consequently, it effects on ink transferring and print results (Lück, 2017a; Proell, 2014).

2.2.5 Surface tension and wettability

A low surface tension of the pad will effect on better ink transfer to the substrate (Hahne et al, 2001). The better ink transfer does not mean transfer more ink. It means getting the appropriate amount of ink from the printing form and transfer the achieved ink to

the substrate completely. A complete ink transferring by a pad, leads to a complete printing of a motif area on the substrate.

The surface tension is directly affected by the amount of silicone oil in the pad. The surface tension is related to the percentage of silicone oil on the surface and its affect is investigated by contact angle of a liquid (e.g. water) on the pad surface (Hahne et al, 2001).

Beside the surface tension, the silicone oil effects the hardness of the pad, too. According to this issue, the diagram of pad hardness and surface tension changing in comparison with silicone oil percentage is shown in Figure 2-9.

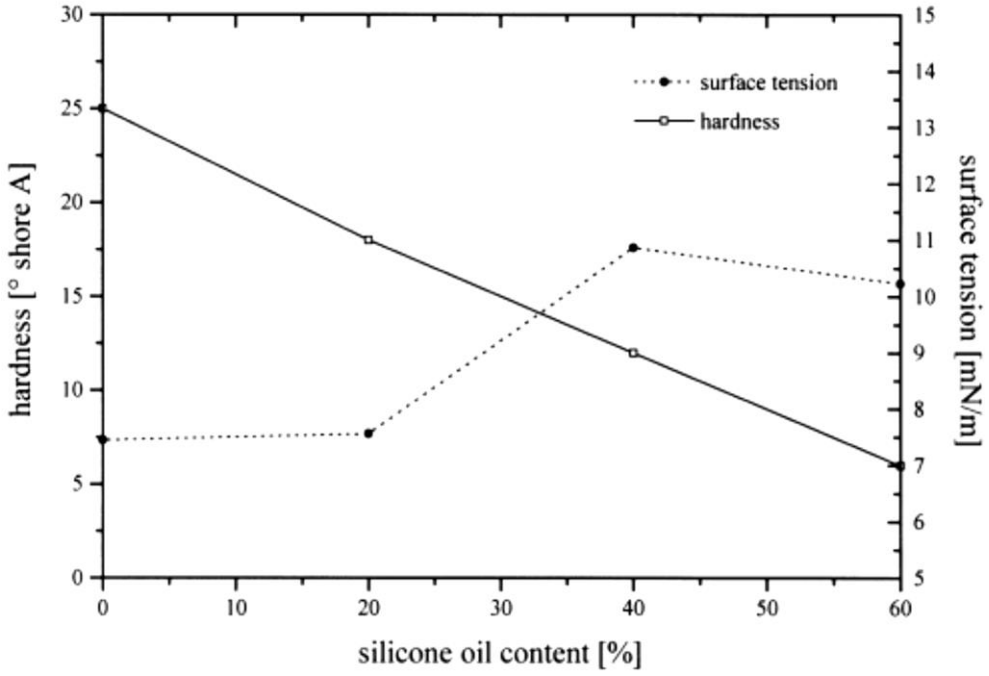

Figure 2-9: The influence of silicone oil percentage on hardness and surface tension of a pad. The solid line and dotted line relate to hardness and surface tension. The left and right vertical axes display the hardness and surface tension. These curves are experimental results described in (Hahne et al, 2001).

According to the diagram in Figure 2-9, increasing of silicone oil percentage decreases the hardness. But the surface tension does not have such a linear behavior. Till adding nearly 20% silicone oil, no changes appears in the surface tension. Then, adding up to 40% silicone oil increases the surface tension and augmenting more than this amount will slightly decrease the surface tension.

2.3 Hyperelastic material model of silicone rubber as a pad material

The pad material is silicone rubber. Silicone rubber is a hyperelastic, isotropic and incompressible material with a relatively low elastic modulus and high bulk modulus (Amabili et al, 2016; Mansouri et al, 2017; Simulia, 2013b). In the following, the hyperelastic material model is described in detail.

2.3.1 Hyperelastic material model

The strain energy function is used to describe the constitutive model of silicone rubber. The strain energy function is divided into two general types of statistical (micromechanical) models and phenomenological models, which are described in (Fahimi et al, 2018; Steinmann et al, 2012) and an overview with relation to this work is given here. The statistical models come from the molecular network theories. So, the parameters of the statistical model describe the molecular quantities. The most important statistical models are 3-chain, 8-chain, and unit sphere. The phenomenological models are described with strain or stretch invariants. The phenomenological model parameters are achieved by different material tests such as uniaxial tensile test, compression test and so on. The phenomenological models are functions of principal stretches or strain invariants. So, there are two general types of phenomenological models. The Ogden models are principal stretches formulated models and models such as Neo Hooke, Mooney-Rivlin, Yeoh, Arruda-Boyce and others are strain invariants formulated models (Steinmann et al, 2012) which will be described in 2.3.2.

According to (Fahimi et al, 2018), the structure of statistical models in comparison with phenomenological models is too complicated to find the model parameters and closed form solution. So, the statistical model is usually not used to solve the numerical problems and the phenomenological models are more useful in this case. So, the phenomenological models are often used in finite element method (FEM) to solve the numerical problem for simulation of the hyperelastic material model.

Hyperelasticity is a useful model to investigate the behavior of rubbers in the large scale deformation regime. Briefly, this model can be considered as a non-linear elasticity (Bergstroem, 2015).

The hyperelasticity model is defined as a function of strain energy. In this model, the Helmholtz free energy per unit reference volume (equation (2-2)) is considered as the energy function which is described in (Bergstroem, 2015) and here an overview with relation to this work will be given. Equation (2-2) describes the energy in parameters of internal energy per unit reference volume (e_0), entropy per unit reference volume (S_0), and reference temperature (T_0). The entropy is the amount of energy in the system that is not changed to work. Equation (2-3) shows the entropy function which is calculated with statistical mechanics according to the molecular chain of material. It is related to the chain number in the unit volume (N), KB as a constant value $1.38 \cdot 10^{-23}$ J/K, and the microscopic configuration Ω (r) which is the probability distribution of the molecular chain end to end distance. Some works in the past (Flory & Volkenstein, 1969; Kuhn & Grün, 1942) describe the calculation methods of Ω. The entropy part of the energy function usually is used in the statistical (micromechanics) model of hyperelastic material with omitting of the internal energy (e_0) effect, because links of the molecular chain model are rigid. So, in this case the applied energy and force only stretches the molecular chain to a special amount of the end to end interval. Similarly, in the phenomenological model because of the focus on the deformation of material in the large scale, the small amount of micromechanic model effects in the energy function is ignored (Bergstroem, 2015). Then, in the following, the entropy part of the energy equation (T_0S_0) is ignored.

$$W = e_0 - T_0 S_0 \tag{2-2}$$

$$S_0 = NK_B ln\Omega \tag{2-3}$$

Equations of this part are based on (Bergstroem, 2015) and other references (that are mentioned in the text). Equation (2-4) describes the Cauchy stress of thermoelastic materials which is a function of the temperature (T_0) and the deformation gradient (F) (Bergstroem, 2015). The deformation gradient describes the current stretch configuration in comparison with the reference (initial undeformed) state. In this equation, the $W(F,T_0)$ is the Helmholtz free energy (strain energy) which is described in different forms and it will be discussed in details later. The parameter J is the Jacobian determinant which is calculated with the det [F], here. The parameter F^T is the transpose of F.

It is important to mention that the deformation gradient classifies the body deformation in different types. There are homogeneous, inhomogeneous, and isochoric deformations. In the homogeneous deformation, the deformation gradient does not change in different positions of the material. In the inhomogeneous deformation, the deformation gradient varies in different positions of the material. The deformation is isochoric or volume preserving when the deformation gradient determinant or J value is equal to one (Bergstroem, 2015).

The Cauchy stress can be explained in the functional form of equation (2-5) according to right stretch tensor (U) and right Cauchy Green tensor (C). R is a rotation tensor. So, equation (2-5) is inserted into equation (2-4) to get equation (2-6) (Bergstroem, 2015).

$$\sigma(F,T_0) = \frac{1}{J}\frac{\partial W(F,T_0)}{\partial F}F^T \tag{2-4}$$

$$\sigma(F) = R\sigma(U)R^T = R\sigma(C)R^T \tag{2-5}$$

$$\sigma(U,T_0) = R(\frac{1}{J}\frac{\partial W(U,T_0)}{\partial U}U^T)R^T \tag{2-6}$$

Equation (2-7) describes the relationship between the Helmholtz free energy partial derivative of U and C. This theorem was clarified in (Bergstroem, 2015). The result of inserting equation (2-7) into equation (2-6) leads to equation (2-8).

$$\frac{\partial W(U)}{\partial U} = 2U\frac{\partial W(C)}{\partial C} \tag{2-7}$$

$$\sigma(C,T_0) = \frac{2}{J}F\frac{\partial W(C,T_0)}{\partial C}F^T \tag{2-8}$$

The energy function is a function of the principal stretch (equation (2-9)) or strain invariants (equation (2-10)). Equation (2-11) shows the general equation of the strain energy function.

W is the strain energy function. $\lambda_1, \lambda_2, \lambda_3$ are principal stretch invariants and I_1, I_2, I_3 are strain invariants. The relationship between the strain invariants and the principal stretches is described in equations (2-12) - (2-14). Function $f(I_1, I_2, I_3, ...)$ describes the incompressible part and $g(K, ...)$ the compressible part which is a function of the bulk

modulus K. Because silicone rubber is an incompressible material function g becomes $g(K,...)=0$ and $I_3=1$ (Hoss & Marczak, 2010).

$$W=W(\lambda_1,\lambda_2,\lambda_3) \tag{2-9}$$

$$W=W(I_1,I_2,I_3) \tag{2-10}$$

$$W=f(I_1,I_2,I_3,...)+g(K,...) \tag{2-11}$$

$$I_1=\sum_{i=1}^{3}\lambda_i^2 \tag{2-12}$$

$$I_2=\lambda_1^2\lambda_2^2+\lambda_2^2\lambda_3^2+\lambda_3^2\lambda_1^2 \tag{2-13}$$

$$I_3=\prod_{i=1}^{3}\lambda_i^2 \tag{2-14}$$

Equation (2-15) explains the stress as a function of strain invariants. So, in this case the energy function of equation (2-10) is used to derive equation (2-15) from equation (2-8).

$$\sigma(I_1,I_2,I_3,T_0)=\frac{2}{J}F\left(\frac{\partial W}{\partial I_1}\frac{\partial I_1}{\partial C}+\frac{\partial W}{\partial I_2}\frac{\partial I_2}{\partial C}+\frac{\partial W}{\partial I_3}\frac{\partial I_3}{\partial C}\right)F^T \tag{2-15}$$

The derivatives of invariants are described in the following equations (2-16) - (2-18).

$$\frac{\partial I_1}{\partial C}=I \tag{2-16}$$

$$\frac{\partial I_2}{\partial C}=I_1 I-C \tag{2-17}$$

$$\frac{\partial I_3}{\partial C}=I_3C^{-1}=I_3F^{-1}F^{-T} \tag{2-18}$$

According to equations (2-15) - (2-18), equation (2-19) is justifiable. By considering $I_3(F) = J$ and $I_3(C) = J^2$ (Bergstroem, 2015), equation (2-20) is achieved.

$$\sigma(I_1, I_2, I_3, T_0) = \frac{2}{J}\left(\frac{\partial W}{\partial I_1} + I_1\frac{\partial W}{\partial I_2}\right)b - \frac{2}{J}\frac{\partial W}{\partial I_2}b^2 + \frac{2}{J}I_3\frac{\partial W}{\partial I_3}I \tag{2-19}$$

$$\sigma(I_1, I_2, J, T_0) = \frac{2}{J}\left(\frac{\partial W}{\partial I_1} + I_1\frac{\partial W}{\partial I_2}\right)b - \frac{2}{J}\frac{\partial W}{\partial I_2}b^2 + \frac{\partial W}{\partial J}I \tag{2-20}$$

Sometimes the deformation gradient of hyperelastic materials is separated into dilatational and distortional parts in finite element analysis. Dilatational part is related to volume change and distortional part is related to volume-conservation. The distortional operator is described in equation (2-21) and the "*" mentions to the distortional parameters. According to this issue, some parameters of equation (2-20) are presented in equivalent distortional parameters in equation (2-22) - (2-25). So, equation (2-26) explains the stress as a function of distortional invariants which can be organized to equation (2-27). Some energy functions are independent to an I_2^* invariant, in this case equation (2-28) clarifies the stress function. The deviatoric operator definition is described in equation (2-29).

$$distortional\left[F\right] = \det\left[F\right]^{-1/3}F \tag{2-21}$$

$$F = J^{1/3}F^* \tag{2-22}$$

$$C = FF^T = J^{2/3}C^* \tag{2-23}$$

$$I_1 = tr\left[C\right] = tr\left[J^{2/3}C^*\right] = J^{2/3}I_1^* \tag{2-24}$$

$$I_2 = J^{4/3}I_2^* \tag{2-25}$$

$$\sigma(I^*_1, I^*_2, J, T_0) = \frac{J}{2}\left(\frac{\partial W}{\partial I^*_1}\frac{\partial I^*_1}{\partial I_1} + J^{2/3}I^*_1\frac{\partial W}{\partial I^*_2}\frac{\partial I^*_2}{\partial I_2}\right)b - \frac{2}{J}\frac{\partial W}{\partial I^*_2}\frac{\partial I^*_2}{\partial I_2}b^2 + \left(\frac{\partial W}{\partial I^*_1}\frac{\partial I^*_1}{\partial J} + \frac{\partial W}{\partial I^*_2}\frac{\partial I^*_2}{\partial J} + \frac{\partial W}{\partial J}\right)I \tag{2-26}$$

$$\sigma = \frac{2}{J}\left(\frac{\partial W}{\partial I^*_1} + \frac{\partial W}{\partial I^*_2}I^*_1\right)b^* - \frac{2}{J}\frac{\partial W}{\partial I^*_2}\left(b^*\right)^2 + \left(\frac{\partial W}{\partial J} - \frac{2I^*_1}{3J}\frac{\partial W}{\partial I^*_1} - \frac{4I^*_2}{3J}\frac{\partial W}{\partial I^*_2}\right)I \tag{2-27}$$

$$\sigma = \frac{2}{J}\frac{\partial W}{\partial I^*_1} dev\left[b^*\right] + \frac{\partial W}{\partial J} I \tag{2-28}$$

$$dev\left[b^*\right] = b^* - \frac{1}{3} tr\left[b^*\right] I \tag{2-29}$$

Silicone rubber is a hyperelastic and incompressible material. So, because of the material incompressibility, equation (2-28) can be written as equation (2-30). In this case, the boundary condition (according to the problem conditions) is performed to calculate the p value as a pressure term of the equation.

$$\sigma = 2\left(\frac{\partial W}{\partial I_1} + \frac{\partial W}{\partial I_2} I_1\right) b - 2\frac{\partial W}{\partial I_2}(b)^2 + pI \tag{2-30}$$

In the following the stress equations of uniaxial, biaxial, and planar loading are calculated. The applied load in the uniaxial and planar tests acts only in one direction while the applied force in the biaxial test acts in two directions. More descriptions about these tests will be given later in 4.1.

In the uniaxial tension, the stretch in the loading direction is λ_1 and the stretch in other non-loaded directions is $\lambda_2 = \lambda_3$. According to equations (2-12) - (2-14) and the condition of $I_3 = 1$ for incompressible materials, the invariants are calculated in equation (2-31). Then, insert the related parameters from equation (2-31) to equation (2-30), to achieve equation (2-32) and (2-33). Afterwards, the stress (applied load) in another direction is zero as the boundary conditions of this problem. The parameter p is calculated, when equation (2-33) equals to zero. Finally, equation (2-34) shows the uniaxial stress equation of the hyperelastic material.

$$\begin{cases} \lambda_2\lambda_3 = \lambda_1^{-1} = \lambda^{-1} \\ \lambda_2 = \lambda_3 = \lambda_1^{-1/2} \end{cases} \Rightarrow \begin{cases} I_1 = \lambda^2 + 2\lambda^{-1} \\ I_2 = 2\lambda + \lambda^{-2} \end{cases} \tag{2-31}$$

$$\sigma_1 = \sigma_{uniaxial} = 2\left(\frac{\partial W}{\partial I_1} + \frac{\partial W}{\partial I_2} I_1\right)\lambda^2 - 2\frac{\partial W}{\partial I_2}\lambda^4 + p \tag{2-32}$$

$$\sigma_2 = \sigma_{transverse} = 2\left(\frac{\partial W}{\partial I_1} + \frac{\partial W}{\partial I_2} I_1\right)\frac{1}{\lambda} - 2\frac{\partial W}{\partial I_2}\frac{1}{\lambda^2} + p \tag{2-33}$$

$$\sigma_{uniaxial} = 2\left(\frac{\partial W}{\partial I_1} + \frac{\partial W}{\partial I_2} I_1\right)\left(\lambda^2 - \frac{1}{\lambda}\right) - 2\frac{\partial W}{\partial I_2}\left(\lambda^4 - \frac{1}{\lambda^2}\right) \tag{2-34}$$

The energy function of some materials is independent to parameter I_2. In this case, the uniaxial stress can be changed from equation (2-34) to equation (2-35).

$$\sigma_{uniaxial} = 2\frac{\partial W}{\partial I_1}\left(\lambda^2 - \frac{1}{\lambda}\right) \tag{2-35}$$

In the biaxial loading, the stretch in two directions of loading is similar and $I_3 = 1$ (incompressible case). So, by considering equation (2-36) and related boundary conditions, the biaxial stress with two invariants is described in equation (2-37) and the I_2 independent biaxial stress is located in equation (2-38).

$$\begin{cases} \lambda_1 = \lambda_2 = \lambda \\ \lambda_3 = \lambda_1^{-2} \end{cases} \Rightarrow \begin{cases} I_1 = 2\lambda^2 + \lambda^{-4} \\ I_2 = \lambda^4 + 2\lambda^{-2} \end{cases} \tag{2-36}$$

$$\sigma_{biaxial} = 2(\lambda^2 - \lambda^{-4})\left(\frac{\partial W}{\partial I_1} + \lambda^2 \frac{\partial W}{\partial I_2}\right) \tag{2-37}$$

$$\sigma_{biaxial} = 2\frac{\partial W}{\partial I_1}\left(\lambda^2 - \frac{1}{\lambda^4}\right) \tag{2-38}$$

$$\sigma_{planar} = 2(\lambda^2 - \lambda^{-2})\left(\frac{\partial W}{\partial I_1} + \frac{\partial W}{\partial I_2}\right) \tag{2-39}$$

$$\sigma_{planar} = 2\frac{\partial W}{\partial I_1}\left(\lambda^2 - \frac{1}{\lambda^2}\right) \tag{2-40}$$

In the same procedure by considering $\lambda_3 = \lambda^{-1}_1$ in the planar (pure shear) deformation, the stress is described in equation (2-39) and if the stress is not related to the second invariant (I2), equation (2-39) will be simplified to equation (2-40) (Beda, 2007; Bergstroem, 2015; SAS, 2013). By use of described equations, the constitutive model of hyperelastic materials can be achieved.

2.3.2 Strain energy

The mechanical concept of the strain energy density is the mechanical energy which leads to material deformation. It can be described mathematically as the load-unload area in strain-stress curve (Loukil et al, 2018).

The strain energy is the function of Cauchy-Green deformation tensor with three invariants of I_1, I_2, and I_3 which is a common isotropic hyperelastic phenomenological model for rubber materials (Wada et al, 2018).

There are different strain energy functions (W) to describe the hyperelastic materials behavior. Because of their extensibility feature, they can be defined in different methods, which are not possible to be described all of them here. So, here some of the important and general functions will be explained, which are supported by the widely used simulation software (FEM software ABAQUS). The most general energy function which leads to most of the other functions is based on a Polynomial model. Equation (2-41) shows a Polynomial energy function. C_{ij}, N, and D_i are material parameters, Polynomial order, and compressibility factor. Different energy functions, such as Mooney Rivlin, reduced Polynomial, Neo Hookean, Yeoh, and so on are defined according to the order values and supported invariants (I). Equation (2-42) shows the Mooney Rivlin energy function which is a Polynomial energy function of first order. In this equation k is the bulk modulus which is related to the compressibility (D). It is considered that $k_0=2/D_1$.

The reduced Polynomial (equation (2-43)) is another subgroup of Polynomial energy functions. In this group of energy functions the I_2 invariant is ignored to reduce the function's complexity. Then, in comparison with the material model parameters (C_{ij}) of Polynomial functions, the material parameter C_{0j} in the reduced Polynomial function is considered to vanish and C_{i0} can get non zero values. Then, the reduced Polynomial function is divided into different functions according to its degree. The Neo Hookean and Yeoh models are more famous in this model group. Equation (2-44) explains the Neo-Hookean energy function order 1. The degree of the Yeoh energy function in equation (2-45) is 3.

$$W = \sum_{i+j=1}^{N} C_{ij}(I_1 - 3)^i (I_2 - 3)^j + \sum_{i=1}^{N} \frac{1}{D_i}(J-1)^{2i} \qquad (2\text{-}41)$$

$$W = C_{10}(I_1 - 3) + C_{01}(I_2 - 3) + \frac{k}{2}(J-1)^2 \tag{2-42}$$

$$W = \sum_{i+j=1}^{N} C_{ij}(I_1 - 3)^i + \sum_{i=1}^{N} \frac{1}{D_i}(J-1)^{2i} \tag{2-43}$$

$$W = C_{10}(I_1 - 3) + \frac{k}{2}(J-1)^2 \tag{2-44}$$

$$W = C_{10}(I_1 - 3) + C_{20}(I_1 - 3)^2 + C_{30}(I_1 - 3)^3 + \frac{k}{2}(J-1)^2 \tag{2-45}$$

The Neo-Hookean is the Hooke's law extension to large deformations (simplest model). The Mooney-Rivlin model is a common and standard model of rubber materials and the analysis of uniaxial tensile and compression and planar tensile test results of hyperelastic materials lead to select the appropriate strain energy function (Steinmann et al, 2012; Wada et al, 2018).

The Ogden energy model (equation (2-46)) is defined in applied principal stretch terms (λ) while the Polynomial and reduced Polynomial models are explained in strain invariants (I) terms. If N and α become equal 1, the Ogden and Neo-Hooke models are equal. Here, α_i and μ_i are the thermal expansion coefficients and shear modulus.

$$W = \sum_{i=1}^{N} \frac{2\mu_i}{\alpha_i^2}(\lambda_1^{\alpha_i} + \lambda_2^{\alpha_i} + \lambda_3^{\alpha_i} - 3) + \sum_{i=1}^{N} \frac{1}{D_i}(J-1)^{2i} \tag{2-46}$$

The J value of the hyperelastic materials is usually equal 1. So, in the above equations, the part which is related to J and bulk modulus can be ignored.

The maximum degree of Polynomial, reduced Polynomial and Ogden which FEM software ABAQUS supports, normally are 2, 6, and 6, respectively.

There are other models which will not be discussed here, because they would lead too far to this subject. For example, the Arruda-Boyce model was achieved according to microstructure and molecular model of hyperelastic theories which is a statistical model and it is not in the working area of this dissertation. There is another model to get the material energy function directly from the real uniaxial test results. This model in some cases is named Marlow model. The energy function in the Marlow model is determined

only with first strain invariant. This model is a high accurate method for uniaxial tension data but it is not accurate for biaxial test data (Bergstroem, 2015).

To find a material energy function and a material model, material tests should be performed and according to experimental test data, model and material parameters should be selected.

The Mullins effect is the most well-known damaging effect on the rubber materials. If the rubber's mechanical behavior shows the damage from the previous loading history the continuum damage mechanics (CDM) theory should be considered as a function of the load cycles or time (Wada et al, 2018).

A development in the automation level of an indirect gravure printing machine will be described in the next chapter. Therefore, the printing machine structure will be presented. Then, a process of machine development to improve the automation level will get explained.

3 Development of the indirect gravure printing machine

The first indirect gravure printing machine was created nearly 200 years ago. Afterwards, its automation level has been developed over time to level 0 and level 1 (Micro Print, 2014; Morlock, 2012; Tampoprint, 2014). The concept of automation level was described in chapter 2.1.3. Nowadays, some developed indirect gravure printing machines with the highest automation level (level 1) can control the printing speed in vertical direction (Kuscharski, 2017).

This work concentrates on automation level developments of indirect gravure printing machines with the porpuse of its use in scientific fields.

Part of the work described in this chapter was published in (Hakimi Tehrani et al, 2016).

3.1 Indirect gravure printing process

The general structure of indirect gravure printing is described in the following. First, the elements of the printing unit get introduced. After an acquaintance with the printing unit elements, role of pad, printing form table and printing object in printing steps will be clarified.

Printing unit elements

Figure 3-1 shows the printing units of an indirect gravure printing machine. It consists of impression (pad) unit, inking unit and object-holding unit. The pad is an element of the pad unit. The pad transfers ink to the substrate. The pad linear guide (cylinder) has the role of pad movement. The pad linear guide is coupled with the pad by the pad coupling element. The object-holding unit's function is to hold and fix the substrate in the correct position. The vacuum table has a flat and rigid surface and is usually used to hold flat substrates. The substrate table holds the substrate and all the objects that are

related to the substrate. The substrate is the object that the pad transfers the ink layer to it. The inking unit elements are the ink cup, the printing form and the printing form table. The ink cup (in closed systems) consists of a sealed ink container and a round shaped doctor blade. The doctor blade removes the extra ink over the printing plate in the backward movement while the ink remains in the engraved cells. This happens after the ink feeding in the printing form with forward movement of printing form table. The printing form consists of an engraved motif which is filled with ink. The pad picks up the ink from the printing form. The printing form table is the printing form carrier which moves the printing form forwards and backwards in various steps of the printing process.

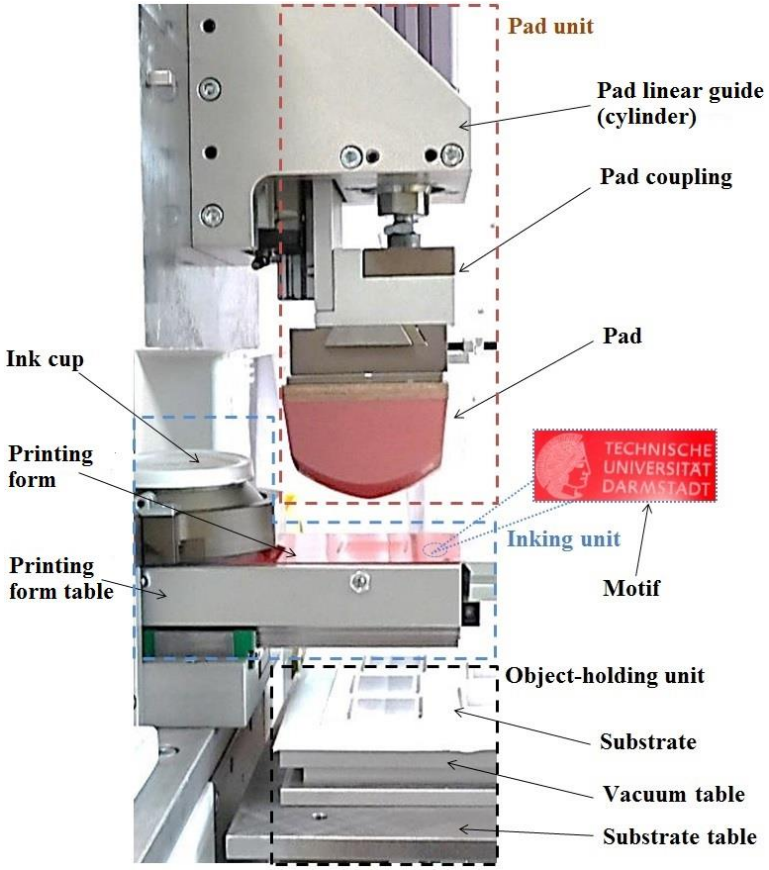

Figure 3-1: The indirect gravure printing process units. The impression (pad), inking and object-holding units consist of different elements which are shown here.

Description of indirect gravure printing process

Figure 3-2 shows the indirect gravure printing steps. Generally, the moveable elements are the pad and printing form table. At the beginning of the process, the printing form and pad are in their reference position, where ink can flow into the engraved cells of the printing form.

A reference position is an initial position for pad and printing form table with the following conditions. The ink cup should completely cover the motif area of the printing form when the printing form table is located at the reference position. The printing form table should not be located along a pad motion path while the printing form table is located in its reference position. There is no interaction between the pad surface area and the motion path of the printing form table when the pad is located at its reference position. Here, the ink cup is positioned in a fixed place in different steps of the printing process.

In step 1, the printing form table moves in the forward direction. Here the doctor blade wipes excessive fluid off. The pad moves in the downward direction to take up the ink (step 2). In step 3, the pad with a layer of ink elevates from the printing form. Then, the printing form table reverts to the original position (step 4). The pad comes down to print the ink layer on the substrate in step 5. Finally, in step 6 the pad revert to the reference position (DECO, 2018; Hahne, 2001; Hakimi Tehrani et al, 2016).

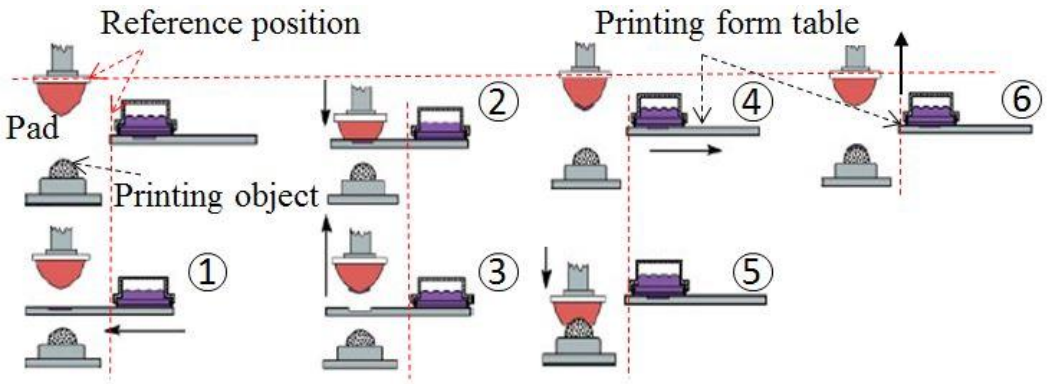

Figure 3-2: The steps of printing in an indirect gravure printing process. The dashed lines in red color clarifies the reference positions which are the start position of the pad and the printing form table. The numbers describe the print steps. The steps should be performed respectively to complete the printing process and get the printed objects.

The operator usually has to push a button for execution of each printing step in the conventional indirect gravure printing machines.

3.2 Requirements concerning an automated indirect gravure printing machine

The automation level of conventional indirect gravure printing machine is developed to fulfill the following requirements.

Pressing less push buttons to execute each printing iteration: It will lead to more similar printing conditions in different printing iterations. In this case, the operating time in the printing process is independent of the delay time of users of the machine.

Control of the speed and time for each printing step: The operating time in different steps of the printing process will be controllable.

New control unit: A real-time, embedded industrial machine controller with monitoring capabilities will be added to the system.

Exchange the drives of motion system: They will be exchanged from a pneumatic system to an electrical system.

Force measuring system: The force measurement system will be added to the machine for more accurate monitoring of the printing process.

Online and offline monitoring: The monitoring of printing parameters will be possible during and after the printing process.

Save and reuse of set points: The set points of printing parameters will be saved and reused for next printing iterations.

3.3 Indirect gravure printing machine consideration as a mechatronic system

A mechatronic system is an integration of different fields such as mechanics, electronics and control which are used to improve or optimize the system's functionality. These fields are shown in Figure 3-3 and in each field the related subjects are listed. The subjects that this research will focus on were marked by brown color. Figure 3-4 shows the mechatronic system structure. This structure includes a control unit, sensors, actuators and mechanics. The arrow directions in Figure 3-4 present the data transferring direction between different parts of mechatronic system (Casner et al, 2017; Hakimi Tehrani et al, 2016; Isermann, 2008). For example the control unit sends the

commands to actuators. Then, they execute the commands by use of the mechanics parts. The sensors measure some parameters and send them to the control unit.

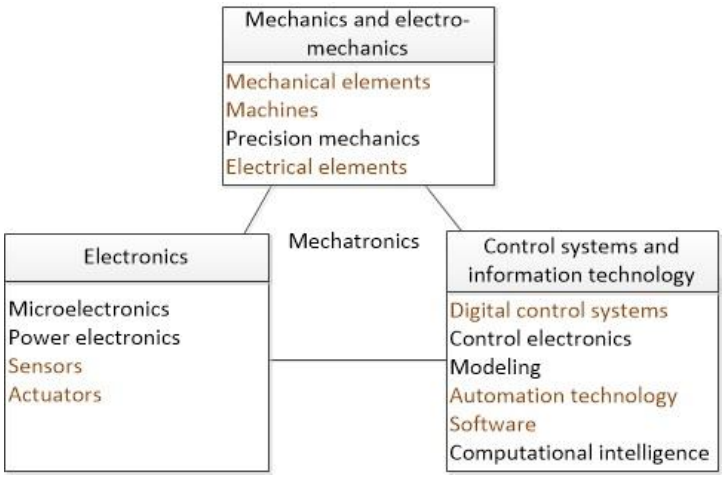

Figure 3-3: The mechatronic system related fields. This dissertation concentrates on the marked subjects. This figure is based on (Casner et al, 2017; Hakimi Tehrani et al, 2016; Isermann, 2008).

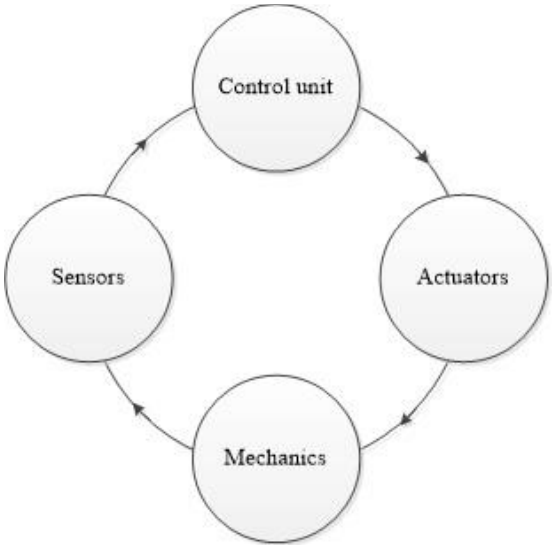

Figure 3-4: The mechatronic system structure. It shows different parts of a mechatronic system. The arrow directions show the sending and receiving directions of data. This figure is based on (Casner et al, 2017; Hakimi Tehrani et al, 2016; Isermann, 2008).

The indirect gravure printing machine structure consists of three main fields, which are electronics, control systems and mechanics. To organize the elements and improve the automation level of the indirect gravure printing machine as a system, it is considered as a mechatronic system (Hakimi Tehrani et al, 2016). The indirect gravure printing machine units are organized according to mechatronic system structure in Figure 3-5. It

shows the elements of each unit and the data transferring direction between different units of indirect gravure printing machine with arrow directions. The units and their elements are described in the following.

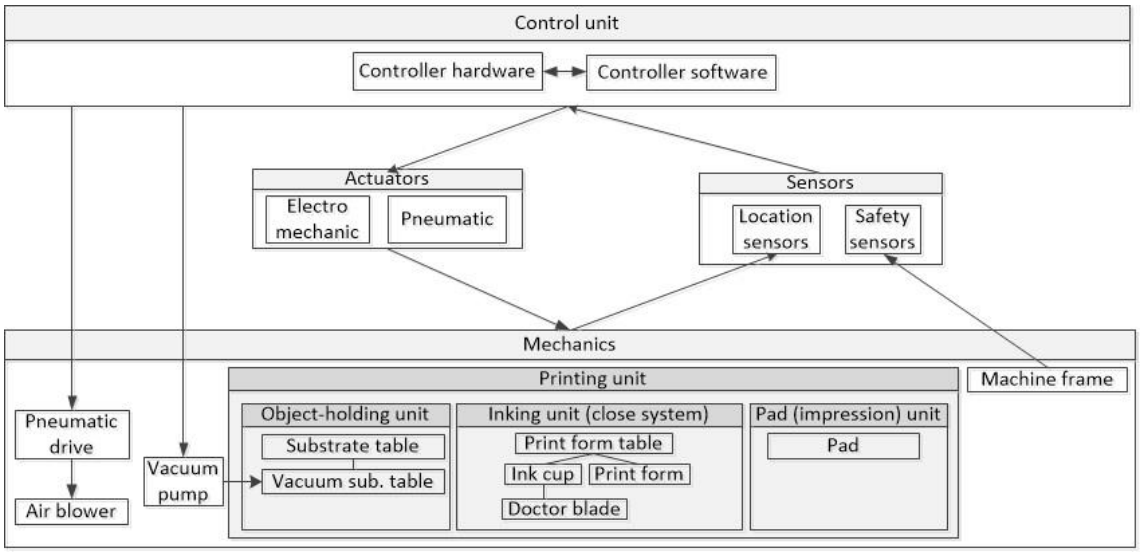

Figure 3-5: The indirect gravure printing machine units were organized according to mechatronic system structure. The printing unit is located in the mechanics. It consists the object holding, inking and pad units. The arrow direction describes the data flow direction.

Control, actuators, mechanics, sensors units

The control unit is the center of processing and logical calculations. The controller hardware is the control unit's main element with the main goal of system control (Kiel, 2008). In addition to other units, it sends and receives the control data of the elements in its unit (internally) such as controller hardware and controller software which communicate with each other.

The actuators are "the muscles of the automation system" (Kiel, 2008). The control unit sends the commands to actuators and they execute the commands on elements of mechanics unit.

The mechanics unit is the executive part of the system which shows the mechanical responses of user demands. The printing unit is one part of the mechanics unit which is divided into impression (pad), inking and object-holding units in the indirect gravure printing system (Hakimi Tehrani et al, 2016).

The sensors unit measures the mechanics unit parameters and transfers them to the control unit for further analysis. The sensors of an indirect gravure printing machine are divided into safety, controlling and measurement (location) sensors. The safety sensors are used to increase the machine safety with more focus on human safety. For example, micro switches are located on the machine surroundings to protect the user and print object during the printing process. These sensors send the signal to the controller and the controller stops the printing process immediately as soon as they get activated. The controlling sensors control the position of some elements of mechanics unit such as vertical and horizontal axes. For example, when the horizontal axis is located in the reference position, the controlling sensor sends the related signal to the control unit.

The Morlock GFG100 (Morlock, 2012) is the type of indirect gravure printing machine which is developed and discussed in this dissertation. The machine schema with location of the axes are shown in Figure 3-6. The related coordinate system and printing direction are presented in this figure.

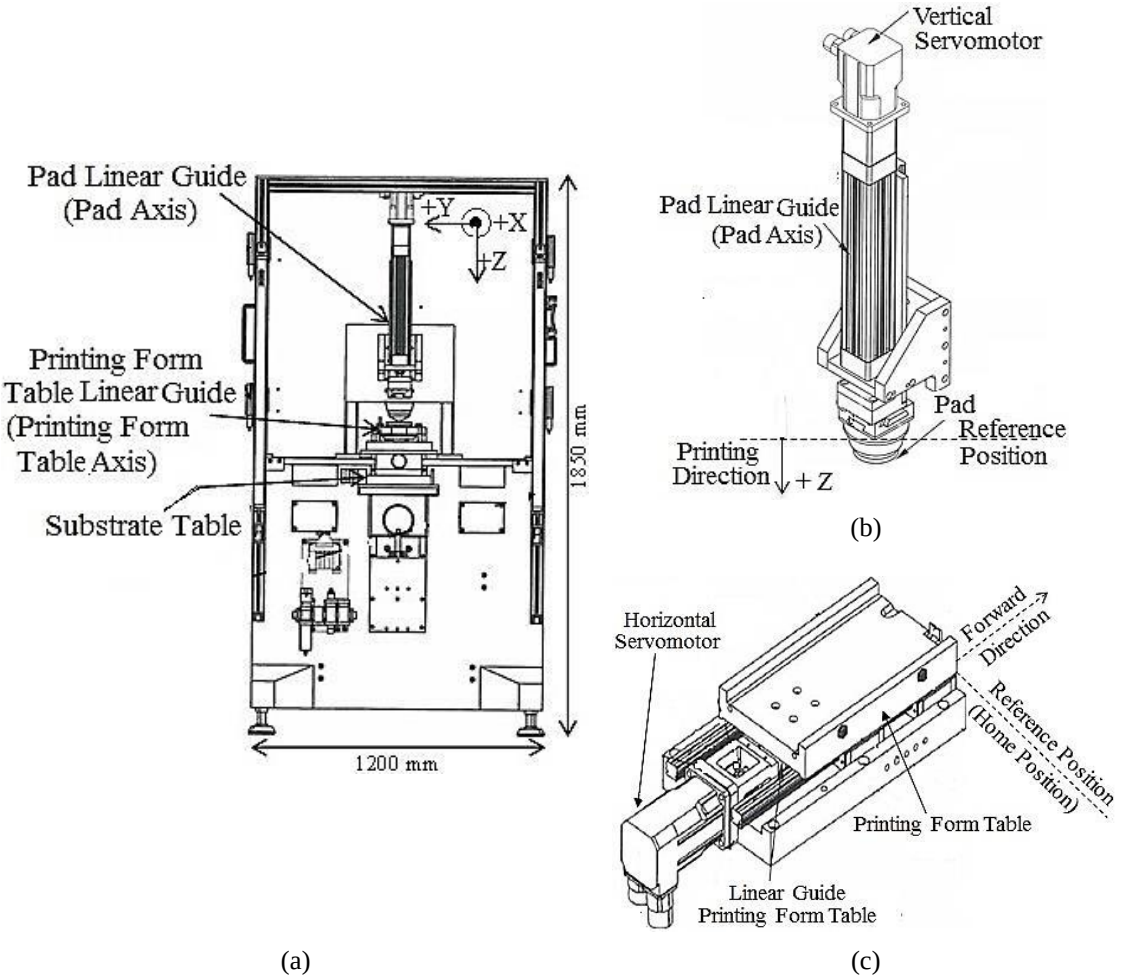

Figure 3-6: The indirect gravure printing machine layout. (a) Location of machine parts and the related coordinate system is presented here. (b) Related elements to pad axis. (c) Related elements to the printing form table axis. They present the position of elements on Morlock GFG100 indirect gravure printing machine in more details to make clear the described elements in the text. This figure is based on (Morlock, 2012).

An indirect gravure printing machine has the maximum two degrees of freedom (DOF) during printing. As it was shown in printing steps (Figure 3-2), a pad axis moves in Z-direction and a printing form axis moves in X-direction. In this case, Z and X directions can be considered as vertical and horizontal directions. So, there are two main servo drives in control unit to control vertical and horizontal servo motors as system actuators. After receiving the commands, the servo motors execute it and effect on mechanical elements such as linear guides (cylinders).

3.4 Process of the machine development

The use of indirect gravure printing in scientific fields is increasing day by day. It can be applied to print sensors, electroluminescent panels and so on. For example, the developed indirect gravure printing machine described here, is a distinguished method to study the printing process of electroluminescence on curved surfaces (Hirmer et al, 2016). So, the development process is performed with a focus on print parameters controllability and data tracing during and after a printing process. The ability of online and offline data monitoring leads to a performance of more accurate and controllable scientific researches. So, according to these goals and the structure of the indirect gravure printing machine in Figure 3-5, highlighted blocks in Figure 3-7 display segments of the machine that are developed here.

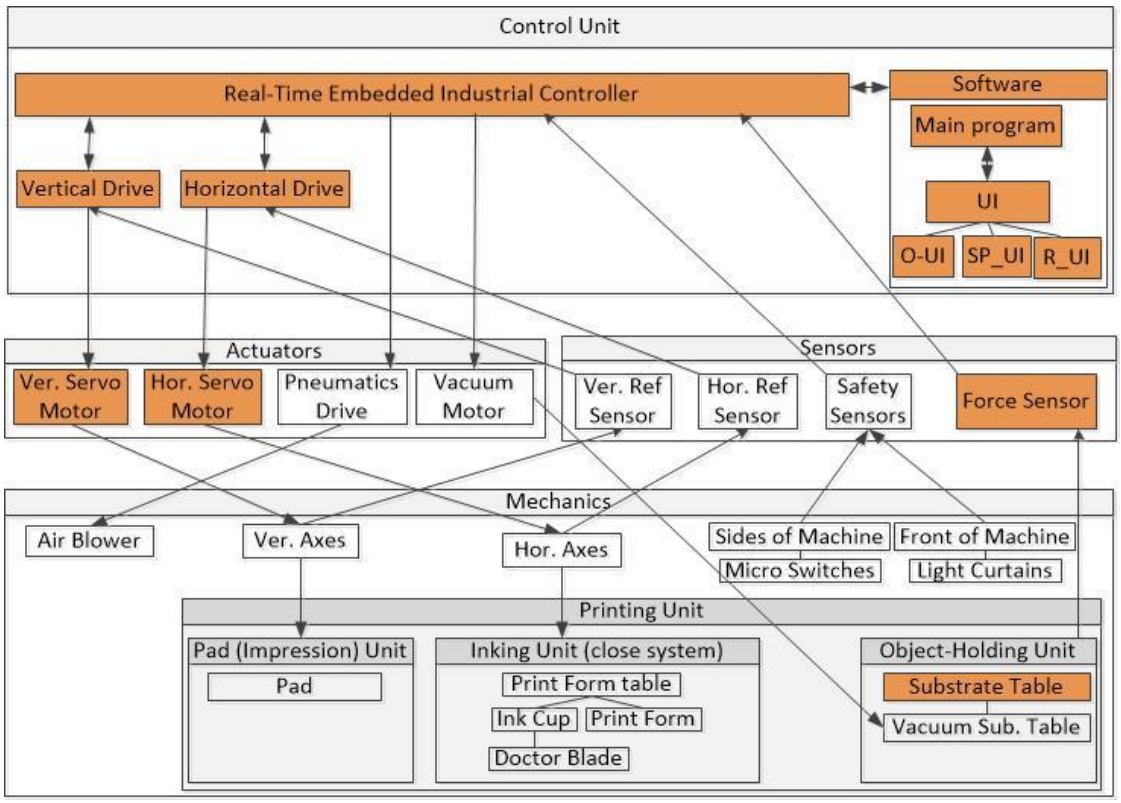

Figure 3-7: The indirect gravure printing machine units (Hakimi Tehrani et al, 2016). The highlighted blocks show the units and sub-units of the machine developed by the author. The blocks are described in detail in the following chapters.

3.4.1 Development in software

Software is a sub-unit of a control unit in the indirect gravure printing machine. Further than process control, main roles of the control unit are the signal processing and logical calculations before, during and after the printing process.

The software as part of a control unit in Figure 3-7, is divided into two segments: Main program and UI. UI is an abbreviation for the user interface.

Figure 3-8 shows schematically a communication between different parts of the software. According to this figure, UI receives user demands through SP_UI and O_UI which are user interfaces for set points of printing parameters and operating buttons, respectively. Then, UI sends them to the main program for execution. The main program executes the commands and performs the signal processing and logical calculations. Afterwards, the main program sends the executive commands to the actuators unit through the real-time embedded industrial (RTEI) controller part. Further, the main program sends calculation results and system reports to R-UI through UI. R-UI is a user interface which reports important printing parameters such as position, velocity and force in different steps of the printing process.

The controller is connected to actuators and sensors. It receives signals from sensors and commands from the main program and executes them with actuators. The sensor signals are related to the measured values and detected positions by sensors.

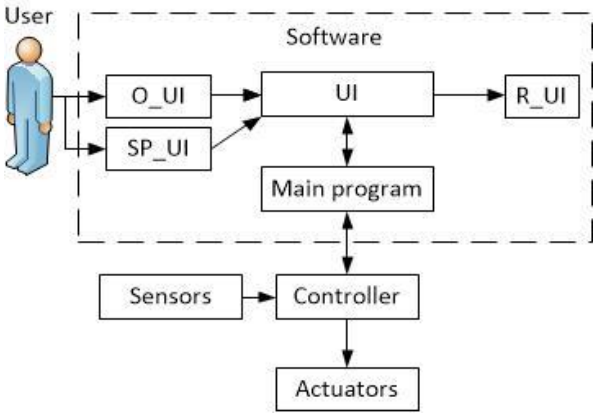

Figure 3-8: The software sub-units communication. The communications between O_UI, SP_UI, UI, R_UI and Main program as sub-units of the software with other units are shown here. The arrow direction describes the data flow direction.

O_UI is displayed in Figure 3-9. The operating buttons are located on O_UI. Start and Stop buttons can start and stop the printing process. “Find Home” button is used for

sending the horizontal and vertical axes to their reference position. “HLE” button would activate the program if a high level error occurred. The high level error is described in the description of Figure 3-13. “Vacuum” and “Air Blower” buttons will turn on their pumps. The vacuum option is used to fix the substrate on the table and the air blower option leads to blowing air on the pad surface, for increasing the speed of solvent evaporation in some special cases. “Vertical_Movement” button is pushed when only a pad movement in the vertical direction is desired. In this case, the printing form table is fixed. “Printing Form Service” button is pressed when the printing form needs maintenance services such as cleaning. In this case only the printing form table is moved. On the left side of the figure, a printing process is shown on-line. “Printing No.” shows the number of printed specimens. The same number is used to save printing parameters in R_UI. So, it can be used to trace the printing parameters of each printed specimen after printing (offline).

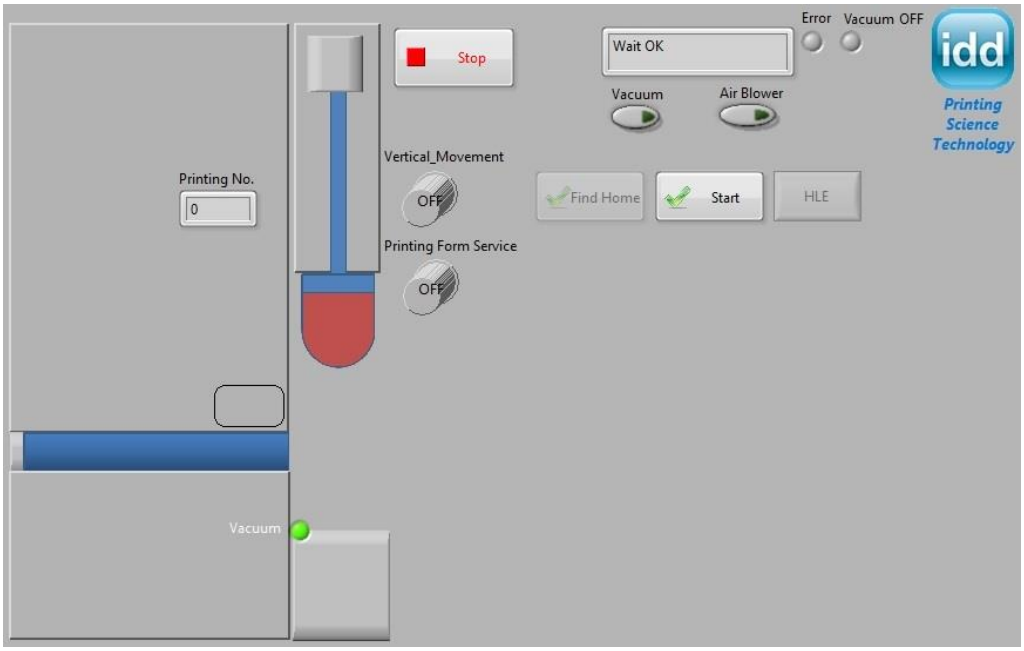

Figure 3-9: The operational user interface. It is abbreviated with O_UI. The operating buttons are located on this UI and the current step of the printing process is shown online in the left side, graphically.

Figure 3-10 shows the machine set point user interface. SP_UI contains input variables for the main program. The input variables are parameters for the printing process.

In SP_UI, the input variables are organized in six different groups according to the six different steps of the indirect gravure printing process in Figure 3-2. In all steps, the

velocity can be changed. Further, the position values in different steps, except of step 4 and 6, can be defined. The velocity and position in vertical and horizontal directions are explained as velocity and position of the pad and the printing form table, respectively. In step 4 and 6, the printing form table or pad should come back to their reference positions, so the position value is fixed to be zero. In step 2 and 5, a contact time of the pad with printing form and substrate can be defined. In step 2 and 5 by pushing "Force_cont" button, the printing process can be performed according to an acting force of the pad on the printing form or substrate. In this case, some extra variables should be set such as desired force. After step 6, there are two variables to set the printing form table position and its velocity. In this step, the printing form table moves forward to perform maintenance services on a printing form. These services are related to extra operations on the surface of a printing form such as cleaning, position adjustment, ink density observation and so on. There are two options on the above part of SP_UI. They are used to save and load the input (printing) parameters of SP_UI. This ability makes it easy to use the print parameters at different times.

Figure 3-10: The set point user interface which is called SP_UI. The printing parameters are adjusted here. The interface structure is organized according to the printing process steps from number 1 till 6 on the left side. In front of each number there is a short description about related steps.

Figure 3-11 shows the important printing parameters which are monitored online in graphs of R_UI. The X, V_X, Z and V_Z are printing form table position, printing form table velocity, pad position and pad velocity, respectively. The position and velocity units are mm and mm/s. The pad force on the substrate and the printing form are related to "F_sub" and "F_printing form" with unit of N. Further than online monitoring of these printing parameters, they are saved in each printing iteration. They can be used offline to analyze the printing parameters in comparison with printing results. The field at bottom of R_UI is related to the file path where the printing parameters are saved.

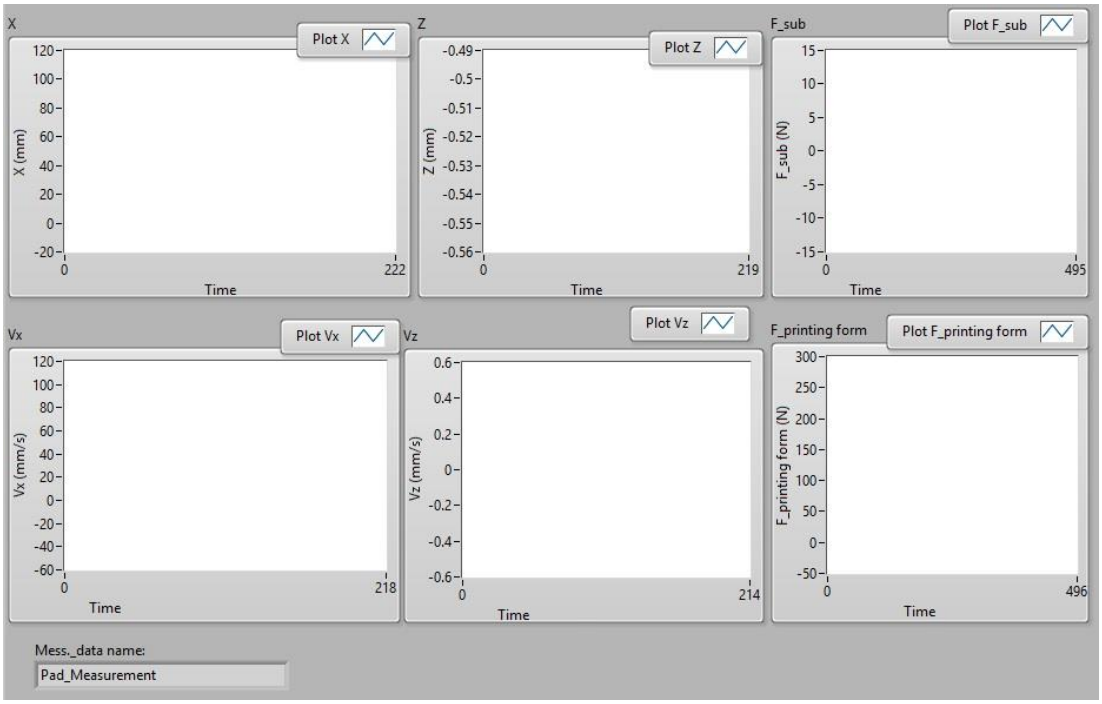

Figure 3-11: The measured printing parameters are displayed online on R_UI. Further, it shows the file path where printing parameters are saved for offline use. It supports the printing parameters such as position, velocity and force during the printing process.

Figure 3-12 is a flowchart of the indirect gravure printing working process. It describes the working process systematically. The used flowchart symbols clarify the nature of each part. The pad, ink, printing form and substrate are the process inputs and the printed substrate is the process output. Getting the printed substrate as an output from the inputs is the goal of this process which can be achieved in each iteration of this process. The flowchart steps are matched with the indirect gravure printing steps which were described in Figure 3-2.

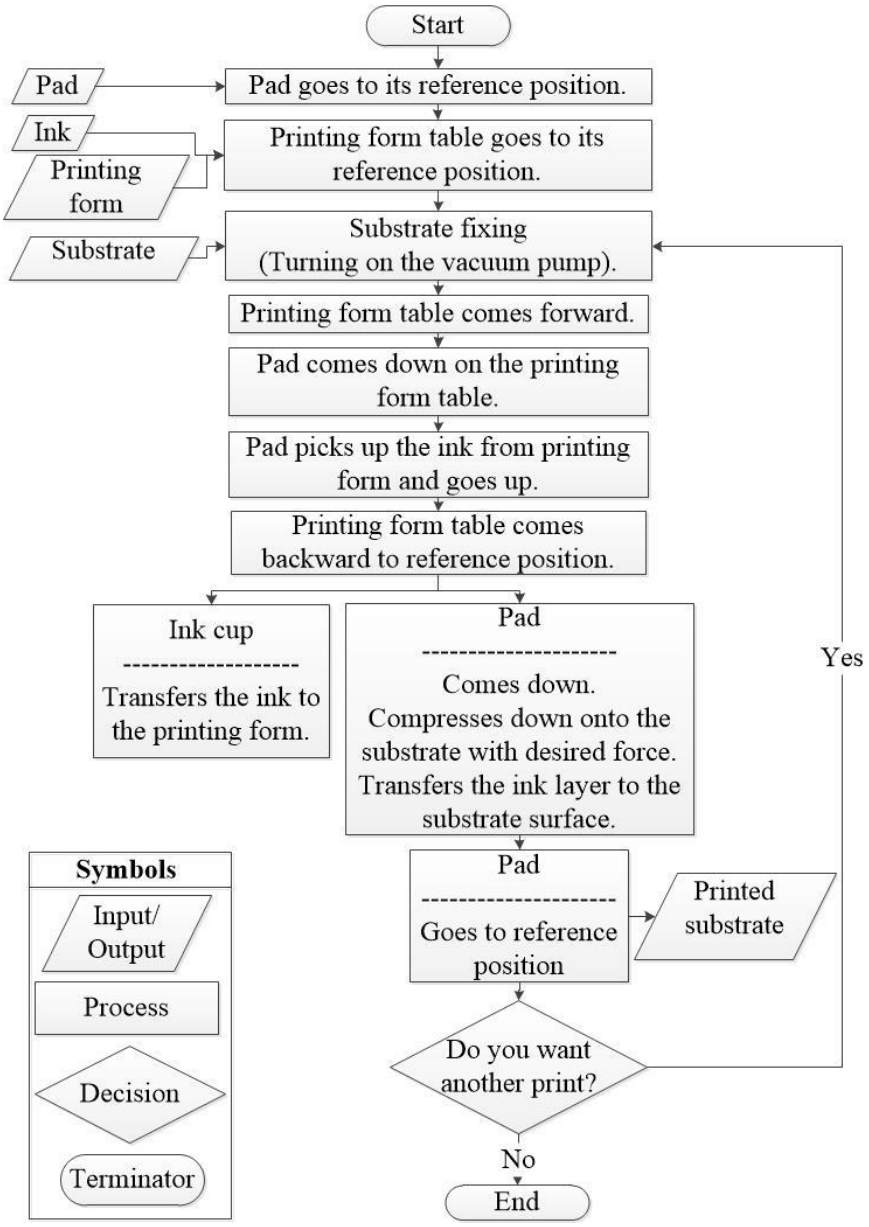

Figure 3-12: The indirect gravure printing process steps. The flowchart shows different steps to get print results. The concept of different symbols which were used in this flowchart are mentioned at the end of this figure. Figure is based on (Hakimi Tehrani et al, 2016).

Figure 3-13 is the state diagram of the indirect gravure printing machine process which is programmed in the main program segment of the software. It is achieved according to the flowchart steps in Figure 3-12. Each circle is a state in the program structure. After starting the program, in the first state, it is waiting to get a start command from the user.

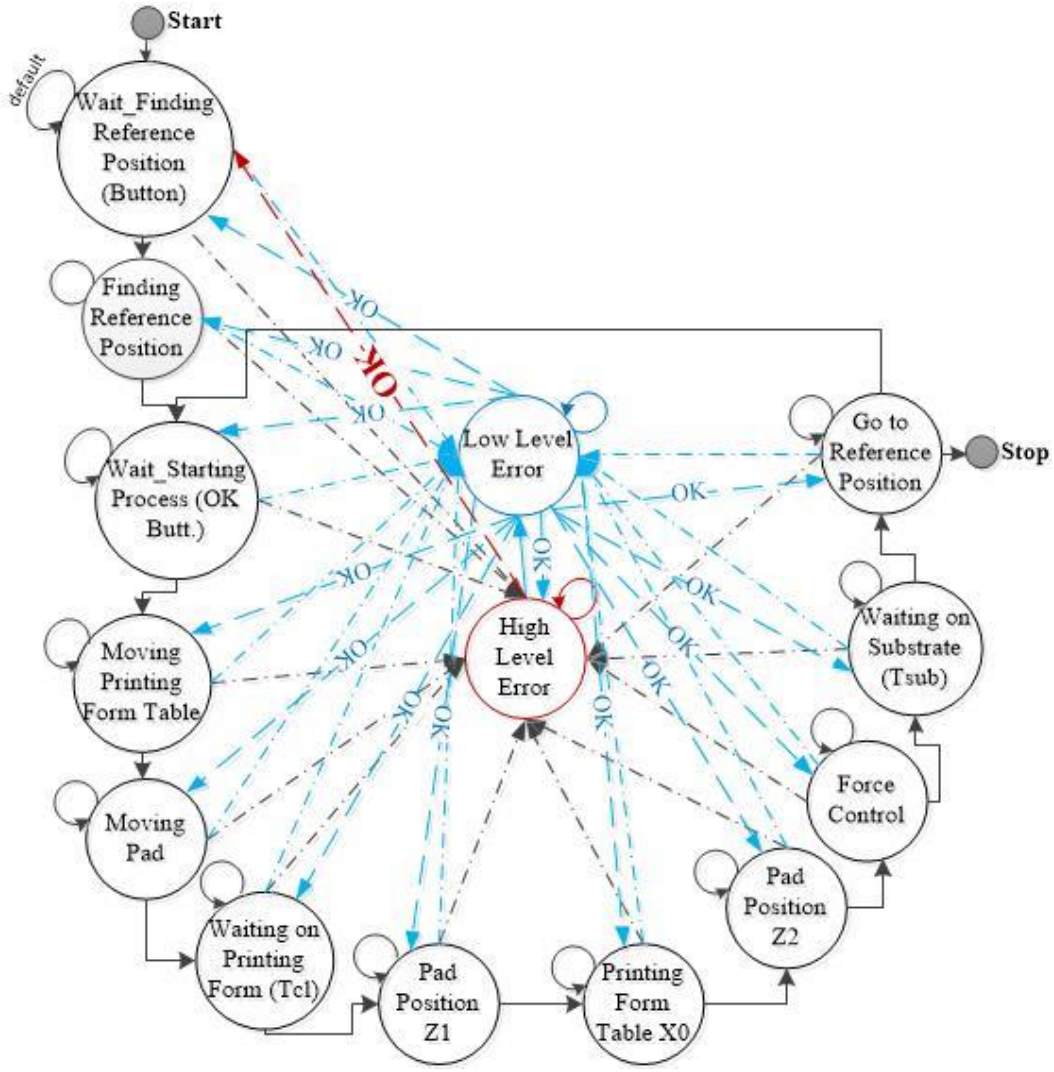

Figure 3-13: The state diagram of the indirect gravure printing machine program. It shows different states of the program. The performance of these states leads to control and monitor of the indirect gravure printing process.

After the start of the program, the pad and printing form table axis move to their reference position. Next, the program is waiting for the starting process button in the software user interface (UI) getting pressed. Then, the printing form table comes forward. In the next state, the pad comes down on the printing form table. It can wait on the printing form to pick up the ink for the waiting time which is set in SP_UI. In the next state, the pad goes up, and the printing form table comes back to the reference position. Then, the pad comes down to transfer ink onto the substrate and in next state, the printing force on the substrate can be controlled. Further, a contacting time between the pad and substrate can be set in SP_UI. Finally, the pad goes to reference position

and waits for the next print command or a stop command. Always, safety and location sensors check the environment and after detecting an undesirable event in their environment, immediately the system state changes into Low Level Error (LLE) or High Level Error (HLE) state. In LLE and HLE states, the current printing process gets stopped when an undesirable event appears. After the disappearance of the undesirable event, the printing process state will change from LLE state into the last state before happening the undesirable event. In the case of HLE state, the printing process state will be changed to the first state in the beginning of the program when the undesirable event is disappeared. For example, when the emergency push button of the machine is pressed by the user, the machine will be stopped as a reaction of HLE state. In this case, the system state will be immediately changed to HLE state. It will be remained in this state until releasing the push button. After releasing the push button, the system state will be changed to the first state of the program.

3.4.2 Development of controller, actuators, sensors and mechanics

The controller type and software programing method are affected by the purpose of the indirect gravure printing machine's application. So, the machine should fulfill new demands which are created in the market for the indirect gravure printing machine to use in scientific fields and researches such as printed electronic devices and biomedical applications. Because of that, it is developed for scientific applications.

In this case, control, actuators, sensors and mechanics units should be highly accurate in controlling, operation, measurement and monitoring. As control unit hardware, CompactRio (cRIO) 9074 from National Instruments was used. cRIO is a real-time, embedded industrial machine controller with additional monitoring capabilities. Its specifications have been described in (National Instruments, 2014). It contains a real-time processor chip with speed of 400 MHz and input/output (I/O) modules to connect measurement devices, actuators and sensors to it. Further, external devices through networking can be expanded to this controller. The printing machine's horizontal and vertical drives are Kollmorgen AKD servo drives as part of controlling unit. They can be programmed to measure and control the speed, acceleration, position, torque and current of servomotors. In this case, the real-time embedded industrial controller and drives support EtherCAT protocol to transfer data and this ability was used here (Kollmorgen, 2010; National Instruments, 2012a; b). The synchronization time between

master and slave parts is less than 1 µsec which it causes a high speed performance with EtherCAT protocol. So, it is useful for coordinating motion between motion axes and it is suitable for projects which motion control and measurement equipments are used in it (ETG, 2014; National Instruments, 2012b). So, EtherCAT protocol was used in the developed indirect gravure printing machine to get an accurate and precise control in addition to a fast and synchronized data transferring between the drives and controller.

A single point load cell with a maximum capacity of 100 kg was added to the machine to measure force changes in the printing process. Its safe load limit is 150 kg at a maximum eccentricity of 150 mm and accuracy class C3. By the use of the force sensor, force values during the printing process with a high accuracy level (Mininum verification interval of 0.1961 N for maximum capacity of 980.665 N) are monitored.

The substrate table was developed to perform scientific researches on curved surfaces. In this case, different cylindrical metal parts with different diameters can be assembled on the table and flat substrates can be wrapped around the cylinders. In this case, results of printing on different parts of curved substrates are transferred to flat surfaces and their analysis (e.g. image processing to evaluate print quality) becomes easier. The results and methods of regarding the use of flat substrates wrapped around cylinders were described in (Ücüncü, 2015).

3.5 Improvement of automation level with machine development

The automation level explanation and the automation level of conventional indirect gravure printing machines were described in chapter 2.1.3. Therefore, the automation level of the conventional indirect gravure printing machines with control system, actuators and sensors are located at level 0 or 1. The improved indirect gravure printing machine which was described in this chapter is able to monitor online the printing process and printing parameters. It displays the printing results online during the printing process on the user interface of the machine. So, the automation level 2 is reached. Further, saving and reuse of printing parameters for next times according to feedbacks of the monitored data, are possible. Also, the user is able to store, handle and trace data (online and offline) with use of DIAdem (Version 15, National Instruments). These important improvements can establish an information management system for the indirect gravure printing. So, these developments lead to improve the automation level of indirect gravure printing to level 3.

Further development in the automation level of indirect gravure printing process will be achieved by simulation of the printing process. The results of the next chapter are used to perform the simulation of the printing process. So, the silicone rubber characteristics as the pad material are described in the next chapter.

4 Silicone rubber characteristics

The characteristics of silicone rubber as pad material will be described in this chapter. First, the mechanical testing methods for silicone rubber are introduced. Second, the measurement setups are implemented. Third, the test results of different test methods are achieved to characterize the pad material with different hardnesses. Finally, the hyperelastic material models for different hardnesses are calculated. Then, a model which is more fitted to the experiments will be selected between the various models. Further, the fitting situation of calculation results and experiments shows the validation status of selected models.

4.1 Mechanical testing methods for silicone rubber

To evaluate the material behavior, the number and complexity of test specimens should be decreased as much as possible because they consume time and cost (Steinmann et al, 2012). So, the optimum test models are selected with the highest usability and with respect to the highest recommendation.

4.1.1 General concepts

Generally, an ideal material model has the following specifications which usually is not possible to gain all of them. First, use the minimum number of material parameters which are possible (e. g. the minimum number of invariants or degree of Polynomial functions). Second, the capability to get the material behavior results in complex deformations for different structures. Third, the ability of material parameter specification with few simple tests (Steinmann et al, 2012). Shortly, in an ideal model with a minimum number of simple tests, the minimum useful material parameters should be selected to achieve the material behavior in complex deformations.

So, here the useful test methods to investigate the material model are described. They are clarified in Figure 4-1. The uniaxial tensile test and equibiaxial compression test, the

uniaxial compression test and the equibiaxial tensile tests, the planar tension and planar compression can be considered instead of each other (Simulia, 2013b). The reason comes from the loading effect of hydrostatic stresses on incompressible materials. It is schematically presented in Figure 4-2. For example, in the second row, the vector adding of uniaxial compression and hydrostatic tension in Cartesian coordinates equals to biaxial tension. The hydrostatic pressure (compression) will not deform the incompressible materials (Berselli et al, 2011). Then, the uniaxial tension and biaxial compression are considered equal.

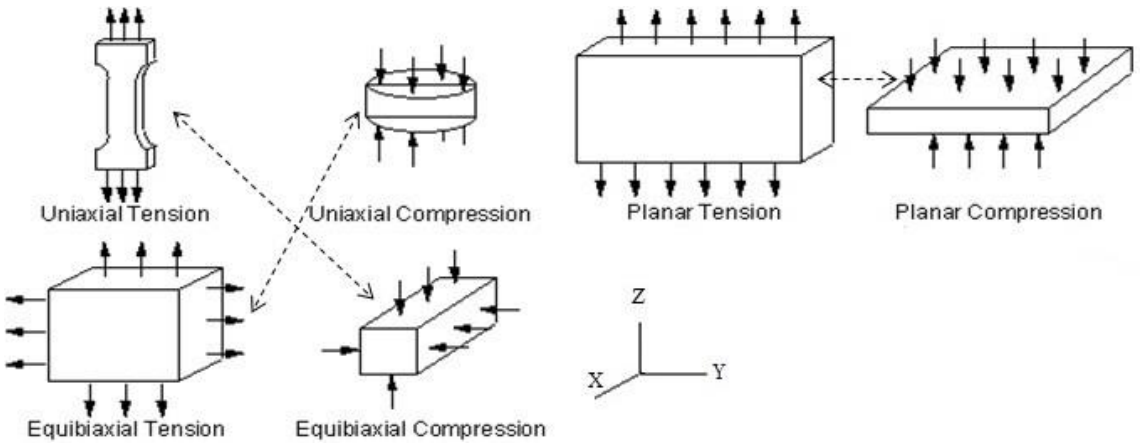

Figure 4-1: The relationship between different hyperelastic material test methods, namely uniaxial, equibiaxial and planar tension and compression test methods. The dashed lines show the similar test methods. The test results of similar test methods are nearly equal to each other in incompressible materials. Figure is based on (Simulia, 2013b).

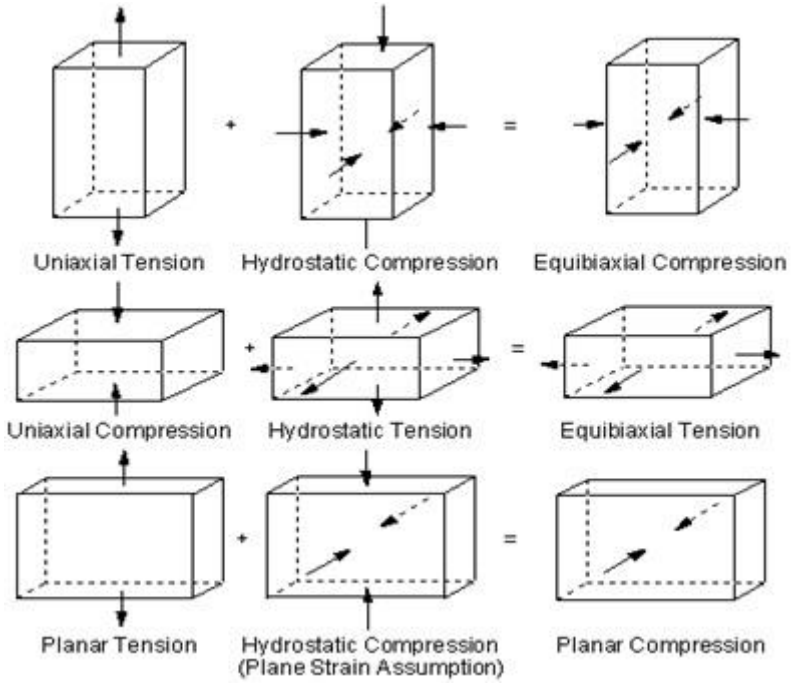

Figure 4-2: The proof of similarity between some test methods by showing the effects of loaded hydrostatic stresses on incompressible materials. The hydrostatic pressure does not deform the incompressible materials (Berselli et al, 2011). So, the described equality between the test methods in both sides of equation can be proven. Figure is based on (Simulia, 2013b).

The suitable test methods are chosen by considering the described situation for a suitable and efficient material model (a minimum number of simple tests and the minimum useful material parameters), focus on cost efficiency issues (decrease time and costs), the available material test instruments and the FEM software ABAQUS needs for hyperelastic material behavior simulation.

In the following, the related test methods are described and further in chapter 4.3, the test results will be discussed.

4.1.2 Uniaxial tensile test

In a uniaxial tensile test, a silicone rubber test specimen stress-strain behavior during a loading and/or unloading extension in one direction such as Z-direction is measured. In this case, to test the specimen, different parameters should be set according to the standard method. The test specimen shape is one of the important parameters and usually has a shape of dumb-bell or dog-bone in different sizes.

The ASTM 412 and ISO 37 (ASTM D412, 2016; ISO 37, 2012) are standard methods to execute silicone rubber uniaxial tensile tests. The test parameters such as test specimen geometries, test speed, test environment and so on are described there.

The test specimen's shape, the related dimensions and test types are clarified in Table 4-1 according to the standards. The test speed is 500 mm/min for test type 1, 1A, 2 and 200 mm/min for type 3 and 4. The thickness of the specimens for test types 1, 2, 3 and 1A is 2 ± 0.2 mm and for type 4 is 1 ± 0.1 mm. The stretch of a special area in the middle of test specimen should be measured and is called test length (TL). The test length for different types of test specimens is not equal. A normal extensometer measures the test machine grapes distances which is not useful for rubber materials, because the test length is not equal to the grape distances. To fulfill this situation, a non-contact extensometers can be used. One type of non contact extensmeters is the video extensometer system. In the video extensometer system, the test length of the specimen is marked and the video extensometer measures its extension during the test (ASTM D412, 2016; ISO 37, 2012; Raupach, 2016). So, for this case, a video extensometer system was designed by the author. The designing process and its optimization were described in (Benedikt et al, 2017). The video extensometer system was used to measure the extension and retraction of rubber test specimen.

In uniaxial tensile tests, the test specimens should be selected as large as possible to decrease the measurement errors, but the test machine and test specimen preparation are determinative elements to select the largest one.

Table 4-1: The test specimen's dimensions in different test types. TL, A, L, TW and W are test length, length of narrow part, total length, test width and total width of test specimens, respectively. They are the important parameters of dumb-bell shaped test specimens.

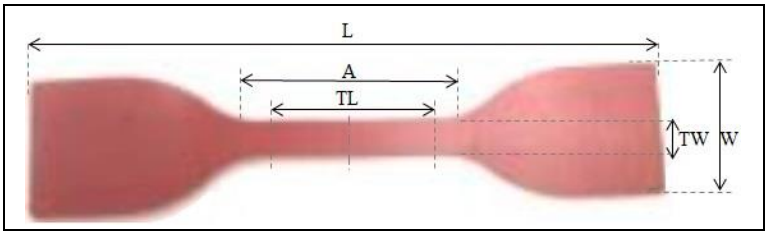

Test type ⇨ / Dimensions ⇩	Type 1 (Type C)	Type 1A	Type 2	Type 3	Type 4
L (mm)	115	100	75	50	35
A (mm)	33±2	21±1	25±1	16±1	12±0.5
TL (mm)	25±0.5	20±0.5	20±0.5	10±0.5	10±0.5
TW (mm)	6.2±0.2	5±0.1	4±0.1	4±0.1	2±0.1
W (mm)	25±1	25±1	12.5±1	8.5±0.5	6±0.5

The uniaxial tensile test can be executed in loading or cyclic (loading-unloading) deformations according to the aim of the work (Bergstroem, 2015). The loading is summarized only to get the test data during the tension of material (one time) till a maximum amount of strain or stress is achieved at the end point of the test. In one cycle (loading-unloading) test method, after getting the maximum strain or stress, the test specimen deformation comes back to start position (unloading). In this case, the loading-unloading (one test cycle) stress-strain data is the test data. In other words, one test cycle is a loading-unloading process which is started from an initial strain and stress value and reaches a maximum stress or strain value (loading) and will come back to the start position (unloading). The cyclic test shown in Figure 4-3 is a test which is usually executed more than once and the maximum strain and stress of cycles can be changed during the test. The cyclic test results can give some extra information about the material behavior such as hysteresis and Mullins effect which is used to select an appropriate model (Bauman, 2012).

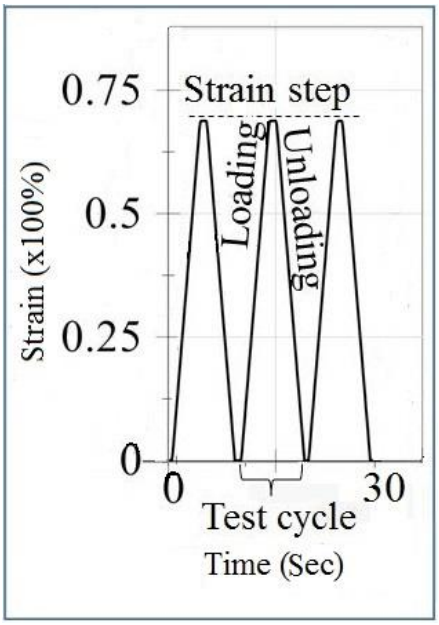

Figure 4-3: The cyclic uniaxial tensile test for one strain step. Three cycles which each cycle consists of loading and unloading process are shown here. The test specimen is stretched (loaded) 70% and then unloaded to get the start position in each test cycle again.

The FEM software ABAQUS generally needs only the monotonic test data such as loading test data for FEM simulations. On the other hand, performance of cyclic loading-unloading in addition to the loading test data, generates more data to get a better feeling about the material mechanical behavior. So, in the dissertation the cyclic tests are executed and their results will be discussed. Afterwards, the loading test's result is used in FEM software ABAQUS.

4.1.3 Uniaxial compression test

The ISO 7743 international standard and ASTM D575 describe the test process for the specification of compression stress-strain properties of rubber materials (ASTM D575, 2012; ISO 7743, 2011). In accordance with ISO 7743, there are two similar letters of A and B for both of test methods and test types. So, in the following, for these letters, the test type and test method should be noted and distinguished.

According to ISO 7743 there are four different test methods A, B, C and D. The test piece is a part of a product or a specimen with special dimensions divided into type A (a cylinder of diameter 29 ± 0.5 mm and height 12.5 ± 0.5 mm) and type B (a cylinder of diameter 17.8 ± 0.15 mm and height 25 ± 0.25 mm). Table 4-2 describes the different

methods and test pieces and their essentials to perform the compression test. The execution of the test methods A, B and C is the same, but the test specimen preparation is different. In method A, the metal plate surface should be lubricated. In method B, a bonded assembly of test specimen should be used. In method C the test specimen should be located centrally in the test machine. In method D the metal plate should be lubricated and the test specimen as a part of the product is positioned in the test machine.

Table 4-2: The overview of different types of test methods and test pieces for compression test. According to test method and test piece type, some test pieces need to be bonded to metal plates or to be lubricated to contact with metal plates.

Method	Test piece 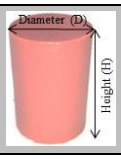	Metal plates lubricated	Metal plates bonded
A	A (cylinder of diameter 29 ± 0. 5 mm and height 12.5 ± 0.5 mm)	Yes	No
B	A	No	Yes
C	B (cylinder of diameter 17.8 ± 0.15 mm and height 25 ± 0.25 mm)	No	No
D	Part of a product	Yes	No

The execution of the test process in test methods A, B and C are the same. In these cases, the test speed is 10 mm/min and a maximum strain value of -25% should be achieved in the test. According to Figure 4-4, in four uninterrupted cycles the loading-unloading process is performed and the strain-stress values in the last cycle are considered as test results. The execution of method D is summarized to loading-unloading cycle at a speed of 10 mm/min with reaching a maximum strain of -30% (ISO 7743, 2011).

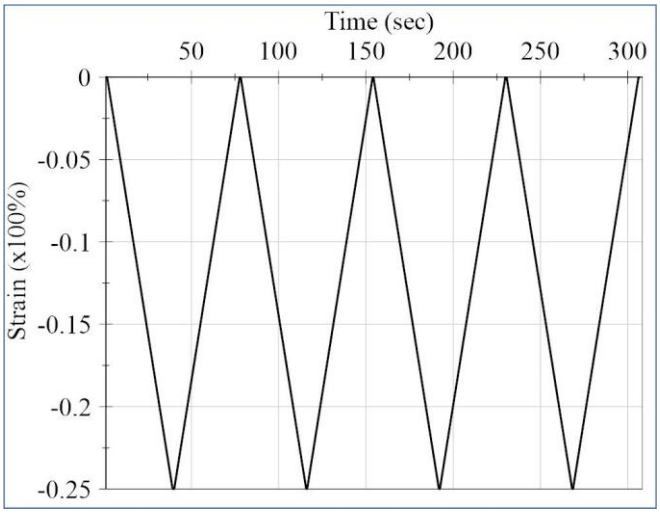

Figure 4-4: The strain versus time changes of compression test cycles in test methods A, B and C. Four different cycles (loading-unloading) are executed with the same maximum amount of strain. The last cycle (4th cycle) is selected to calculate the compression test results.

Method C and test piece B are selected to perform the compression tests because of the advantages that are described in the following. The test results of this method are independent of shape and the lubrication situation of test pieces. The test piece B is more suitable than the other pieces to specify the material properties with the method C (ISO 7743, 2011).

4.1.4 Planar tensile test

The planar tensile test result is an effective test results to find the material behavior and the strain energy function model and parameters. The test execution in the planar test is nearly similar to the uniaxial tensile test, but the test specimen size is different and it is a wide sheet of material. In a wide specimen, the in-plane displacement is in the loading direction through the specimen thickness. So, it proves the similarity of deformation of the test specimen with plane strain (Bergstroem, 2015). The results of the planar tensile test on hyperelastic materials are nearly similar to the pure shear test and they can be used instead of each other (Bergstroem, 2015).

The planar test specimen size is an important issue. Usually, the length per width of test specimen should be more than 5 (Bergstroem, 2015) to get suitable results, but the limitation of test instruments should be considered in this case.

The test specimen becomes thinner in the contact area with grip edges. So, the effective length of this area is increased with the utilization of strain. Then, to ignore this effect, the test area should be located in the middle of the test specimen with some distance from the machine grips (Bergstroem, 2015). Figure 4-5 shows a planar test specimen with dimensions of 60 mm (TW) x 8 mm (TL) and thickness of 1.7 mm. The test length should be marked and a video extensometer system should be used to measure the planar specimen deformation.

Figure 4-5: The planar test specimen, fixed with grips. The black solid lines show the measurement lines which are marked to be detected by the videoextensometer. The test width (TW) and test length (TL) of the measurement area are clarified graphically.

4.1.5 Poisson's ratio

Usually, the poisson's ratio is used in the simulation process of FEM software ABAQUS. It has a limited effect on the mechanical behavior. So, the accurate measurement of poisson's ratio is not an effective parameter to have an accurate simulation (Bergstroem, 2015). The test specimens in the poisson's ratio are similar to the uniaxial tensile test specimens (ASTM D638, 2014). The videoextensometer system can measure the strain in axial and transverse directions. The poisson's ratio is the absolute value of transverse strain to the corresponding axial strain (equation (4-1)). The poisson's ratio should be calculated in the axial strain range of 0.0005 - 0.0025 mm/mm or 0.05 - 0.25 %, when the stress-strain behavior of the material in both directions is not linear. Therefore, the poisson's ratio according to equation (4-2) in the axial strain of 0.002 is calculated when it is not possible to detect a clear (constant) proportion (ASTM D638, 2014).

$$\vartheta = \left| \frac{d\varepsilon_t}{d\varepsilon_a} \right| \tag{4-1}$$

$$\vartheta_c = \left| \frac{d\varepsilon_t}{d\varepsilon_a} \right|_{\varepsilon_a = 0.002} \tag{4-2}$$

In the next part, the measurement setup according to the described test methods of this chapter are presented.

4.2 Measurement setup

This part clarifies the test environment condition in the beginning. Then, the test machine specifications for different tests are described. Afterwards, the type of test specimens and their production method are explained. Then, the execution of different test methods are presented.

4.2.1 Temperature and relative humidity

The mechanical characteristic tests of silicone rubber were executed in an air-conditioned laboratory (IDD Klimalabor) which was adjusted according to DIN 50014.

The different rubber material test methods and the standard conditions for testing of rubber materials (ASTM D1349) describe standard laboratory atmosphere temperature and relative humidity of tests. They shall be 23 ± 2 °C and 50 ± 10 %RH (ASTM D1349, 2014). Figure 4-6 and Figure 4-7 show temperature and humidity of the IDD air-conditioned laboratory for a period of one day as an example. These values are measured with two different sensors which were located in two different positions to support whole environment. The test machine for the silicone rubber test specimens is located near to sensor number 2. Therefore, the temperature and humidity values of sensor number 2 (temp 2 and RH 2) are close to the exact values of the test environment. A day's working time (08:00 - 18:00) is highlighted in Figure 4-6 and Figure 4-7 to have a more realistic comparison.

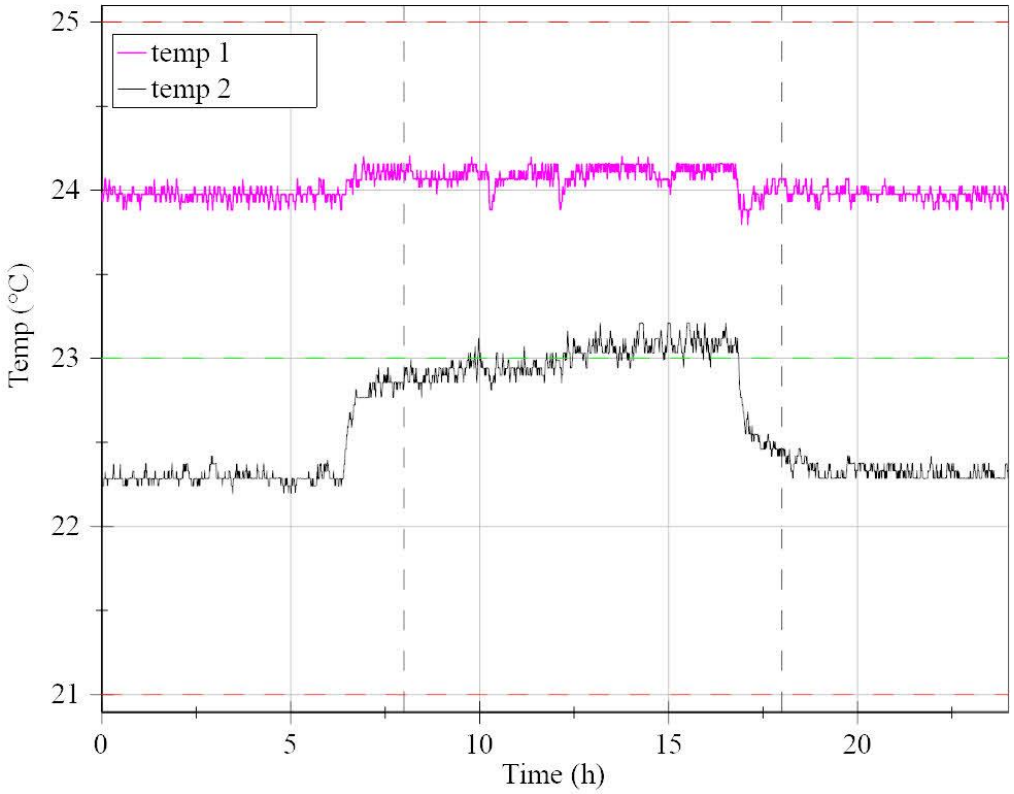

Figure 4-6: The temperature in the air-conditioned laboratory measured on 31.01.2018. The horizontal axis is a daytime from 00:00 until 24:00. The vertical axis is the temperature in °C. The red dashed lines are the minimum and maximum tolerance of temperature 23 ± 2 °C according to the test standards. The green dashed line in the middle is the exact standard temperature. The black (temp 2) and purple curves (temp 1) are the measured values with two different sensors. The two vertical dashed lines show a time duration between 08:00 until 18:00. The measured values prove that the temperature values during the experiments are in the standard range.

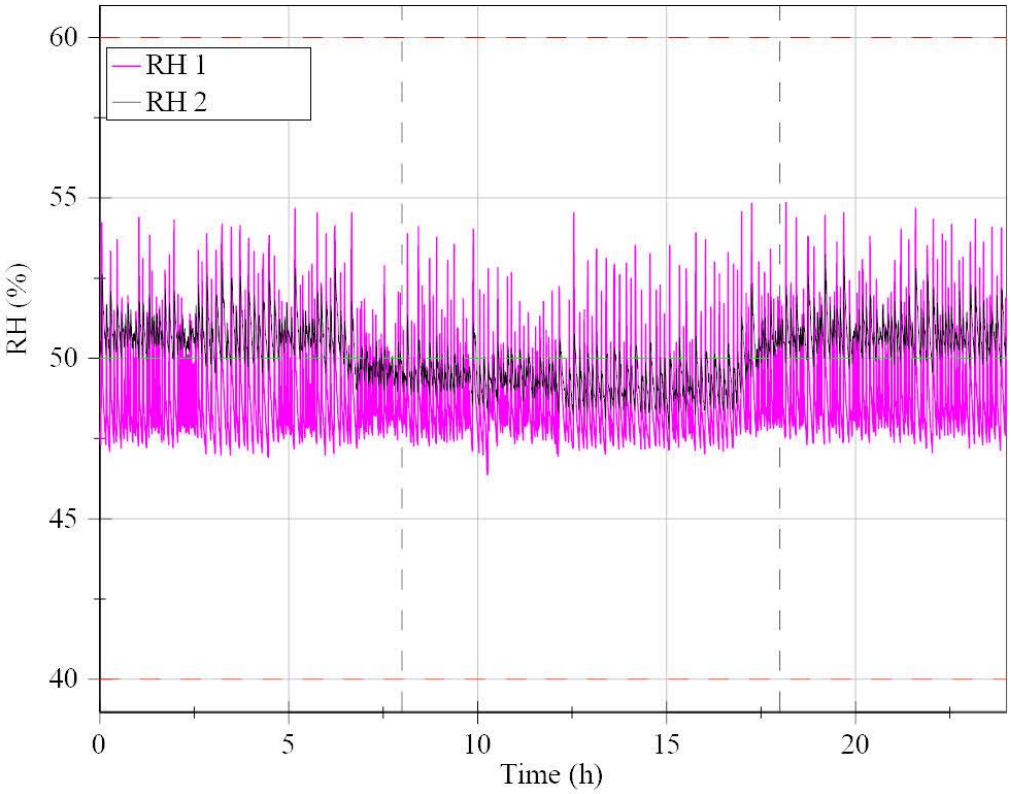

Figure 4-7: The relative humidity in the air-conditioned laboratory measured on 31.01.2018. The horizontal axis is a daytime from 00:00 until 24:00. The vertical axis is the relative humidity in percentage (%). The red dashed lines are the minimum and maximum tolerance of relative humidity 50 ± 10 % according to the test standards. The green dashed line in the middle is the exact standard relative humidity. The black (RH 2) and purple curves (RH 1) are the measured values with two different sensors. The two vertical dashed lines show a time duration between 08:00 until 18:00. The measured values prove that the relative humidity values during the experiments are in the standard range.

Figure 4-6 and Figure 4-7 prove the validity of test environment temperature and humidity with the standard situation.

4.2.2 Test machine

The mechanical tests were performed with a Zwick Z050 test machine which is equipped with accurate measurement devices. The cross head speed can be varied between 0.0005 - 2000 mm/min with ±2 µm position repetition and 27 nm travel resolution accuracy. The test machine is equipped with a high accurate force sensor to measure the force values precisely. The relative accuracy of the force sensor is 0.25 % of the measured value (Zwick, 2018).

The grips are used in the execution of uniaxial tensile and planar tests. Figure 4-8 shows a test grip which is used here. In this figure, a test specimen was fixed between the clamps to perform a test. The grip's role is to clamp and prevent the sliding of the test specimen in the clamped area.

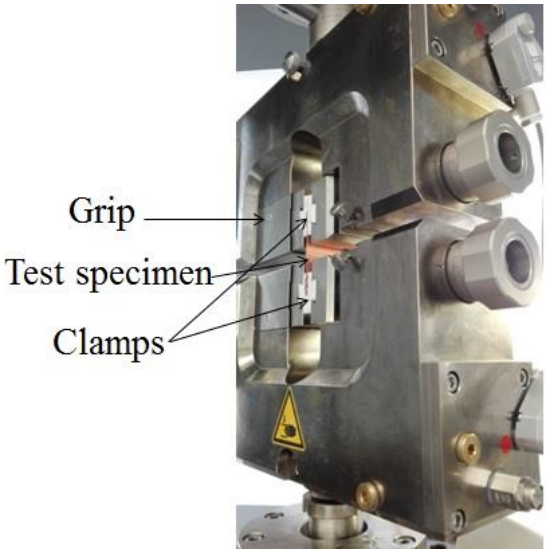

Figure 4-8: The uniaxial tensile test grip. Clamps are assembled on the grip to fix a test specimen. The grip, clamps and test specimen are shown here.

It was mentioned in chapter 4.1.2 that the uniaxial tensile strain of test specimens is measured with a designed video (non-contact) extensometer. Figure 4-9 shows related variables of a test specimen which are measured in video extensometer. The software performs image processing of the video recorded during a test. It detects marked lines on a test specimen and measures the distance between marked positions in all video frames to calculate the strain in the axial direction during a uniaxial tensile test. On the other hand, it measures the test specimen width changes to get the strain in the transverse direction during the test. Finally, the strain in axial and transverse (for poisson's ratio) directions can be calculated during a uniaxial tensile test. The camera system is shown in Figure 4-10.

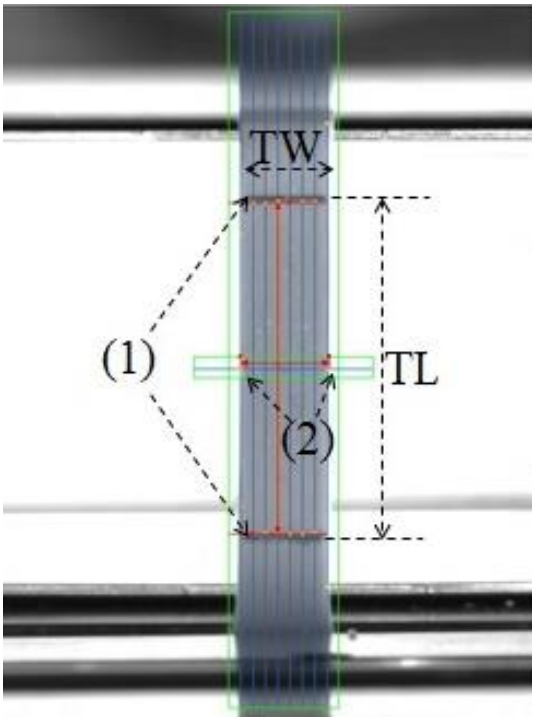

Figure 4-9: The view of a test specimen in the video extensometer. The marked lines on a test specimen in the axial direction (1), the marked lines in the transverse direction (2), test length (TL) and test width (TW) are detected with the software. The recorded videos in uniaxial tensile tests are processed to calculate the strain changes during a uniaxial tensile test.

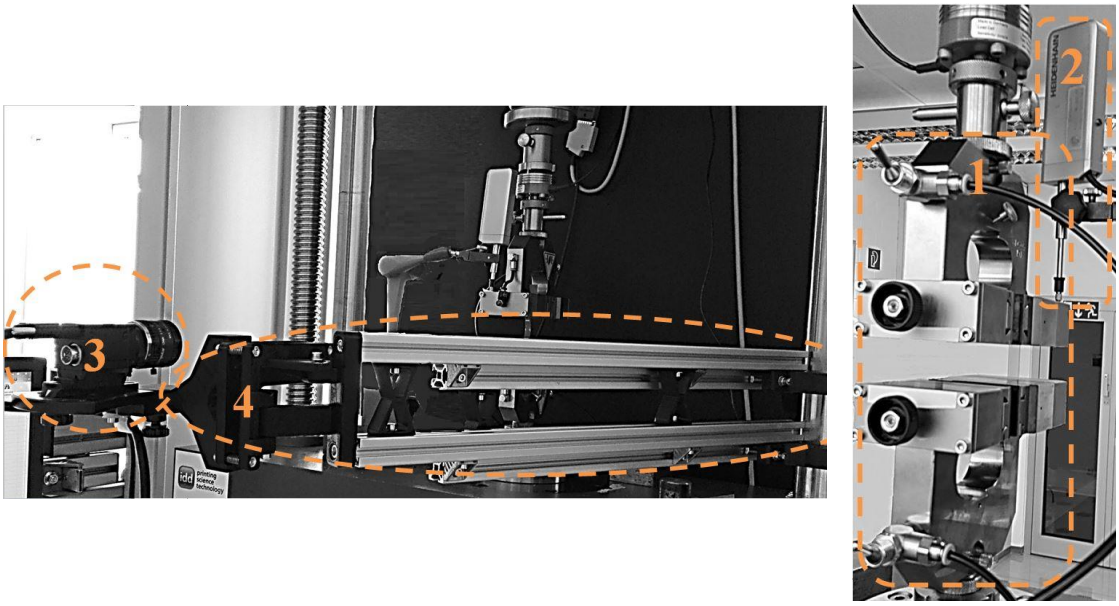

Figure 4-10: The test machine. It can be used to perform uniaxial tensile, compression and planar tests. The test grip (1) and length gauge (2) in left side and camera (3) and camera holder (4) in right side are displayed here.

The compression platens are used in the compression tests. They are shown in Figure 4-11. Often, the bottom platen is called platform. To measure the compression strain, the compression platen movement should be measured because a test specimen is compressed between the compression platen. A high accurate length gauge is used to measure the strain in compression. Here, the length gauge Heidenhain-Metro MT 2581 with 0.2 µm repetition accuracy and 50 nm resolution is used to measure the compression strain.

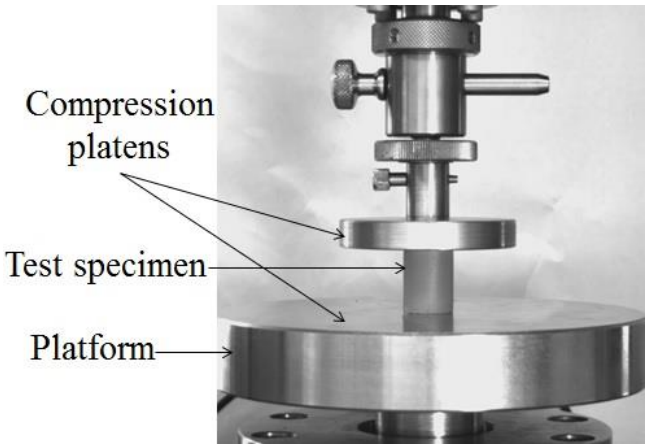

Figure 4-11: The compression test platens. The platens of compression and test specimen are shown here. The bottom platen is called platform.

The test specimens are positioned in the test machine to perform a test. In the next part, a production method of test specimens is described.

4.2.3 Test specimens

4.2.3.1 Types of test specimens

According to chapter 4.1, the following test specimens are selected. The dumb-bell test specimen type 1 is used for the uniaxial tensile test and poisson's ratio tests. The cylindrical test specimen type B is selected for uniaxial compression test. A plane with test width 60 mm, test length 8 mm and thickness 1.7 mm is chosen for planar test.

4.2.3.2 Test specimens production method

The test specimens are produced by a molding method. The negative forms of test specimens are designed and drawn in NX 10.0 software. Then, the negative forms of dumb-bell and cylindrical test specimens are printed by using a stereolithografic 3D printer (Formlabs Form 2, PreForm software for pre-processing). Afterwards, a production of test specimens is ordered at Tampo-Technik company to get the test specimens from the same material produced under same conditions as the final printing pad. Figure 4-12 shows the steps to prepare the uniaxial tensile, compression and planar test specimens from first row to the third row or up to down with shapes of dumb-bell, cylindrical and flat, respectively. The technical drawing, prepared molds and produced silicone rubber test specimens were positioned in (a), (b) and (c) from left to right. According to this order, the standard forms of test specimens are drawn. Then, the molds are prepared and the silicone test specimens are produced. The requested hardnesses of test specimens are 3, 6, 12 and 18 Shore A.

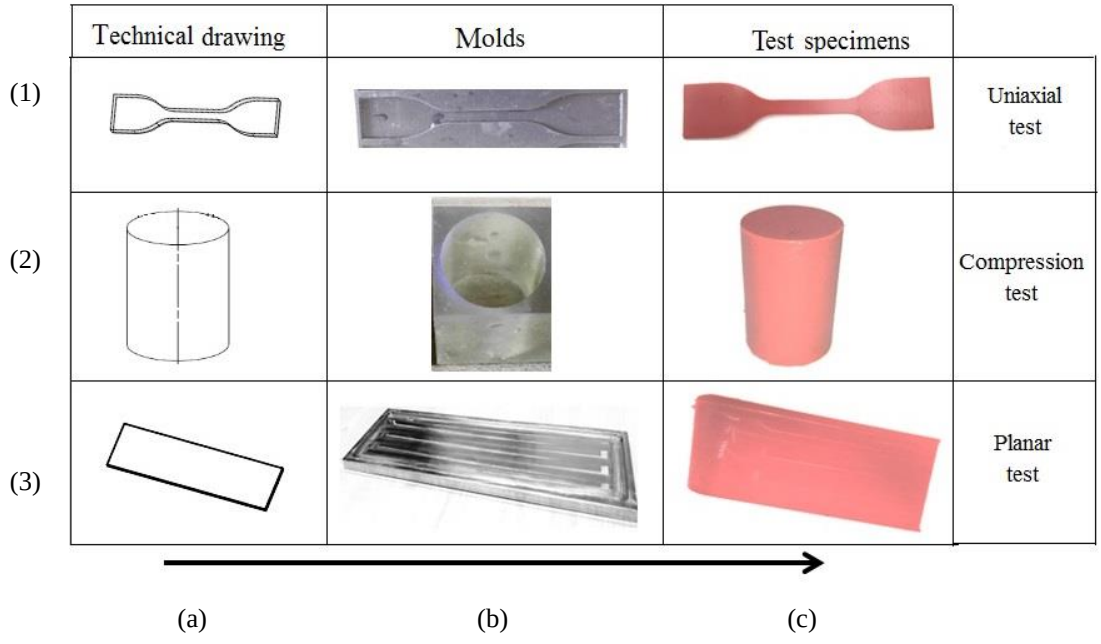

Figure 4-12: The test specimens preparation steps. The technical drawing (a), molds (b) and test specimens (c) show the order of steps for each type of test. From up to down (1 to 3), the uniaxial tensile, compression and planar test specimens preparation steps are located in each horizontal group.

Figure 4-13 shows the table of test specimens and designed pads used in this dissertation. The test specimens are used to perform uniaxial tensile, planar and

compression tests. The designed pads are applied to execute the printing steps in order to measure the force during the printing process. Its results will be compared with simulation results. The related shapes of test specimens and their hardnesses are presented in this figure. A number is clarified in a row and column cross section. It is the number of test specimens and pads which will be tested in each case. Here, it is a constant value of three. It shows in each case three test specimens and pads will be examined.

Designed pads and test specimens			Hardness (Shore A)			
			3	6	12	18
Shape	pad 1	Fig. 1	3	3	3	3
	pad 2	Fig. 2	3	3	3	3
	pad 3	Fig. 3	3	3	3	3
	pad 4	Fig. 4	3	3	3	3
	planar test specimen	Fig. 5	3	3	3	3
	cylindrical test specimen	Fig. 6	3	3	3	3
	dumb-bell test specimen_T1	Fig. 7	3	3	3	3

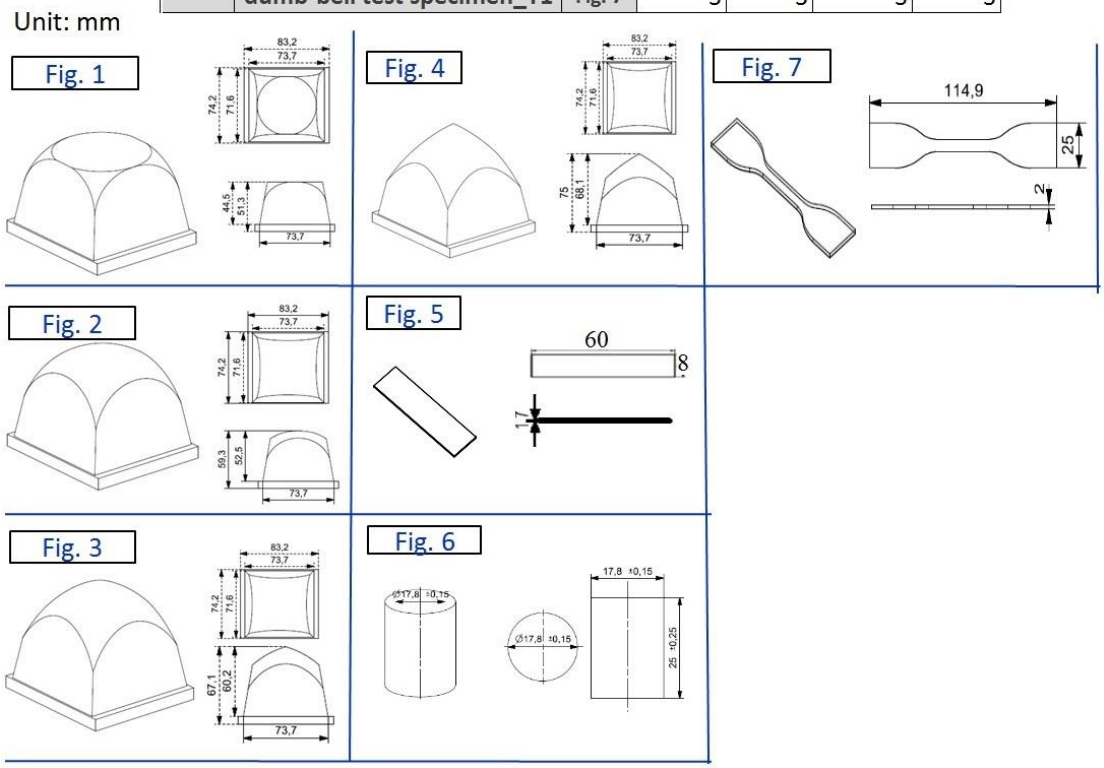

Figure 4-13: The test specimens and designed pads used in this dissertation.

The hardness of cylindrical test specimens will be measured in the next part to compare the produced test specimen hardness with requested hardness.

4.2.3.3 Verification of hardness of test specimens

The hardness measurement method was described in chapter 2.2.4. In order to measure the hardness of a test specimen, its thickness should be more than 6 mm. Therefore, only the compression test specimens have the possibility of hardness measurement because of their geometry and size.

The (ASTM D2240, 2015) standard is considered as the hardness measurement method with some small changes according to the limitation of pad hardness measurement. In the measurement of the pad hardness, the suggested load with a value of 1 kg is not applied. The measurement of pad hardness with the use of this load is not possible because of the pad geometry. In this case, Durometer is located perpendicular on one surface of a pad according to the standard. Then, Durometer is pressed on the pad surface in perpendicular direction. It is continued until the appearance of a complete contact between the flat circular surface of presser foot and the surface of the measurement area. Afterwards, this situation is kept constant for a while which is called holding time. A holding time of 1 ± 0.1 s is used to read the Durometer value. The holding time can be changed according to the agreement between supplier and user (ASTM D2240, 2015). So, the same method is used to measure the hardness of cylindrical test specimens.

In this case, the hardness of three test specimens is measured for each hardnesse. Table 4-3 shows the results of measurements. The ordered hardness is the hardness value which was ordered at Tampo-Technik company for production. The measured hardness is a range between minimum and maximum values which their hardnesses are measured.

Table 4-3: The comparison of hardness between the ordered and prepared compression test specimens.

Ordered hardness (Shore A)	Prepared hardness (Shore A)		
	Minimum	Maximum	Tolerance
3	2.5	3.5	±0.5
6	5	7	±1
12	13	13	+1
18	19	19	+1

A distance between minimum and maximum values of hardnesses which are shown in this table, is less than or equal to 1 Shore A. It is mentioned that a tolerance of ±1 Shore A in the measurement device is acceptable according to standard notifications (ASTM D2240, 2015). So, the hardness of prepared test specimens is in the acceptable range.

4.2.4 Test method execution

The following test setups are selected according to chapter 4.1.

Uniaxial tensile test setup

The dumb-bell test specimen type 1 is used to perform the uniaxial tensile test and poisson's ratio test. The test length of 25 mm is marked symmetric to the center point of test specimen according to related standards (ASTM D412, 2016; ISO 37, 2012). Figure 4-16 (a) displays this test specimen.

In order to investigate the stress-strain behavior of silicone rubber the cyclic uniaxial tensile test is performed. Each cycle shows an increasing strain (loading or extension) and decreasing strain (unloading or retraction) in time. According to cyclic load application the different strain steps in the special number of iterations were applied. In this case, four different strain steps 30%, 70%, 110% and 140% are considered. The pad usually is deformed less than 50% during the printing process based on experience, but in order to use the test results for new designed pads and to get a better understanding for the silicone rubber behavior, the described values of strain steps are the choice. In each step, the loading-unloading process is repeated three times to have three iterations.

Totally, 12 cycles were executed. Figure 4-14 shows the strain changes of one test specimen according to test time as an example in order to describe the uniaxial tensile cycles and their iterations. It is a cyclic uniaxial tensile test performance method which is selected to detect mechanical specification of silicone rubber material with different hardnesses in a uniaxial tensile test.

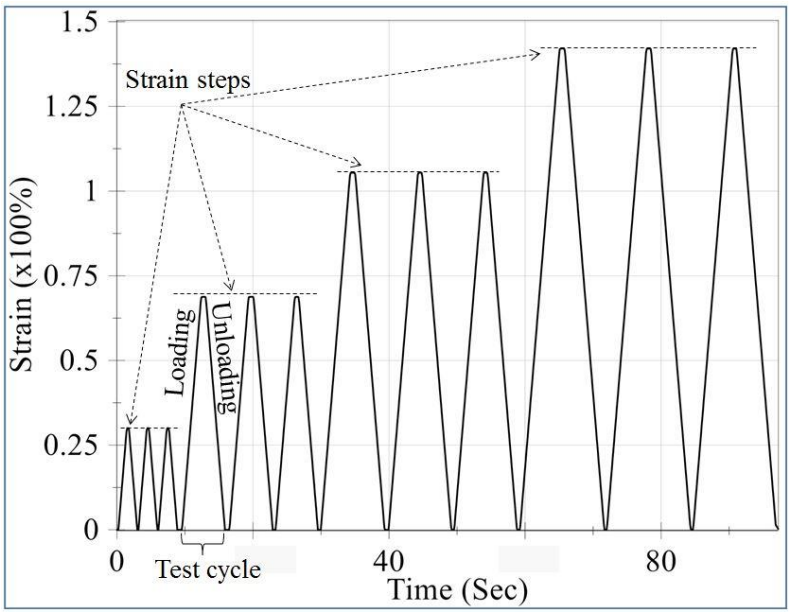

Figure 4-14: The uniaxial tensile test cycles (loading-unloading) procedure. It shows strain versus time. It consists of 12 test cycles in four different strain steps (30%, 70%, 110% and 140%) that is executed on each test specimen.

In each strain step the hysteresis and Mullins effect are the parameters that can be appeared. Some other rubber specifications that do not affect on silicone rubber behavior during printing will not be discussed. More descriptions about other rubber specifications are described in (Bauman, 2012).

To calculate the results, an average value between test results of three different cycles of each step is calculated. Then, test results of three different test specimens will be averaged to get the strain-stress curve. Further, in the same method, in different test specimens between different test cycles results, minimum and maximum values are calculated which it is considered as a deviation of the test results.

Uniaxial compression test setup

Here, the compression test is performed according to ISO 7743 which was described in chapter 4.1.3. In the compression test, the type B test specimens which has a cylindrical shape with diameter 17.8 ± 0.15 mm and height 25 ± 0.25 mm is used. Figure 4-16 (b) shows this test specimen. The test method C is executed for compression test.

In this test method, four cycles with the strain step of -25% are executed on a test specimen with a special hardness which is shown in Figure 4-15. Then, the last cycle is selected as a compression test result of this test specimen. Afterwards, the same process will be performed for two more test specimens with the same hardness. Thereafter, a median, minimum and maximum of test results for these three test specimens is calculated. These values are considered as the compression test result for this hardness.

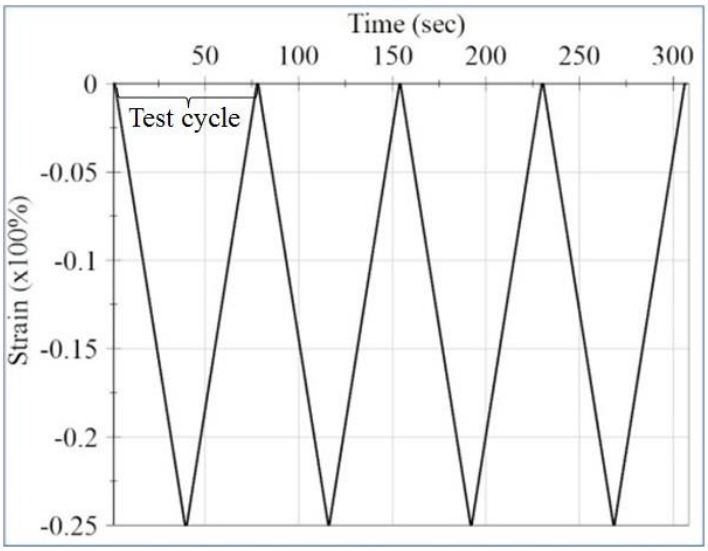

Figure 4-15: The compression test cycles (loading-unloading) procedure. The axis are strain versus time. It consists of four test cycles with -25% strain that is executed on each test specimen.

In this test method, the force will be divided by the original cross-section area to calculate the strain. The compression strain is expressed as the test specimen's deformation divided by the original dimension in the direction of applied force (ISO 7743, 2011).

Uniaxial planar test setup

The planar test specimen with test width 60 mm, test length 8 mm and thickness 1.7 mm is produced and marked to perform the planar tensile test. Figure 4-16 (c) illustrates the planar test specimen. The test method in planar test is similar to the uniaxial tensile test. In this case, the shape of the test specimen is displayed in Figure 4-5 (c). In this figure, the dashed line on the test specimen schema shows the test length that is marked in test execution. The test method and test specimen dimensions were described in above chapters 4.1.4 and 4.1.2. A maximum strain of 55% is applied to tension the test specimen.

Poisson's ratio calculation setup

According to chapter 4.1.5, the transverse strain is calculated during the execution of tensile test to calculate Poisson's ratio. The video extensometer system measures the width changes of test specimens in a perpendicular direction to axial movement. The test specimen and test setup is similar to uniaxial tensile test which was described above. Figure 4-16 (a) displays this test specimen.

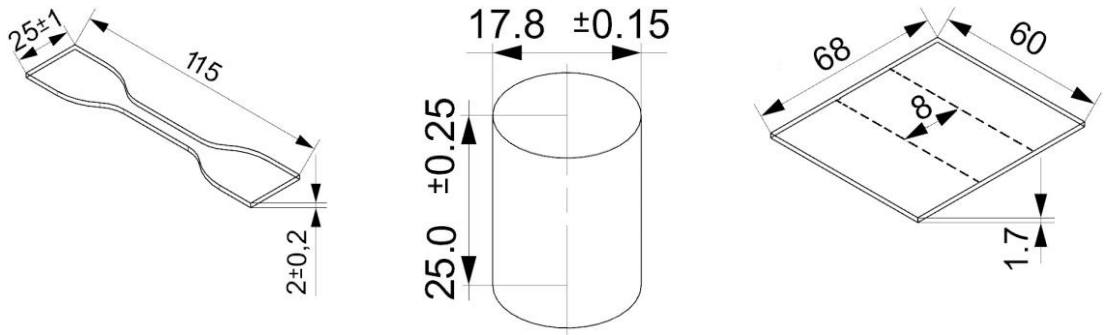

(a) (b) (c)

Figure 4-16: The dimensions of selected test specimens. The dumb-bell test specimen type 1 (a), cylindrical test specimen type B (b) and planar test specimen (c) are shown here. The dashed line on test specimen in (c) shows the test length. The dimension unit is mm.

In order to decrease the measurement and material properties errors for all hardnesses (3, 6, 12 and 18 Shore A) and for each test type (uniaxial tensile, uniaxial compression, planar tensile and poisson's ratio tests), at least three test specimens are tested.

Equation (4-3) shows the calculation method of stress considered for all test results.

$$\sigma = \frac{F}{A_0} \tag{4-3}$$

The stress is displayed by σ parameter in this equation. An engineering stress is presented for stress values according to related standards for uniaxial tensile, uniaxial compression and planar tests. So, an original cross-sectional area of a test specimen is considered as A_0 parameter. The force sensor of the test machine measures an applied force on the test specimen. It is shown by F parameter in equation (4-3).

A description of abbreviation letters of different test specimens is displayed in Table 4-4. There are different test specimens which are used in different test methods. This abbreviation shows a test specimen hardness, geometry and number which are located instead of first, second and third letters. First position ("S") is a position for amount of test specimen hardness. Second position is related to geometry of test specimen. The geometry depends on the test method. It is shown with "T", "C" and "P" for uniaxial tensile, compression and planar tests. The third position is related to the test specimen number. The test specimen number is related to each of three test specimens which have the same geometry and hardness. It is shown with 1, 2 and 3. "123" in third position shows an average in the test results of test specimens with numbers of 1, 2 and 3.

Table 4-4: The description of abbreviation letters used in test results. The "No." in the column of parameters is an abbreviation for number.

Test method	Test specimen geometry	Abbreviation	Parameters
Uniaxial tensile test		ST_n	S = 3, 6, 12, 18 Shore A hardness n = 1, 2, 3, 123 1, 2, 3: Test specimen No. 123: Average of test specimens No. 1, 2 and 3.
Uniaxial compression test		SC_n	
Planar tensile test		SP_n	

The measurement setup was described above in different parts. Afterwards, the test results are presented in the next part.

4.3 Test results of silicone rubber material

4.3.1 Results of uniaxial tensile tests

Here, the strain-stress calculation method for 3 Shore A silicone rubber is described in detail and afterwards for other hardnesses only the final results will be described. There are general rules and notations in the following figures which are described here for all. The vertical axis is the stress in MPa and the horizontal axis is the strain which should be multiplied by 100 to get the percentage values of strain. The four vertical dashed lines show the strain steps. The "Test specimen No." describes the name (which classified by numbers) of the test specimen. The hardness of test specimens is written in "Shore A". There are three different colors and line types for the curves. The black solid lines, pink dashed lines and turquoise dashed lines are related to average, minimum and maximum stress values in the groups of data which are averaged. The curves in each figure relate to different test cycles for each test specimen (e.g. Test specimen No. 1) or the average of results of different test specimens (e.g. Test specimens No. 1, 2, 3).

Figure 4-17 shows the stress-strain results of the applied strain in 12 different cycles that was described in Figure 4-14.

In Figure 4-14, there are four different strain steps 30%, 70%, 110% and 140% which each of them is repeated three times. So, a cycle of loading-unloading with the strain step of 30% is repeated for three times on a test specimen with the name of "No. 1". Therefore, there are three stress-strain data for the test specimen "No. 1" according to three times of test repetition for the strain step of 30%. Then, an average, minimum and maximum between these three strain-stress data are calculated. Thereafter, for other steps of strain which are 70%, 110% and 140%, the same calculation process for the test specimen "No. 1" is performed. The results are displayed in Figure 4-17.

Each test cycle in strain steps of Figure 4-14 consists of two parts which are called loading and unloading. So, each loading and unloading parts have their own average, minimum and maximum strain-stress curves. Therefore, the minimum or maximum curves have a loading-unloading form, separately. This is the reason of observation of more than one minimum or maximum curve in the figures. So, there are average, minimum and maximum curves for loading in strain-stress results of Figure 4-17. In

addition, the average, minimum and maximum curves for unloading are observed in this figure.

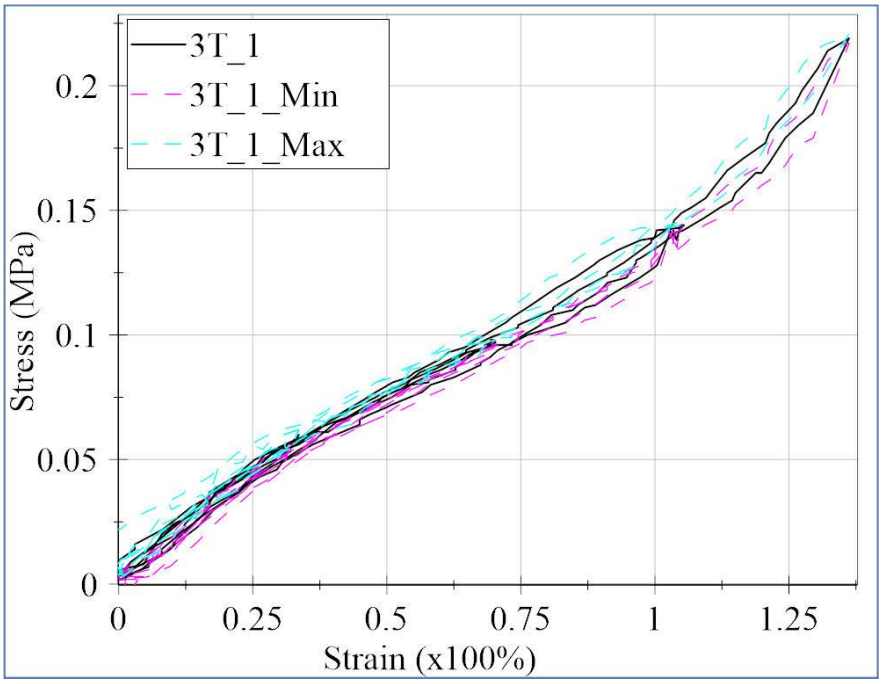

Figure 4-17: The stress-strain behavior of test specimen No. 1 with 3 Shore A hardness. It shows the minimum and the maximum deviation of stress values in addition to average stress for uniaxial tensile test cycles of Figure 4-14. The abbreviation letters were described in Table 4-4.

So, it shows the minimum and the maximum deviation of stress values in addition to average stress for three repetitions of cycles in each strain step. The deviation in the repetitions is very small. So, the stress-strain behavior does not change significantly when the material is used multiple times. The hysteresis effect is ignored, because the loading-unloading curves are nearly located on each other. There is not any Mullins effect because the curves have the same behavior in different strain steps.

Figure 4-17 is only related to one test specimen (No. 1) of 3 shore A hardness. Figure 4-18 shows the test results for specimens No. 2 and No. 3 with the same process as described in Figure 4-17. The strain-stress curves in these figures are not single lines because of the execution of loading-unloading tests. There is similarity in the test processes and there is a small deviation between the minimum, maximum and average curves. So, the curves are shown in smaller scale in the following to increase the efficiency of this dissertation.

Figure 4-18 shows the stress-strain behavior of silicone rubber with hardness of 3 Shore A. This figure relates to measured test data for two different test specimens with names of “Test specimen No. 2” and “Test specimen No. 3” which are shown in Figure 4-18 (a) and Figure 4-18 (b). The dashed line shows the maximum and minimum values of stress-strain and the solid line shows its average value. They are related to iteration of the same test process in each strain step for three times. There is a small deviation between the average curve and curves of minimum and maximum in both test specimens after repeating the test in each strain step for three times. It shows a high accuracy in measurement method because of similarity in test results after three times repetitions.

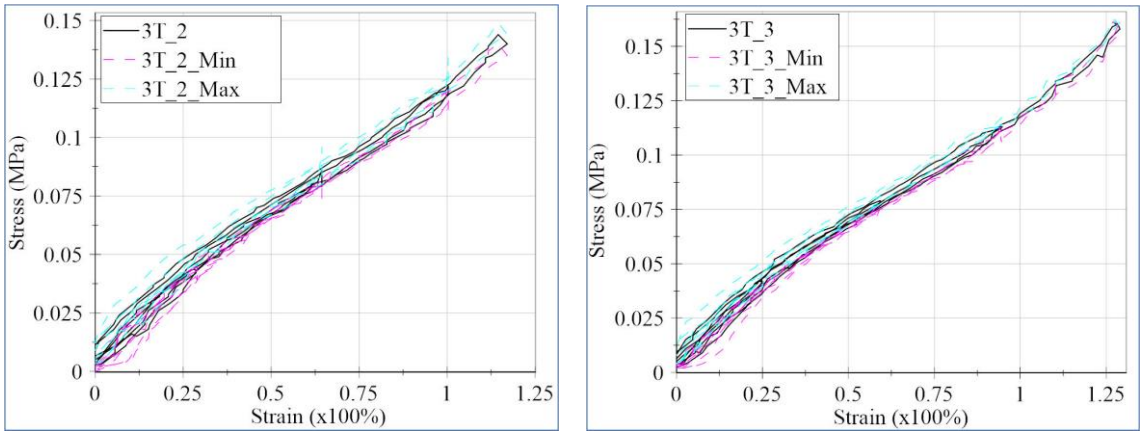

(a) (b)

Figure 4-18: The stress-strain behavior of test specimen No. 2 (a) and No. 3 (b) with 3 Shore A hardness. It shows the minimum and the maximum deviation of stress values in addition to average stress for uniaxial tensile test cycles of Figure 4-14. The abbreviation letters were described in Table 4-4.

Afterwards, an average value of the stress-strain behavior of all three test specimens (Figure 4-17, Figure 4-18 (a) and Figure 4-18 (b)) is calculated and is shown in Figure 4-19. It describes the stress-strain behavior of silicone rubber with hardness of 3 shore A. This figure gives an average value and the deviations of the experimental test results of three different test specimens which twelve test cycles (loading-unloading) in four different strain steps according to Figure 4-14 was performed on each of them.

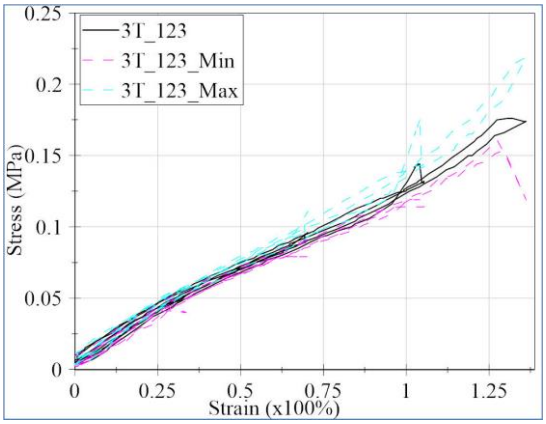

Figure 4-19: The uniaxial tensile stress-strain behavior of silicone rubber with hardnesses of 3 Shore A. The curves show the minimum and the maximum deviation of stress values in addition to the average stress for hardness of 3 Shore A. It is achieved with three repetitions of cycles in each strain step for three different test specimens. The abbreviation letters were described in Table 4-4.

This method is performed for other hardnesses, too. Figure 4-20 (a), Figure 4-20 (b) and Figure 4-20 (c) display the stress-strain behavior of silicone rubber with 6, 12 and 18 Shore A hardnesses. Here, the stress-strain behavior during a uniaxial tensile test, shows a nonlinear behavior. This issue confirms the nonlinear behavior of silicone rubber as a hyperelastic material for different hardnesses.

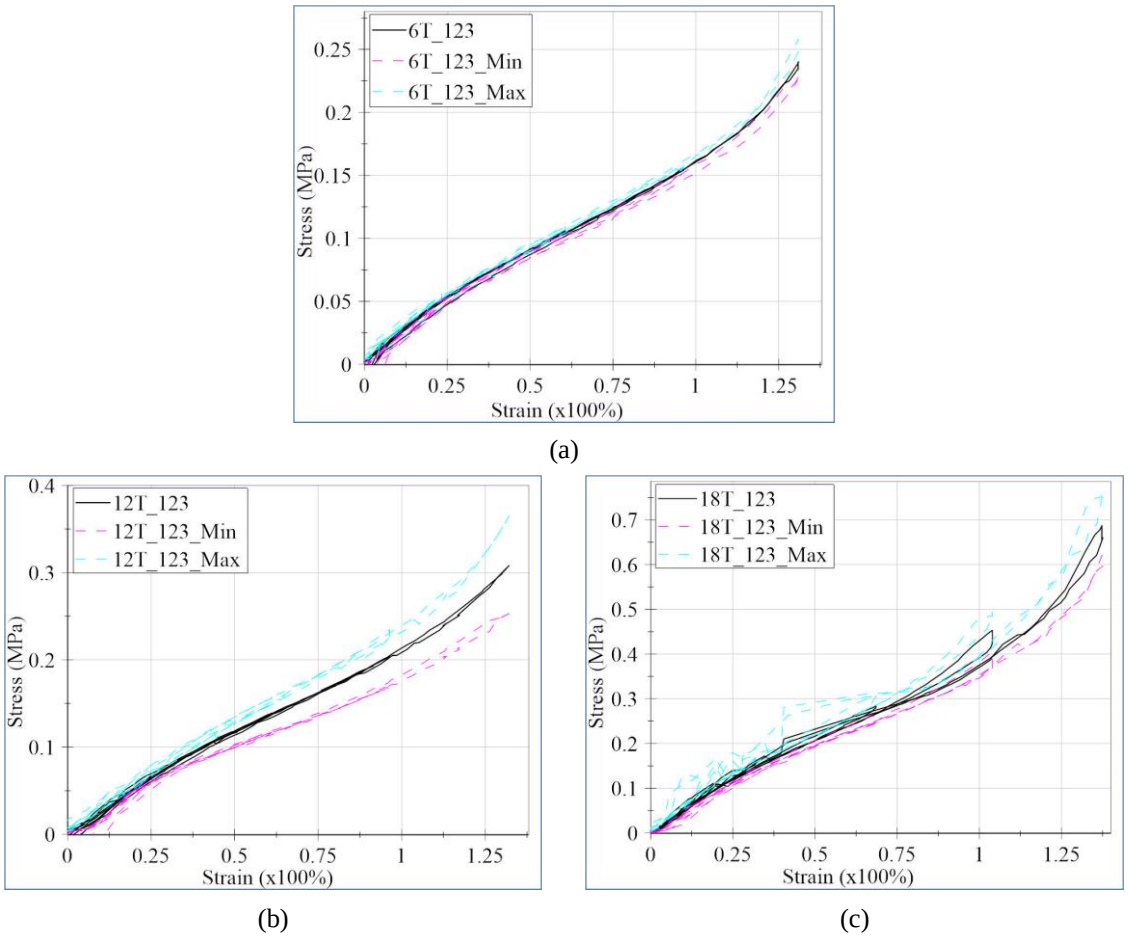

Figure 4-20: The uniaxial tensile stress-strain behavior of silicone rubber with hardnesses of 6 (a), 12 (b) and 18 (c) Shore A. In each segment of the figure, curves show the minimum and the maximum deviation of stress values in addition to the average stress for related hardness. In each hardness, it is achieved with three repetitions of cycles in each strain step for three different test specimens. The abbreviation letters were described in Table 4-4.

Figure 4-21 shows comparative diagrams of stress-strain curves with different hardnesses. The average of the measurements clarifies some material characterizes. The hardness increase of silicone rubber leads to an increase of stress in different steps of strain in a uniaxial tensile test. It means, in the same strain value, the required stress to tension a silicone rubber specimen with more Shore A hardness is more than for one with less Shore A. The harder pad has less tension during the tension of silicone rubber in the printing process with the use of same printing force per unit of element area. The pad deformation is usually less than 50% during the printing process. So, the strain working area for printing process can be considered till 70% and other data are more related to find the behavior of silicone rubber. In Figure 4-21, specially till 70% strain step, there is not a perceptible hysteresis effect, because there is not a sensible

difference between the stress of loading and unloading in the same strain value. In this range, when passing through the same loading and unloading path in different strain steps, the Mullins effect does not appear, too.

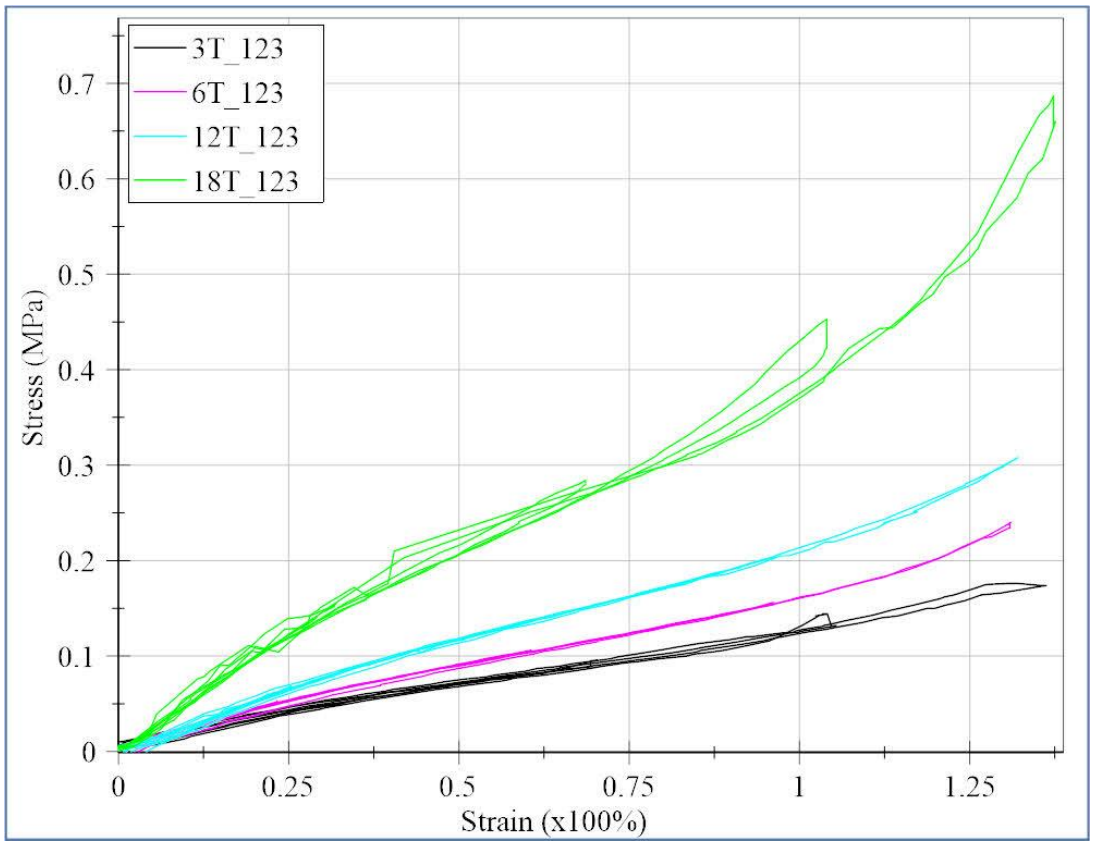

Figure 4-21: The uniaxial tensile stress-strain behavior of silicone rubber for hardnesses of 3, 6, 12 and 18 Shore A. The figure consists of the averaged data of different test specimens for each hardness. The abbreviation letters were described in Table 4-4.

The results of silicone rubber uniaxial tensile test with hardnesses of 3, 6, 12 and 18 Shore A were explained above. The compression test results are described in the next part.

4.3.2 Results of uniaxial compression tests

Figure 4-22 (a), (b), (c) and (d) show the compression results of silicone rubber 3, 6, 12 and 18 Shore A. It is a compression test performance method which is selected to detect mechanical specification of silicone rubber material with different hardnesses.

The stress value and related deviations (minimum and maximum stress) are presented in Figure 4-22. The small deviation in the results, presents a high similarity between the different test specimens in each hardness and it shows the stability of measurements in each hardness.

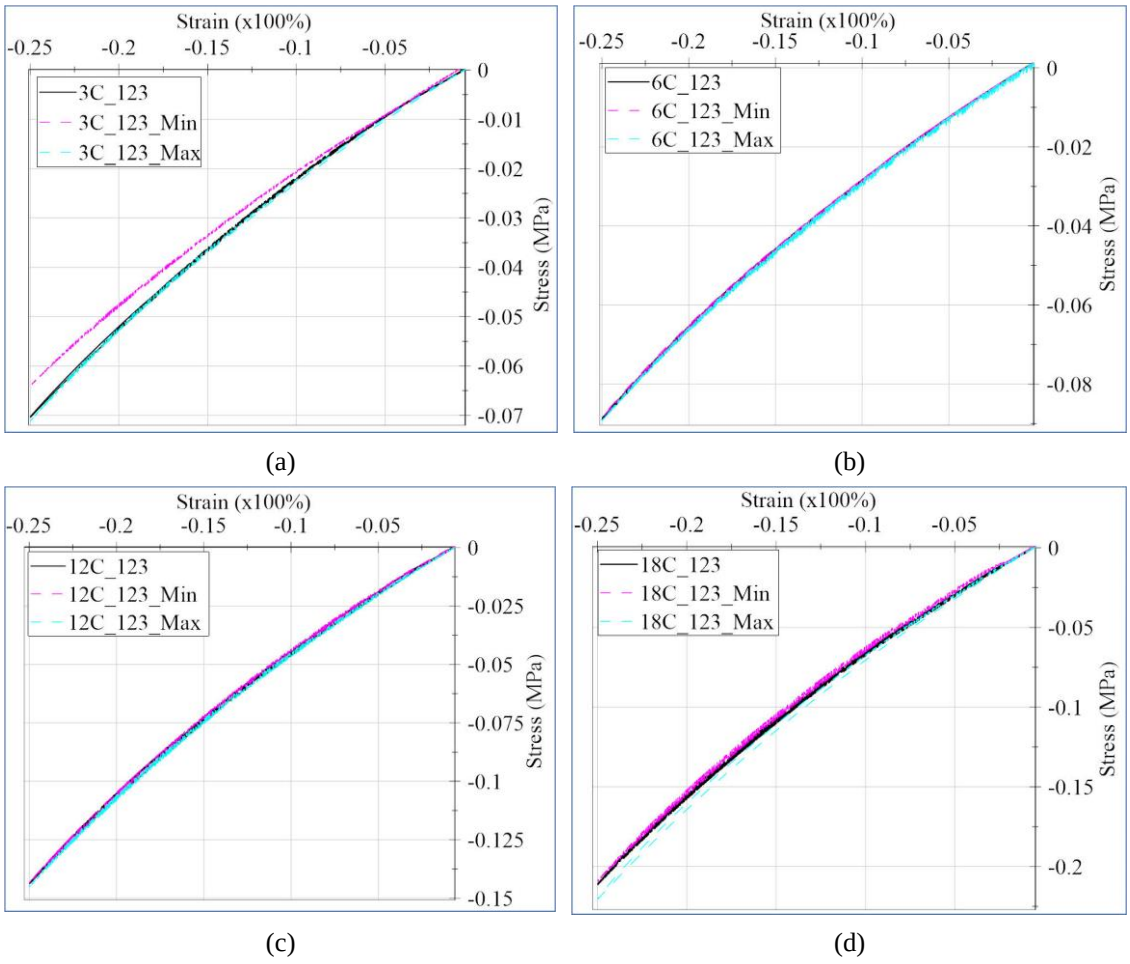

Figure 4-22: The compression stress-strain behavior of silicone rubber with hardnesses of 3 (a), 6 (b), 12 (c) and 18 (d) Shore A. In each segment of the figure, curves show the minimum and the maximum deviation of stress values in addition to the average stress for related hardness. In each segment, three different test specimens were examined. The abbreviation letters were described in Table 4-4.

The comparative curves of silicone rubber compression tests are given in Figure 4-23. Here, the stress-strain compression curves are plotted.

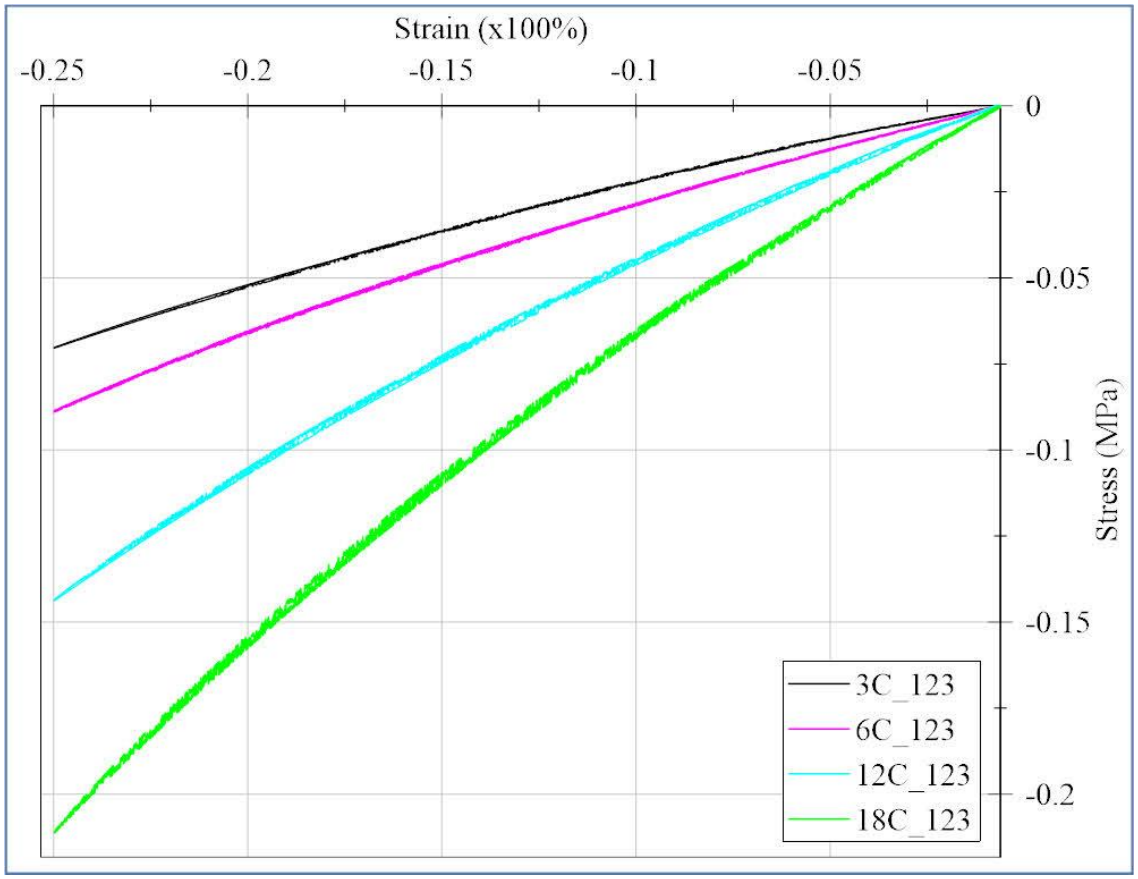

Figure 4-23: The compression stress-strain behavior of silicone rubber with hardnesses of 3, 6, 12 and 18 Shore A. The curves behaviors clarify the increase in stress with an increase of hardness in the same strain. The abbreviation letters were described in Table 4-4.

The uniaxial compression test results can be used to predict the compression behavior of silicone rubber during the applied force in the indirect gravure printing process.

4.3.3 Results of planar tests

Figure 4-24 (a), (b), (c) and (d) display the minimum, maximum and average stress-strain curves of the planar tests of specimens having 3, 6, 12 and 18 Shore A hardnesses. The results can be used to evaluate the material behavior in the simulation of the indirect gravure printing process. In different hardnesses, the stress increases with strain increment.

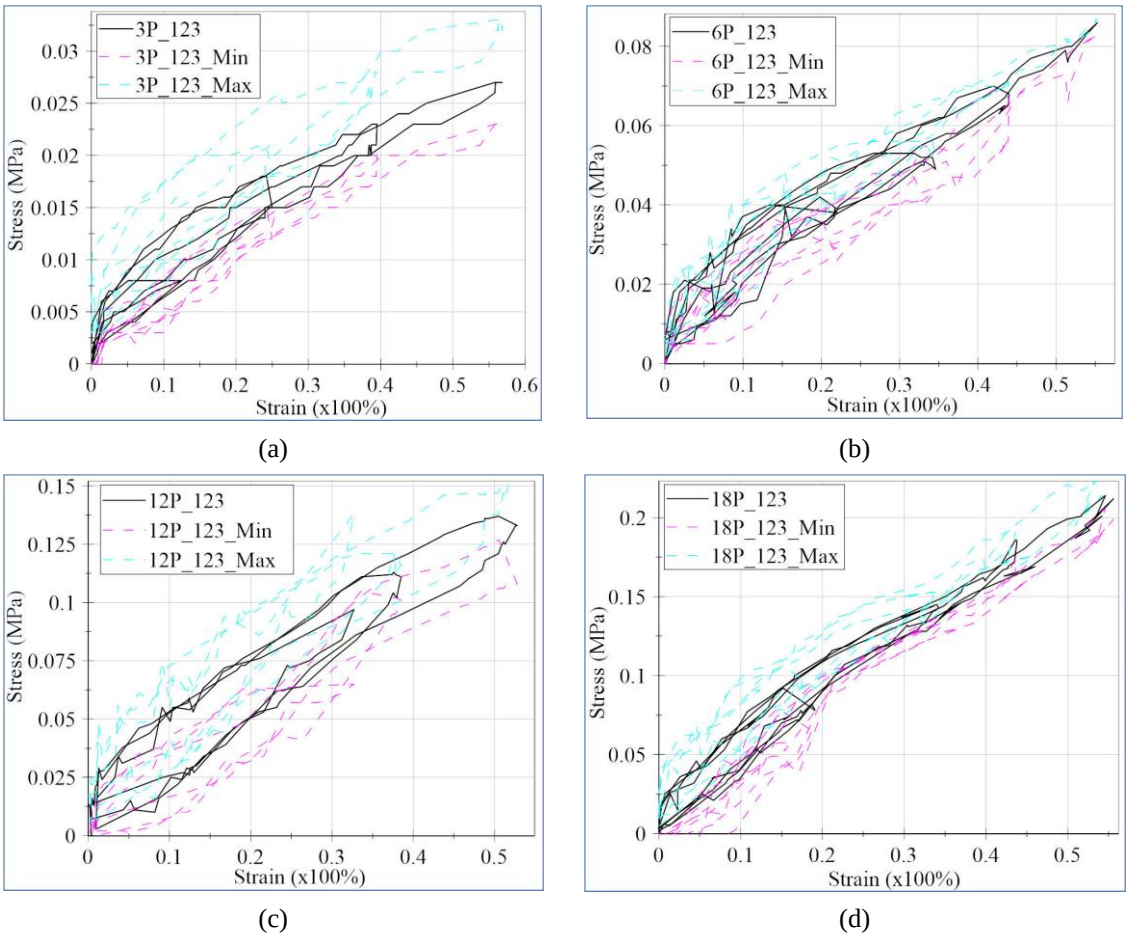

Figure 4-24: The planar tensile stress-strain behavior of silicone rubber with hardnesses of 3 (a), 6 (b), 12 (c) and 18 (d) Shore A. The average, minimum and maximum stress-strain curves of different hardnesses are presented in the figure. The abbreviation letters were described in Table 4-4.

Figure 4-25 shows the planar tensile test results for different hardnesses, averaged from three test specimens for each hardness. A maximum strain of nearly 50% will be considered in the simulation process and the cycle that is related to a strain of 55% is considered for evaluations. Also, these curves show the increase in stress with the increase of silicone rubber hardness in constant strain. For example, higher pressure should be applied to tension a planar specimen with hardness of 18 Shore A in comparison with the hardness of 3 Shore A while the same strain will be achieved.

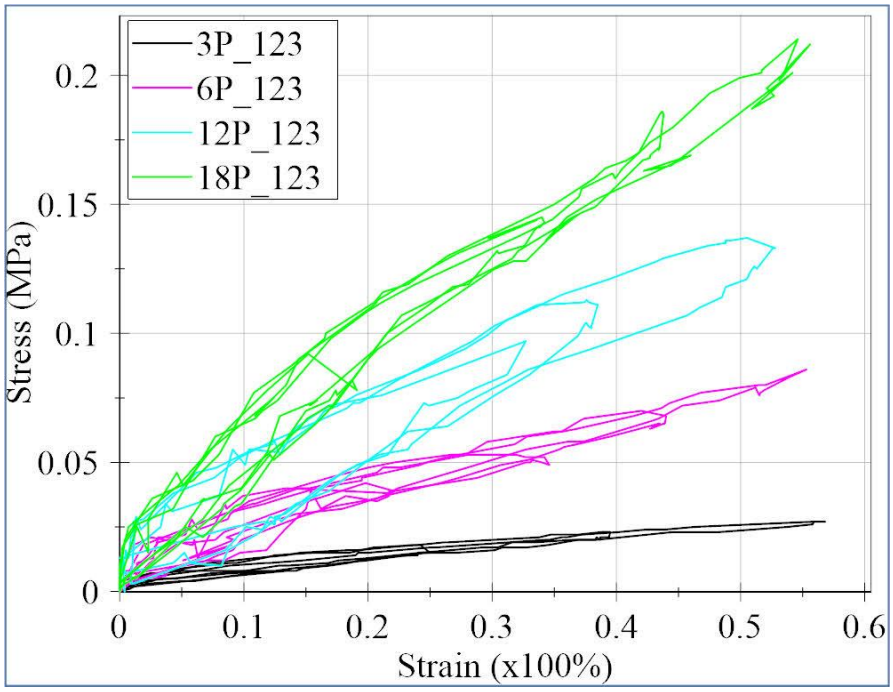

Figure 4-25: The planar stress-strain behavior of silicone rubber with hardness of 3, 6, 12 and 18 Shore A. The stress values are measured here from cycles with a maximum strain of 55%. The curves behaviors clarify the increase in stress with an increase of hardness in the same strain. The abbreviation letters were described in Table 4-4.

4.3.4 Calculation of Poisson's ratio

In chapter 4.1.5 the Poisson's ratio and its calculation method by use of transverse and axial strains were described. A transverse strain is a strain in a direction perpendicular to the direction of axial strain. An axial strain is the strain in axial direction during an execution of the uniaxial tensile test. The transverse strain is calculated in the uniaxial tensile test by dividing the width changes of test specimen by original width. The width of the test specimen is decreased during the execution of the uniaxial tensile test. It leads to achieve negative values for transverse strain.

Figure 4-26 is related to transverse strain versus the axial strain. The black solid line shows an average of test results. The average of test results of this figure is achieved with calculation of an average between the axial-transverse strain test results of three test specimen with same hardness and geometry. According to Table 4-4, it is called "S"T_123. Here, "S" is the silicone rubber hardness in Shore A. T_123 means an

average (123) between the test results of three test specimens with the same geometry and hardness in uniaxial tensile test method (T).

Further, in Figure 4-26, the related functions with the nonlinear curve fitting method based on "S"T_123 axial-transverse strain curves are calculated as Polynomial functions of second degree (see equation (4-4)), which related parameters are described in Table 4-5. The related curves to these functions are shown by red dashed lines in Figure 4-26. An abbreviation with a form of "S"T_NLF is related to the results of a nonlinear curve fitting method ("NLF") for tensile test ("T") with a hardness of "S" Shore A. In this case, "S" is replaced with Shore A hardness value. Here, "S"T_NLF curves are calculated based on "S"T_123 curves with a nonlinear curve fitting method. For example, according to Figure 4-26 (a), 3T_NLF is related to an axial-transverse strain curve of silicone rubber material with hardness of 3 Shore A in a tensile test method which is calculated according to nonlinear curve fitting method. 3T_NLF curve is calculated based on 3T_123 axial-transverse strain curve by a nonlinear curve fitting method.

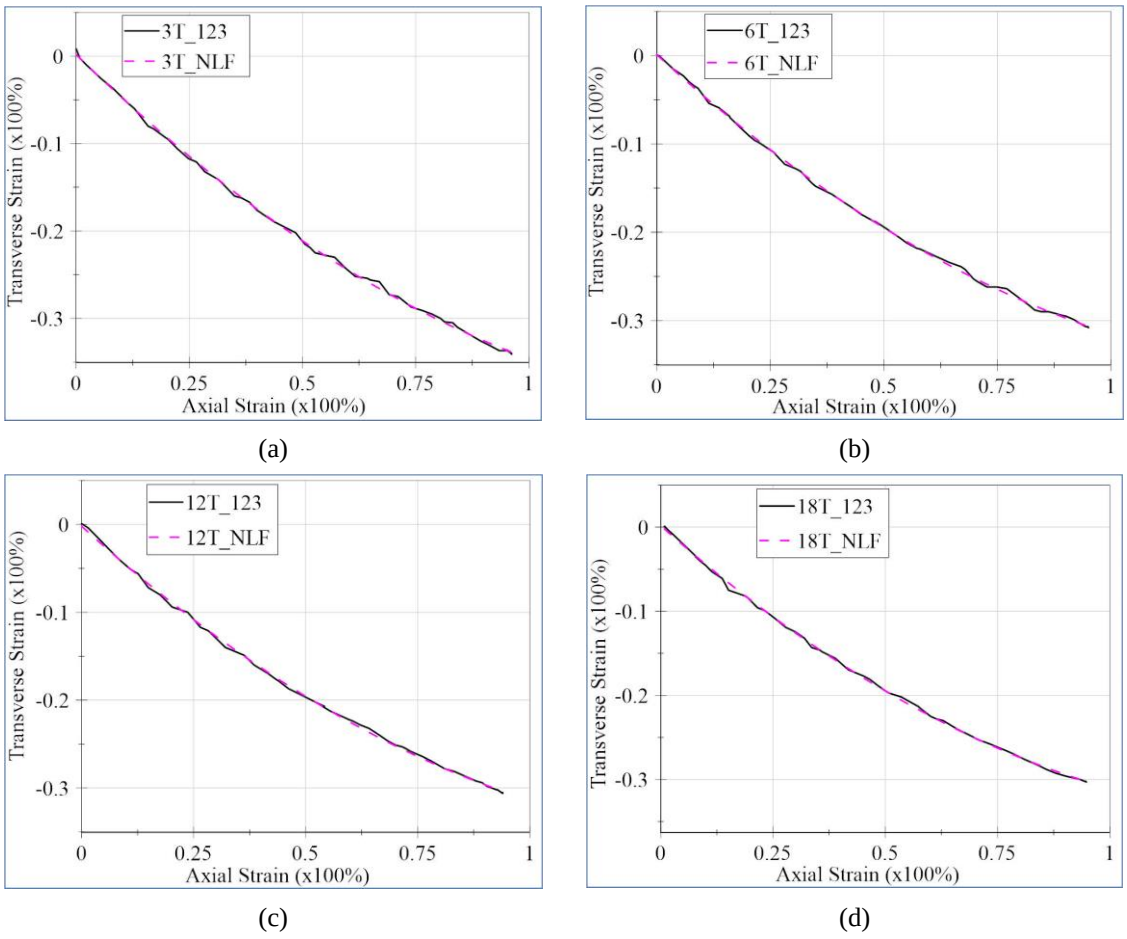

Figure 4-26: The transverse strain versus the strain for 3, 6, 12 and 18 Shore A hardnesses in (a), (b), (c) and (d) are shown here. In each diagram, the black solid line and the red dashed line curves are related to average and its nonlinear calculated function, respectively. The average curve is achieved from 3 different test specimen measurement results. The nonlinear calculated curve is a Polynomial function of order two.

The nonlinear calculated curves in Figure 4-26 were fitted very well on the average curves. The nonlinear function in equation (4-4) is used to calculate the transverse strain of ε_t for each axial strain value of ε_a. Then, it can be used to calculate the poisson's ratio for the defined strain values according to the standard (ASTM D638, 2014). In equation (4-4), ε_t and ε_a are the transverse strain and the axial strain. The a_1, a_2 and a_3 are the nonlinear fitting function indexes. The equation parameters are calculated with nonlinear curve fitting method for different hardnesses based on the axial-transverse strain test results. The test results are shown by names with "S"T_123 format in Figure 4-26. The calculated functions according to this method are second degree Polynomial functions. They are shown by names with "S"T_NLF format in Figure 4-26.

$$\varepsilon_t = a_1 + a_2\varepsilon_a + a_3{\varepsilon_a}^2 \quad (4\text{-}4)$$

Table 4-5 describes the nonlinear fitting function parameters of equation (4-4). The coefficient of determination (R^2) is 0.999 and mean squared error (MSE) is very small for the different functions, it proves that the functions are fitted very well with the test results.

Table 4-5: The calculated poisson's ratio and parameters of second degree Polynomial fitting function of axial-transverse strain experimental results. It is classified for different Shore A hardnesses. The a_1, a_2 and a_3 are the function indexes. MSE is the mean squared error.

Shore A		3	6	12	18
Poisson's ratio		0.5035	0.4673	0.4621	0.4725
Nonlinear fitting function parameters	a_1	0.0018	0.0011	-0.0019	0.0016
	a_2	-0.5042	-0.4679	-0.4627	-0.4731
	a_3	0.1562	0.1517	0.1508	0.1610
	MSE	9.1680E-06	5.1299E-06	5.7322E-06	1.2464E-05

Finally, the equation (4-4) leads to calculate the transverse strain for desired axial strain values in different hardnesses. Then, Poisson's ratio is calculated by use of equations of (4-2) and (4-4). So, a constant value as Poisson's ratio for each hardness is reported in Table 4-5 according to these equations and refer to related standard ASTM D638 (2014). The calculated Poisson's ratios for silicone rubber with different hardnesses are near to 0.5. It shows that the silicone rubber as pad material is an incompressible material.

4.4 Selection of silicone rubber pad material model

There are different material models for silicone rubber as a hyperelastic material such as Polynomial, reduced Polynomial and Ogden models. In this part, the most fitted model to experiments for each hardness of silicone rubber will be selected according to the following method.

4.4.1 Method of material model selection

A material model describes the type of strain energy function (and constitutive model) in the hyperelastic material for different hardnesses according to the test results of the material. There are different material models such as Polynomial, reduced Polynomial and Ogden models in different orders. These models are calculated according to test results of chapter 4.3 and the use of the general equation (2-30) that was divided into equations (2-34), (2-37) and (2-39) for different test methods. In the following, a method to select the most accurate material model between the possible material models is presented.

The loading part of the test cycle from different test methods are usually used to evaluate a hyperelastic material model (Simulia, 2013a). Here, the loading part of the test cycle is called an experiment.

The suitable hyperelastic material model is selected according to experiment result. In this case, a material model is selected which fits more with experiment result. R-squared factor is called the coefficient of determination. It is used to find the model which is more fitted to the experiment and it is called model selection. According to (Dispersyn et al, 2017; Shahzad et al, 2015), R-squared is calculated with use of equation (4-5). Here, equation (4-6) and (4-7) explain the summation of square errors from the model (SS_{reg}) and the sum of the square deviation around the test results average (SS_{total}). The σ_i^{test}, σ_i^{model} and $\sigma_i^{avg\_test}$ are stress values in i^{th} element of strain for test results, model results and the average of test results, respectively.

$$R-squared = 1-\frac{SS_{reg}}{SS_{total}} \tag{4-5}$$

$$SS_{reg} = \sum_{i=1}^{n}(\sigma_i^{test} - \sigma_i^{model})^2 \tag{4-6}$$

$$SS_{total} = \sum_{i=1}^{n}(\sigma_i^{test} - \sigma_i^{avg\_test})^2 \tag{4-7}$$

In following, the selection of silicone rubber material model with hardness of 3 Shore A is described in detail. In this case, Figure 4-28 and Figure 4-27 show the different possible hyperelastic material models in comparison with the uniaxial tensile and

compression test results of silicone rubber material with hardness of 3 Shore A. In this chapter, the figures for selection of silicone rubber material model with other hardnesses are not presented because of similarity in curves behaviors. These figures will be presented in Appendix A1.

Afterwards, for selection of silicone rubber material model, the accuracy of fit parameters for different models are calculated according to the equation (4-5), (4-6) and (4-7) and reported in the tables of this chapter. In these tables, the R-squared is an appropriate parameter to compare the fitting of different hyperelastic material models with experiments result.

This chapter is a part of simulation results verification because it establishes the fitted material model to experiment result to perform simulation.

In the following, different material models for each hardness of silicone rubber are presented according to the test results in chapter 4.3. The basic knowledge about different models of hyperelastic materials was described in chapter 2.3.

4.4.2 Selection of silicone rubber material model with 3 Shore A hardness

In this part, Figure 4-27 and Figure 4-28 show curves of the Polynomial (Poly), reduced Polynomial (R_Poly) and Ogden models in different order numbers (N). The dashed lines with +, x and o symbols show the Polynomial, reduced Polynomial and Ogden curves. The red, green, blue, violet, turquoise and gray colors define the order numbers of 1 till 6. These models are calculated according to experiment result (black solid curves) with the use of the general equation (2-30) that was divided into equations (2-34), (2-37) and (2-39) for different test methods. These equations were described in chapter 2.3.1.

Figure 4-27 and Figure 4-28 show the diversity of 14 different hyperelastic material models with tensile test and compression test data. In these figures, the black solid line is the loading part of the test cycle and it is called Experiment in the figure legend. The Experiment curve in Figure 4-27 is reached from the loading part of the last cycle in the uniaxial tensile test with hardness of 3 Shore A which was shown in Figure 4-20 (a). The Poly_N2 (green dashed line with + symbol) is the nearest model to Experiment curve in Figure 4-27.

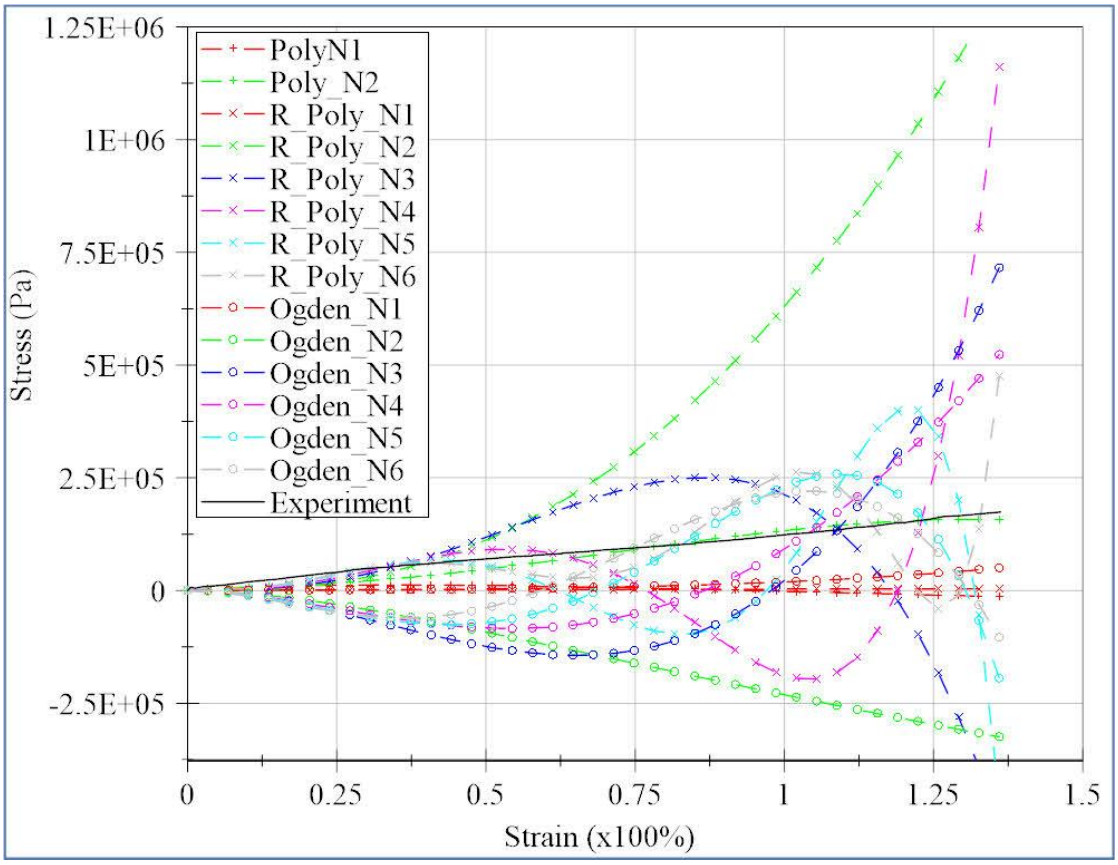

Figure 4-27: The different possible hyperelastic material models in comparison with the tensile test results of 3 Shore A. The stress-strain behavior of different models and related curves are described here. The black solid line was achieved from uniaxial tensile test results for 3 Shore A. The dashed lines describe different model results.

The Experiment curve in Figure 4-28 is related to the loading part of the uniaxial compression test with hardness of 3 Shore A which was shown in the Figure 4-22 (a). Other curves display the hyperelastic material models which are achieved according to the equations in chapter 2.3.2. Also here, the Poly_N2 (green dashed line with + symbol) is the nearest model to the compression test results with hardness of 3 Shore A, in Figure 4-28.

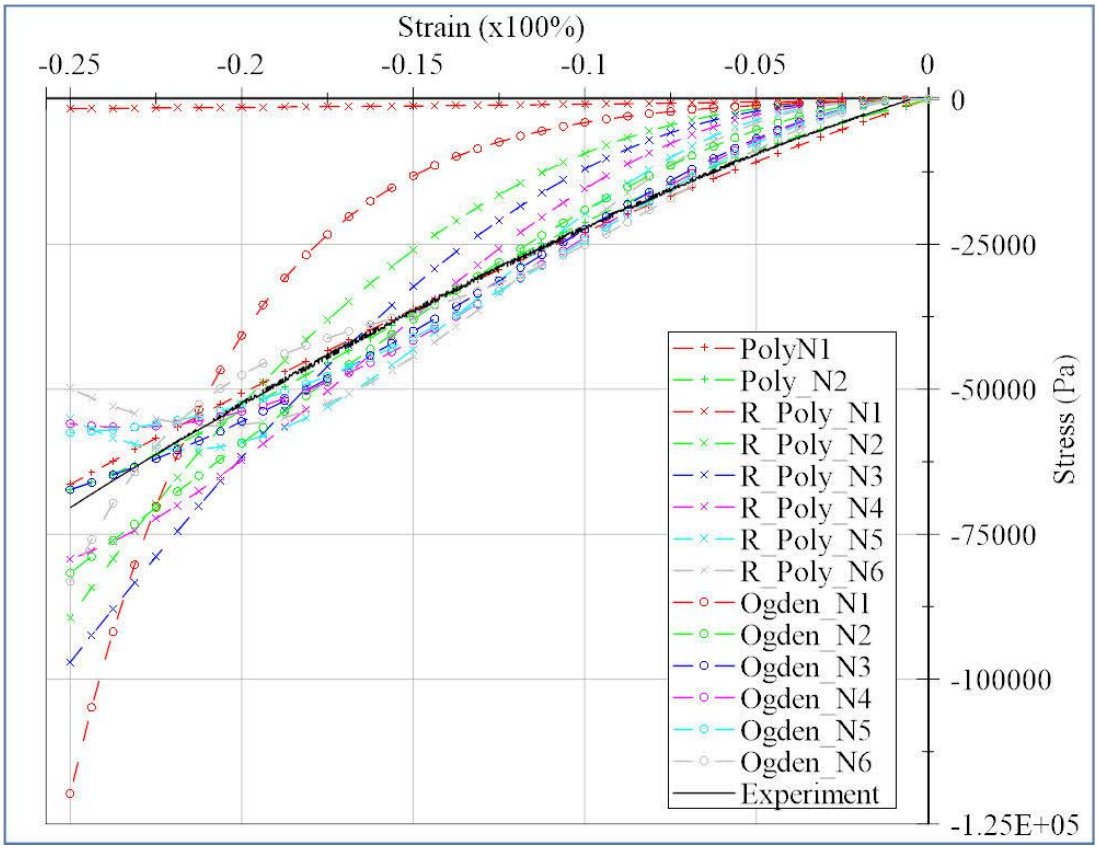

Figure 4-28: The possible hyperelastic material models and the compression test results of 3 Shore A. The stress-strain behavior of different models and related curves are described here. The black solid line was achieved from compression test results for 3 Shore A. The dashed lines describe different model results.

Table 4-6 clarifies the accuracy of the fits for different hyperelastic material models compared to test results. The R-squared is a suitable quantitative parameter to find the model which is more fitted to test results. The summation of square errors (SS_{reg}) and root mean square errors (RMSE) are also described in this table. For the Polynomial model of degree 2 (Polynomial order 2), both errors are the smallest and the coefficient of determination R-squared is the nearest value to 1 in comparison with other models. The Polynomial order 2 model is presented by equation (4-8). It is achieved when N is equal to 2 in equation (2-41).

$$W = \sum_{i+j=1}^{2} C_{ij}(I_1 - 3)^i (I_2 - 3)^j + \sum_{i=1}^{2} \frac{1}{D_i}(J-1)^{2i} \qquad (4\text{-}8)$$

Table 4-6: The accuracy of fit parameters for different models in comparison with tension and comparission test results of 3 shore A silicone rubber. The SS_{reg}, R-squared and RMSE are a summation of square errors from the model, the coefficient of determination and root mean square error, respectively.

	Tension			Compression		
	SS_{reg}	R-squared	RMSE	SS_{reg}	R-squared	RMSE
Poly_N1	5.420E+11	-3.100E+00	9.931E+04	2.050E+10	9.939E-01	1.602E+03
Poly_N2	1.230E+10	9.071E-01	1.495E+04	6.600E+09	9.980E-01	9.082E+02
R_Poly_N1	5.160E+11	-2.899E+00	9.685E+04	1.070E+13	-2.207E+00	3.662E+04
R_Poly_N2	1.090E+13	-8.125E+01	4.448E+05	7.230E+11	7.838E-01	9.507E+03
R_Poly_N3	1.370E+12	-9.374E+00	1.580E+05	8.710E+11	7.397E-01	1.043E+04
R_Poly_N4	2.410E+12	-1.718E+01	2.091E+05	3.890E+11	8.837E-01	6.973E+03
R_Poly_N5	1.220E+12	-8.256E+00	1.492E+05	2.660E+11	9.206E-01	5.762E+03
R_Poly_N6	3.940E+11	-1.978E+00	8.465E+04	3.370E+11	8.993E-01	6.488E+03
Ogden_N1	3.790E+11	-1.868E+00	8.306E+04	2.510E+12	2.503E-01	1.770E+04
Ogden_N2	4.180E+12	-3.057E+01	2.756E+05	2.140E+11	9.361E-01	5.168E+03
Ogden_N3	1.780E+12	-1.249E+01	1.801E+05	4.810E+10	9.856E-01	2.453E+03
Ogden_N4	8.820E+11	-5.667E+00	1.266E+05	1.470E+11	9.562E-01	4.279E+03
Ogden_N5	5.940E+11	-3.489E+00	1.039E+05	1.260E+11	9.625E-01	3.961E+03
Ogden_N6	3.880E+11	-1.933E+00	8.400E+04	8.020E+10	9.760E-01	3.166E+03

Table 4-7: The Polynomial order 2 (Poly_N2) model coefficients according to experiment results of silicone rubber 3 Shore A. The Polynomial order 2 model is described by equation (4-8).

D1	C10	C01	C11
0.0000	-1.352E+4	2.631E+4	1.165E+5
D2	C20	C02	
0.0000	-3.762E+4	-5.861E+4	

Figure 4-27, Figure 4-28 and Table 4-6 show the selection of different models compared to the test results for silicone rubber with hardness of 3 Shore A. So, the Polynomial model of degree 2 with coefficients described in Table 4-7 is the model which fits best to experiment results and it can be used in simulation of silicone rubber pad behavior with hardness of 3 Shore A.

4.4.3 Selection of silicone rubber material model with 6 Shore A hardness

Table 4-8 shows quantitatively the similarity of different hyperelastic material models with test results. The R-squared is an appropriate parameter to compare them and find the model which is more fitted to test results. For the Polynomial model of degree 2, the SS_{reg} and the RMSE are the smallest and the R-squared is the nearest value to 1 in comparison with other models. So, this model is selected.

Table 4-8: The accuracy of fit parameters for different models in comparison with tension and compression test results of 6 shore A silicone rubber. The SS_{reg}, R-squared and RMSE are a summation of square errors from the model, the coefficient of determination and root mean square error, respectively.

	Tension			Compression		
	SS_{reg}	R-squared	RMSE	SS_{reg}	R-squared	RMSE
Poly_N1	8.890E+11	-1.717E+00	1.179E+05	4.300E+10	9.917E-01	2.320E+03
Poly_N2	1.920E+10	9.413E-01	1.732E+04	9.530E+09	9.982E-01	1.092E+03
R_Poly_N1	6.900E+11	-1.108E+00	1.038E+05	1.020E+13	-9.640E-01	3.565E+04
R_Poly_N2	1.440E+13	-4.286E+01	4.736E+05	7.220E+11	8.605E-01	9.503E+03
R_Poly_N3	1.610E+12	-3.931E+00	1.588E+05	9.010E+11	8.258E-01	1.062E+04
R_Poly_N4	2.510E+12	-6.680E+00	1.982E+05	4.070E+11	9.213E-01	7.138E+03
R_Poly_N5	1.100E+12	-2.362E+00	1.311E+05	3.380E+11	9.347E-01	6.501E+03
R_Poly_N6	4.590E+11	-4.019E-01	8.468E+04	3.960E+11	9.235E-01	7.038E+03
Ogden_N1	6.910E+11	-1.110E+00	1.039E+05	1.360E+12	7.367E-01	1.306E+04
Ogden_N2	5.680E+12	-1.636E+01	2.980E+05	2.580E+11	9.500E-01	5.686E+03
Ogden_N3	2.390E+12	-6.301E+00	1.932E+05	6.840E+10	9.868E-01	2.927E+03
Ogden_N4	1.120E+12	-2.429E+00	1.324E+05	2.040E+11	9.605E-01	5.057E+03
Ogden_N5	7.880E+11	-1.407E+00	1.110E+05	1.680E+11	9.675E-01	4.590E+03
Ogden_N6	5.490E+11	-6.755E-01	9.258E+04	9.860E+10	9.809E-01	3.513E+03

Table 4-9: The Polynomial model order 2 (Poly_N2) coefficients according to test results of silicone rubber 6 Shore A. The Polynomial order 2 model is described by equation (4-8).

D1	C10	C01	C11
3.270E-06	-8.234E+03	2.696E+04	1.252E+05
D2	C20	C02	
0.000E+00	-3.976E+04	-6.210E+04	

It can be concluded from Table 4-8 that the Polynomial model of degree 2 with described coefficients in Table 4-9 is the model which is more fitting to 6 Shore A silicone rubber test results. So, these results validate the Polynomial of degree 2 material model to be used in the simulation process of the silicone rubber pads with a hardness of 6 Shore A.

The figures of hyperelastic material models in comparison with the tensile and compression test results are positioned in Appendix A1 for more studies.

4.4.4 Selection of silicone rubber material model with 12 Shore A hardness

Table 4-10 shows the R-squared, SS_{reg} and RMSE of different hyperelastic material models compare to the test results. By considering the minimum value for the errors and nearest value of R-squared to 1, the appropriate model is selected. So, the Polynomial model of degree 2 for 12 Shore A silicone rubber material model is selected, too.

Table 4-10: The accuracy of fit parameters for different models in comparison with tension and compression test results of 12 shore A silicone rubber. The SS_{reg}, R-squared and RMSE are a summation of square errors from the model, the coefficient of determination and root mean square error, respectively.

	Tension			Compression		
	SS_{reg}	R-squared	RMSE	SS_{reg}	R-squared	RMSE
Poly_N1	1.970E+12	-2.605E+00	1.343E+05	1.640E+11	9.889E-01	4.496E+03
Poly_N2	6.970E+10	8.723E-01	2.529E+04	8.730E+10	9.941E-01	3.279E+03
R_Poly_N1	2.380E+12	-3.364E+00	1.478E+05	5.150E+13	-2.489E+00	7.963E+04
R_Poly_N2	4.850E+13	-8.789E+01	6.671E+05	6.280E+12	5.742E-01	2.782E+04
R_Poly_N3	8.710E+12	-1.497E+01	2.827E+05	3.380E+12	7.708E-01	2.041E+04
R_Poly_N4	4.190E+12	-6.683E+00	1.961E+05	2.380E+12	8.391E-01	1.710E+04
R_Poly_N5	3.320E+12	-5.080E+00	1.745E+05	1.140E+12	9.226E-01	1.186E+04
R_Poly_N6	1.020E+12	-8.728E-01	9.682E+04	1.650E+12	8.880E-01	1.427E+04
Ogden_N1	1.780E+12	-2.254E+00	1.276E+05	1.970E+13	-3.340E-01	4.924E+04
Ogden_N2	9.930E+12	-1.719E+01	3.018E+05	2.190E+12	8.515E-01	1.643E+04
Ogden_N3	5.430E+12	-8.945E+00	2.231E+05	7.200E+11	9.512E-01	9.415E+03
Ogden_N4	2.220E+12	-3.075E+00	1.428E+05	1.030E+12	9.304E-01	1.125E+04
Ogden_N5	1.770E+12	-2.240E+00	1.274E+05	7.910E+11	9.464E-01	9.866E+03
Ogden_N6	1.110E+12	-1.042E+00	1.011E+05	5.140E+11	9.652E-01	7.952E+03

Table 4-11: The Polynomial model order 2 (Poly_N2) coefficients according to test results of silicone rubber 12 Shore A. The Polynomial order 2 model is described by equation (4-8).

D1	C10	C01	C11
3.799E-06	-5.866E+04	8.030E+04	2.394E+05
D2	C20	C02	
0.000E+00	-7.628E+04	-1.257E+05	

Between different models the Polynomial model of degree 2 with described coefficients in Table 4-11 is selected to use in the simulation process as the material model for silicone rubber having a hardness of 12 Shore A.

The figures of hyperelastic material models in comparison with the tensile and compression test results are positioned in Appendix A1 for more studies.

4.4.5 Selection of silicone rubber material model with 18 Shore A hardness

To simulate the silicone rubber pad behavior, the different hyperelastic material models can be applied.

The accuracy of different models versus the experiment results is described in Table 4-12 numerically. It shows the R-squared as an appropriate parameter to compare different models and find the model which is more fitted to test results. The model which has the nearest R-squared value to 1 with the smallest values of SS_{reg} and RMSE, is chosen. So, this situation can be fulfilled with the Polynomial model of degree 2.

The coefficients of Polynomial model of degree 2 of silicone rubber 18 Shore A are clarified in Table 4-13.

Table 4-12: The accuracy of fit parameters for different models in comparison with tension and compression test results of 18 shore A silicone rubber. The SS_{reg}, R-squared and RMSE are a summation of square errors from the model, the coefficient of determination and root mean square error, respectively.

	Tension			Compression		
	SS_{reg}	R-squared	RMSE	SS_{reg}	R-squared	RMSE
Poly_N1	5.790E+12	-2.813E+00	3.547E+05	1.840E+11	9.937E-01	4.800E+03
Poly_N2	1.100E+11	9.277E-01	4.882E+04	6.630E+10	9.977E-01	2.881E+03
R_Poly_N1	4.850E+12	-2.199E+00	3.248E+05	8.080E+13	-1.769E+00	1.006E+05
R_Poly_N2	1.060E+14	-6.854E+01	1.510E+06	5.550E+12	8.100E-01	2.635E+04
R_Poly_N3	1.520E+13	-9.020E+00	5.749E+05	6.760E+12	7.685E-01	2.909E+04
R_Poly_N4	2.120E+13	-1.299E+01	6.794E+05	3.190E+12	8.906E-01	2.000E+04
R_Poly_N5	1.170E+13	-6.740E+00	5.053E+05	2.220E+12	9.240E-01	1.667E+04
R_Poly_N6	3.680E+12	-1.424E+00	2.828E+05	2.830E+12	9.031E-01	1.881E+04
Ogden_N1	3.710E+12	-1.447E+00	2.841E+05	1.390E+13	5.246E-01	4.168E+04
Ogden_N2	4.160E+13	-2.642E+01	9.511E+05	1.580E+12	9.457E-01	1.408E+04
Ogden_N3	1.720E+13	-1.035E+01	6.118E+05	4.900E+11	9.832E-01	7.835E+03
Ogden_N4	8.540E+12	-4.626E+00	4.308E+05	1.300E+12	9.555E-01	1.276E+04
Ogden_N5	5.080E+12	-2.347E+00	3.323E+05	1.180E+12	9.597E-01	1.213E+04
Ogden_N6	3.750E+12	-1.474E+00	2.857E+05	6.180E+11	9.788E-01	8.797E+03

Table 4-13: The Polynomial model in order 2 (Poly_N2) coefficients according to test results of silicone rubber 18 Shore A. The Polynomial order 2 model is described by equation (4-8).

D1	C10	C01	C11
1.583E-06	-5.420E+04	9.289E+04	2.346E+05
D2	C20	C02	
0.000E+00	-6.332E+04	-1.237E+05	

The figures of hyperelastic material models in comparison with the tensile and compression test results are positioned in Appendix A1 for more studies.

It is concluded from the described hyperelastic material models with 3, 6, 12 and 18 Shore A hardnesses that the Polynomial model of degree 2 (equation (4-8)) is a suitable model to simulate the material behavior of the silicone rubber pads. Briefly, in this part the appropriate material model of silicone rubber and the related coefficients of this model for different hardnesses were clarified. This model was validated in comparison with material test results.

The automation level of indirect gravure printing process can be improved by performing a simulation of the printing process. The material model is an input for the simulation process. So, selection of more accurate material model verifies the material specifications which are used in the simulation process. In addition to the material model, the pad geometry is an important issue to execute the simulation process. So, a method to design the pad geometry is described in the next chapter.

5 Method of designing the pad geometry

According to experts' knowledge, scientific researches and knowledge of the author, until now, there is no mathematical and organized method to design a pad. The pad designing process is empirically according to the experiments of experts. Further, the production process is expensive because of producing the positive forms with metal (Lück, 2017a). So, for the first time, a method for designing a pad is presented here. Further, a novelty in the production procedure of pad molds with benefit of reduction in the molds production costs are introduced in this chapter.

The awareness of effective parameters in designing a pad leads to consider possible types of pads in each printing case. This awareness of effect of different parameters on designing a pad is achieved by mathematical equations. Then, it is possible to select the optimized parameters of a pad according to each printing case. Further, their molds can be produced in a cost efficient method. Therefore, the printing process can be performed with optimized geometry of pad based on each printing condition. It is mentioned that the process optimization is related to level 3 of automation levels.

The pad is a main part in the indirect gravure printing process. It is important to print with a pad which its size and geometry are matched with the substrate and printing motif. For example, printing on a convex substrate needs a pad with less sharpness in comparison with printing on a concave surface. As a further example, a pad size relates to printing motif size. For instance, in practice, the pad size is different for a printing motif with a diameter of 10 mm in comparison with a diameter of 12 mm.

Therefore, in this case, first, the mathematical equations of the pad geometry should be discovered. Second, a calculator is programmed to calculate the geometrical parameters of the pad easily. Third, the pad geometry is drawn according to calculated parameters. Finally, the pad mold is prepared and the desired pad can be produced.

It was described in 2.2.2 that the rectangular geometry of pads is one of the most used geometries. So, in this dissertation the pad with rectangular geometry will be considered. The goal of this chapter is the introduction of a mathematical method to design rectangular pads.

5.1 Mathematical equations of the rectangular pad geometry

The pad designing possibility is needed to design unique pads according to printing conditions. Therefore, mathematical relationships between different parameters of pad geometry should be investigated to design a pad. Further, the independent variables in mathematical equations should be achieved. They are considered as effective parameters on pad design. The other parameters can be calculated with the help of mathematical equations and effective parameters. In following, mathematical equations of the pad with rectangular geometry is presented.

In this work, the rectangular pad geometry is divided into three different segments. They are base, arc and surface (bottom, middle and top) segments that are shown in Figure 5-1.

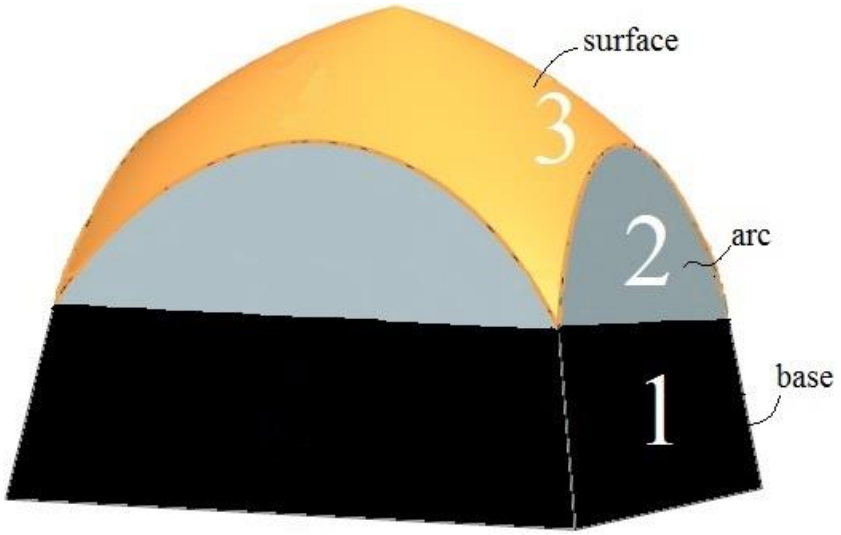

Figure 5-1: The three pad geometry segments of a rectangular pad: base (1), arc (2) and surface (3). They are defined to calculate the mathematical equations of each segment, according to their solid geometry.

Base segment

In Figure 5-2, two planes $A_1A_2A_3A_4$ and $B_1B_2B_3B_4$ are parallel, so the distance between them is the constant value h. Therefore, h is the height value of B_1 till B_4 points. O is the center point of the $A_1A_2A_3A_4$ plane and it is located on the center of the used coordinate system. O′ is the center point of the $B_1B_2B_3B_4$ plane. O″ is the point on the tip of the

pad in segment 3 and it is the highest point of the pad. O, O′ and O″ are located on the Z-axis of the coordinate system.

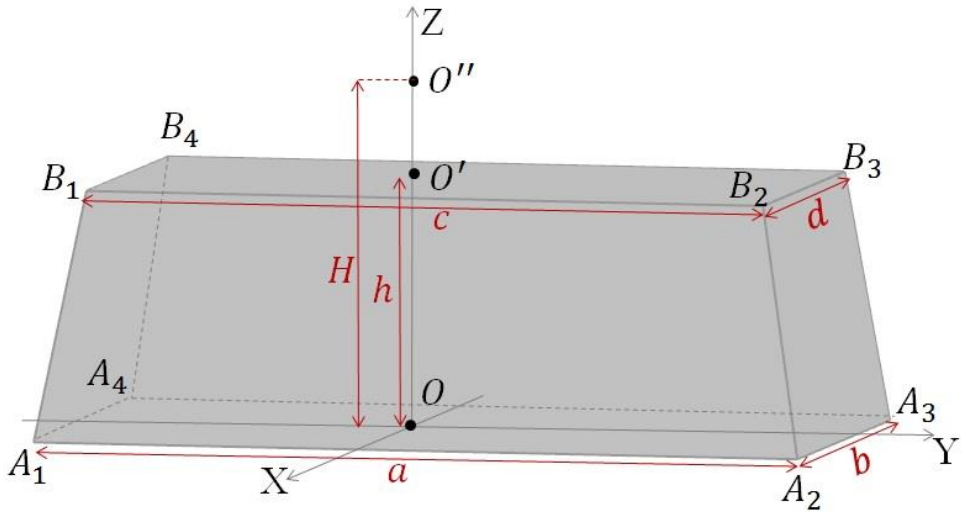

Figure 5-2: The pad base segment. A_1, A_2, A_3, A_4 and O are located on the bottom plane. B_1, B_2, B_3, B_4 and O′ are positioned on the upper plane of the base segment. O″ is the highest point of the pad. The XYZ are the axes of the coordinate system. a, b and H are length, width and height of the pad. c, d and h are length, width and height of the print area.

The coordinates of A_1 till A_4 and B_1 till B_4 points are the main parameters to calculate the base segment solid geometry of the pad. So, the method to calculate them is described here.

Equations (5-1) till (5-5) describe the problem assumptions according to the parameters of Figure 5-2 and the rectangular pad features.

$$\left|\overline{A_1A_2}\right| = \left|\overline{A_4A_3}\right| = a \tag{5-1}$$

$$\left|\overline{A_2A_3}\right| = \left|\overline{A_1A_4}\right| = b \tag{5-2}$$

$$\left|\overline{B_1B_2}\right| = \left|\overline{B_4B_3}\right| = c \tag{5-3}$$

$$\left|\overline{B_2B_3}\right| = \left|\overline{B_1B_4}\right| = d \tag{5-4}$$

$$\left|\overline{OO''}\right| = H \tag{5-5}$$

In equations (5-1) till (5-5), a, b, c, d and H parameters are called pad length, pad width, print area length, print area width and pad height, respectively. They are usually introduced as the technical parameters of pads. So, equations (5-6) till (5-9) describe the coordinates of A_1 till A_4 in the base segment. Equation (5-10) is related to coordinates of O″ according to equation (5-5).

$$A_1\left(\frac{b}{2},\frac{-a}{2},0\right) \tag{5-6}$$

$$A_2\left(\frac{b}{2},\frac{a}{2},0\right) \tag{5-7}$$

$$A_3\left(\frac{-b}{2},\frac{a}{2},0\right) \tag{5-8}$$

$$A_4\left(\frac{-b}{2},\frac{-a}{2},0\right) \tag{5-9}$$

$$O''\left(0,0,H\right) \tag{5-10}$$

Figure 5-3 displays the position of base segment angles which are described in equations (5-11) till (5-14). The relationship between the angles of Θ_2, Θ'_2 and Θ''_2 is described in equation (5-13) according to the rules of solid geometry. In Figure 5-3 (b), B'_2 is the intersection point of $A_1A_2A_3A_4$ plane and the perpendicular line to this plane through B_2 point. A_{23} is the intersection point of A_2A_3 line segment and its perpendicular line that crosses B'_2. The distance between the two points B_2 and B'_2 is called h.

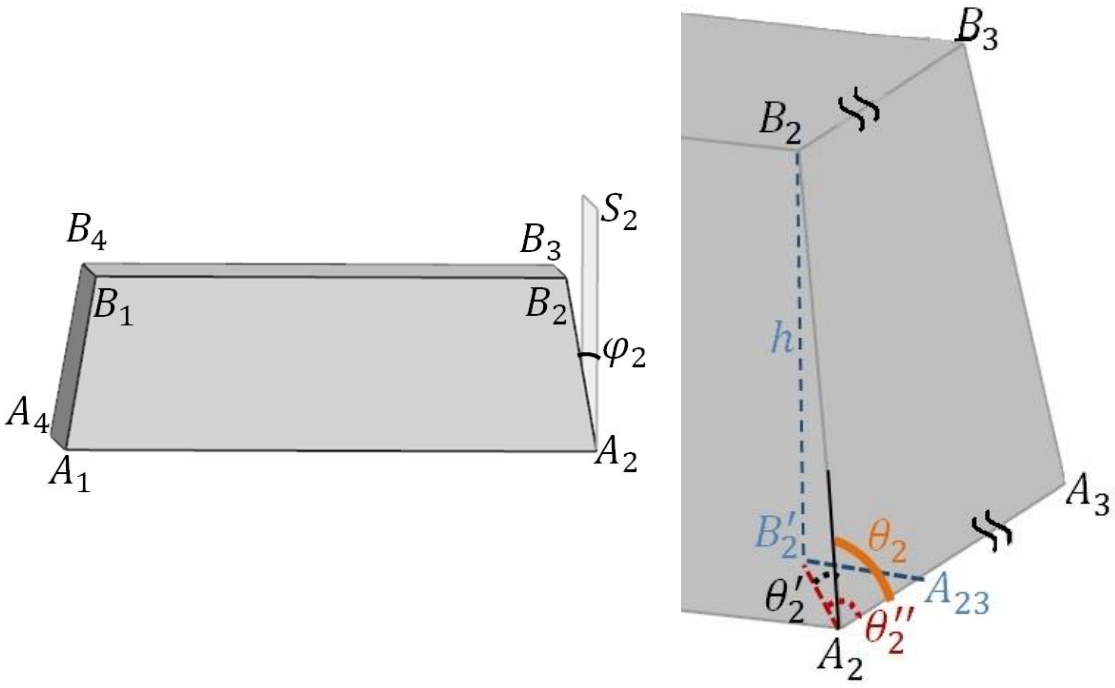

(a) (b)

Figure 5-3: The pad base angles. (a): φ_2 is the angle between the plane of pad side and vertical plane (S_2). (b): Θ_2 is the angle of $B_2A_2A_{23}$. Θ'_2 is the angle of $B_2A_2B'_2$ and Θ''_2 is the angle of $B_2'A_2A_3$.

$$\angle B_2 A_2 S_2 = \varphi_2 \tag{5-11}$$

$$\angle B_2 A_2 A_3 = \theta_2 \tag{5-12}$$

$$\angle B_2 A_2 B_2' = \theta_2' = \cos^{-1}\left(\frac{cos\theta_2}{cos\theta_2''}\right) \tag{5-13}$$

$$\angle B_2' A_2 A_{23} = \theta_2'' \tag{5-14}$$

φ_2 is the angle between the plane of pad side and vertical plane (S_2) according to Figure 5-3 (a). This value describes the deviation of the side plane of pad in comparison with the vertical plane that it is perpendicular to X-Y plane of coordinate system.

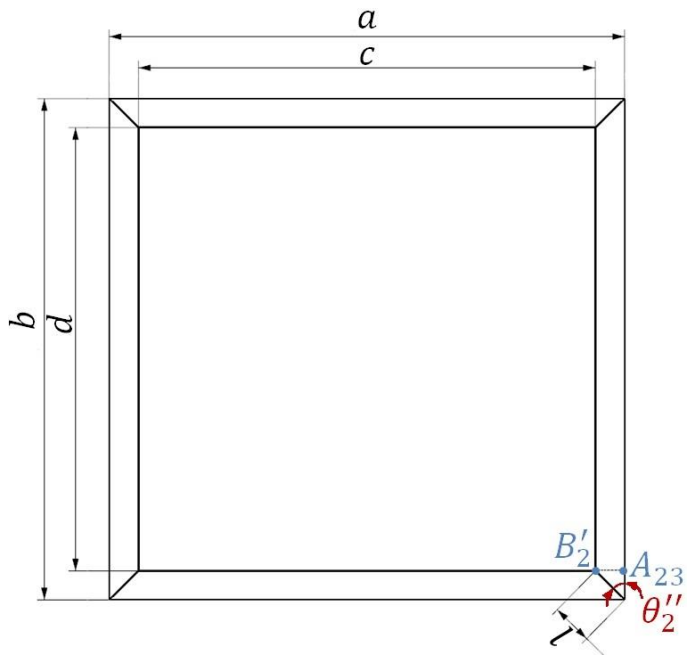

Figure 5-4: Top view of the base segment. The position of Θ″$_2$ and its relationship with other parameters are shown here. a, b, c and d are the dimensions of the pad and print area.

Figure 5-4 is related to the top view of the base segment to get equations (5-15) and (5-16) according to the technical parameters of pad (a, b, c and d). $A_{23}B'_2$ and A_2A_{23} are perpendicular line segments. So, l and Θ″$_2$ values are calculated by equations (5-15) and (5-16).

$$\left|\overline{A_2B_2'}\right| = l = \sqrt{\left(\frac{a-c}{2}\right)^2 + \left(\frac{b-d}{2}\right)^2} \tag{5-15}$$

$$\theta_2'' = \tan^{-1}\left(\frac{a-c}{b-d}\right) \tag{5-16}$$

The parameter of h is the height or value in Z-direction of the coordinates of B_1, B_2, B_3 and B_4. It is explained in equation (5-17) and its parameters are achieved with equations (5-13) and (5-15). Finally, the coordinates of B_1 till B_4 and O′ are described in equations (5-18) till (5-22).

$$\left|\overline{OO'}\right| = h = l.\tan\theta_2' \tag{5-17}$$

$$B_1\left(\frac{d}{2},\frac{-c}{2},h\right) \tag{5-18}$$

$$B_2\left(\frac{d}{2},\frac{c}{2},h\right) \tag{5-19}$$

$$B_3\left(\frac{-d}{2},\frac{c}{2},h\right) \tag{5-20}$$

$$B_4\left(\frac{-d}{2},\frac{-c}{2},h\right) \tag{5-21}$$

$$O'\left(0,0,h\right) \tag{5-22}$$

So, the coordinates of A_1, A_2, A_3, A_4, B_1, B_2, B_3 and B_4 as the main coordinates of base segment were achieved.

Arc segment

The $B_1B_2B_3B_4$ plane described above is an intersection of the base and arc segments. The coordinates of B_2 and B_3 from the arc segment was achieved in base segment. So, the following equations describe the procedure to calculate the coordinate of the arc segment highest point shown with G_2 parameter.

Equation (5-23) describes the angle φ_2 according to Figure 5-3 (a) and equation (5-6). So, equation (5-24) is achieved to calculate the value of φ_2. In this equation l, Θ''_2 and h are achieved from equations (5-15), (5-16) and (5-17).

$$\varphi_2 = \angle B_2 A_2 S_2 = \angle A_{23} B_2 B_2' \tag{5-23}$$

$$\varphi_2 = \tan^{-1}((l.\sin\theta_2'') / h) \tag{5-24}$$

Equation (5-25) describes the geometrical position of h_2 according to Figure 5-5 (a). So, equation (5-26) introduces the coordinate of G_2, according to the calculated φ_2 in equation (5-24).

$$\left|\overline{i_2 G_2}\right| = h_2 \tag{5-25}$$

$$G_2\left(0, \frac{a}{2} - h_2 sin\varphi_2, h_2 cos\varphi_2\right) \tag{5-26}$$

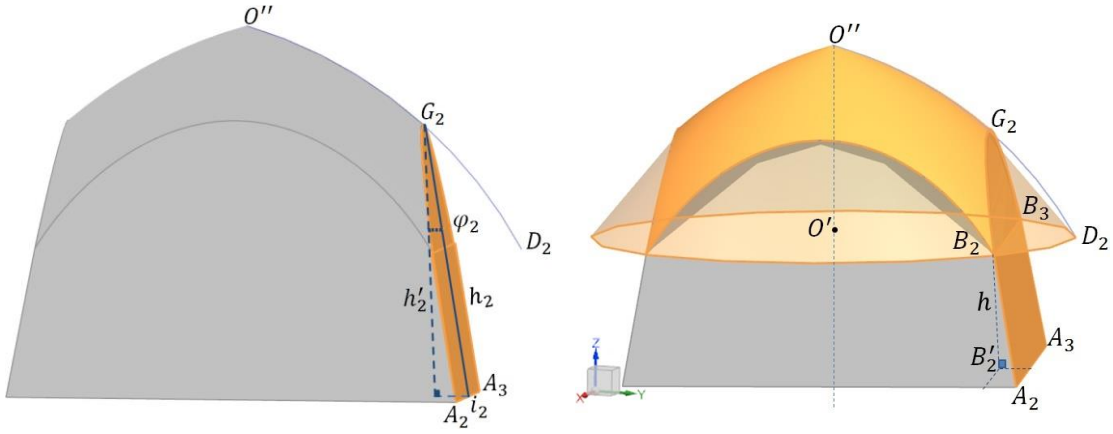

(a) (b)

Figure 5-5: The essential points of arc (a) and surface segments (b) of the pad. The location of G_2, D_2 and O″ are clarified. Their coordinates are important to get the surface of the pad. The related points and parameters (such as φ_2 and h_2 in (a) segment) to calculate their coordinates are shown here.

The coordinates of B_2, B_3 and G_2 are related to the arc segments. The coordinates of B_2 and B_3 were achieved in base segment. The coordinate of the arc segment highest point shown with G_2 parameter was calculated in this part.

Surface segment

G_2 is an intersection point of the arc and surface segments. Its coordinate was calculated in arc segment. Further, the coordinate of O″ from pad surface was explained in equation (5-10). So, the coordinate of D_2 is calculated here to get the coordinates of the main points of the surface segment.

D_2 is located on a circle perimeter in the center of O′ and radius of O′B_2. Further, D_2 is on the same plane with the positions of B_1 till B_4 and it has a value of h in Z-direction. The coordinate of D_2 in X-direction is zero because it is located on Y-plane. So, Δ_2 is the coordinate of D_2 in Y-direction. It is equal to the radius of the circle described in

equation (5-28). So, equation (5-27) describes D_2 coordinate as a function of Δ_2 and h parameters.

$$D_2\left(0,\Delta_2,h\right) \tag{5-27}$$

$$\Delta_2 = \sqrt{c^2 + d^2}\ /\ 2 \tag{5-28}$$

The pad structure is symmetric. An arc of the pad surface is created through three points of O″, G_2 and D_2. So, the whole surface of the pad can be achieved with these three points. Therefore, three coordinates of O″, G_2 and D_2 from equations of (5-10), (5-26) and (5-27), are required to get the solid geometry of the pad surface.

The three regions bounded by pad segments (the base, arc and surface of the pad) lead to the possibility of designing the pad geometry. A calculator for rectangular pads was designed according to the above equations. It was programmed in LabVIEW (Version 14). This program contains two parts: the user interface and the program structure. The user interface is described here and the program structure is shown in Appendix A2.

The user interface consists of seven input and output parameters. The output parameters are the coordinates of the pad base (A_1 till A_4 and B_1 till B_4), the top point of the arc segment (G_2) and the useful coordinates to construct the pad surface (O″, G_2 and D2). φ_2 is the angle between two planes of $A_2A_3B_2B_3$ of the pad and the plane perpendicular to Y-axis.

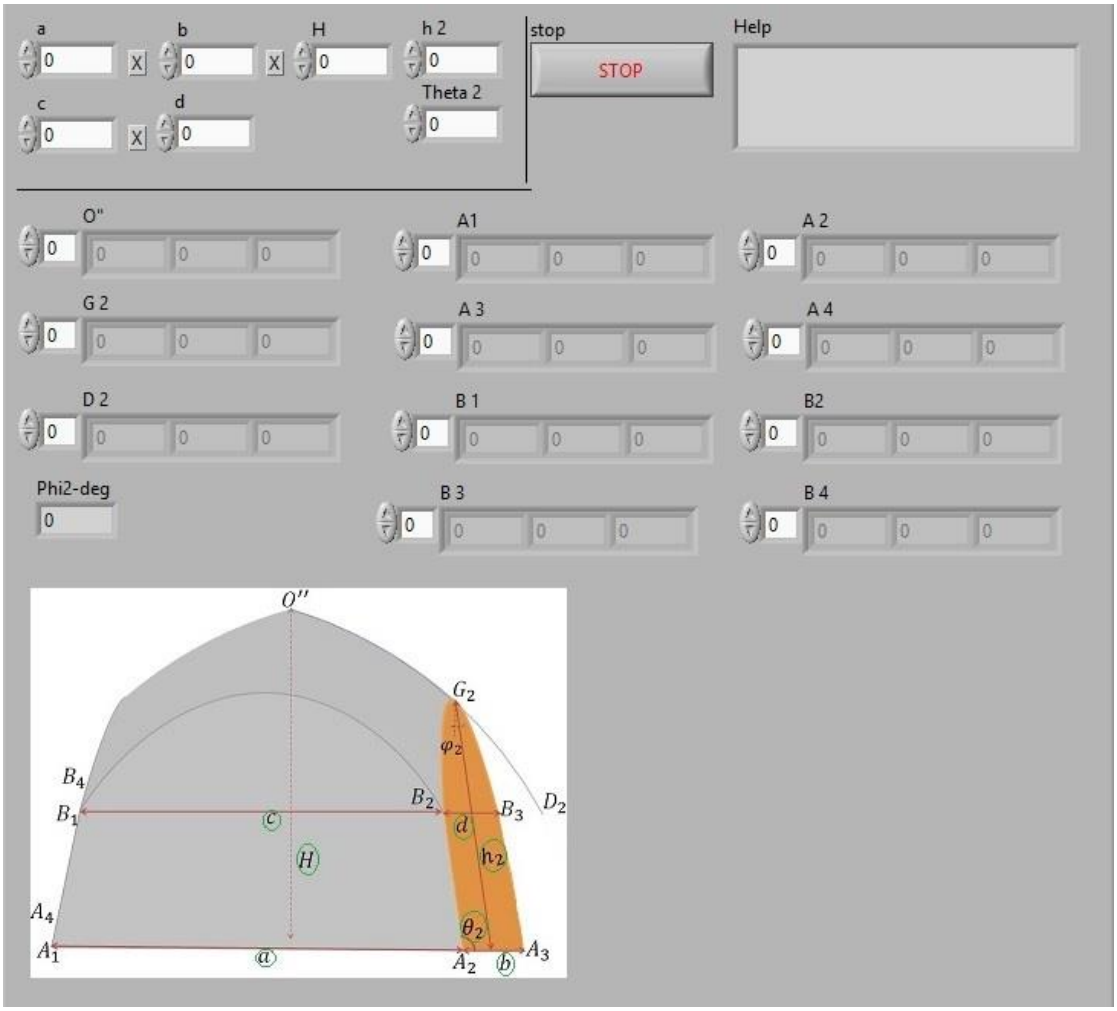

Figure 5-6: The calculator for rectangular pads. a, b, H, h_2, c, d and Θ_2 (Theta 2) are input parameters. The picture on the right side of the user interface shows graphically the concept of parameters. Other values are the outputs of the calculator to design a pad.

The calculator calculates the coordinates of points needed to draw a pad geometry. Then, a user by use of these coordinates and considering the symmetric geometry of pad can draw a pad geometry in CAD (Computer Aided Design) software such as NX. In this case, the calculator output parameters of Figure 5-6 are applied. The user applies eight parameters A_1 till A_4 and B_1 till B_4 to define the pad base structure. Then, G_2, φ_2, B_2 and B_3 parameters are considered to get the arc segment's geometry. Thereafter, three parameters O″, G_2 and D_2 are used to draw the pad surface.

5.2 New method to design the desired pads

A method to design the desired pads are presented here. In this method, the designing process of pad is divided into four steps. The first step is the calculation of the desired pad parameters. Second, the pad is constructed by using CAD software NX 10.0 according to the calculated parameters. Third step is the production of positive pad forms with a stereolithografic 3D printer (Formlabs Form 2, PreForm software for pre-processing). Then, negative forms (molds) are produced with the help of the positive forms. Finally, the silicone rubber is added to the molds and the manufacturing process is completed.

In the following, a practical example of using this method to design the desired pads is explained. This example is prepared according to a case study which will be performed in chapter 6. In this case study, the pad sharpness effects on displacement of pad surface points will be evaluated by simulation of the printing process. So, four pads with different sharpnesses (heights) are designed according to this designing method.

Therefore, in this example, the pad height is changed and other designing parameters are considered to be constant to evaluate the pad sharpness in the printing process. The height of the pad (H) is increased from pad 1 (44.5 mm) till pad 4 (68.1 mm) shown in Figure 5-7. The pad length, pad width, pad angle, print area length, print area width and arc height are 73.7 mm, 71.6 mm, 80.4 degree, 65.2 mm, 63.3 mm and 45.2 mm respectively which are constant for these pads. Then, the pad designing parameters are calculated with programed pad calculator according to the discovered mathematical equations of the pad. Afterwards, they are drawn with NX 10.0 software. Figure 5-7 shows the dimensions of pads which are called pad 1, pad 2, pad 3 and pad 4.

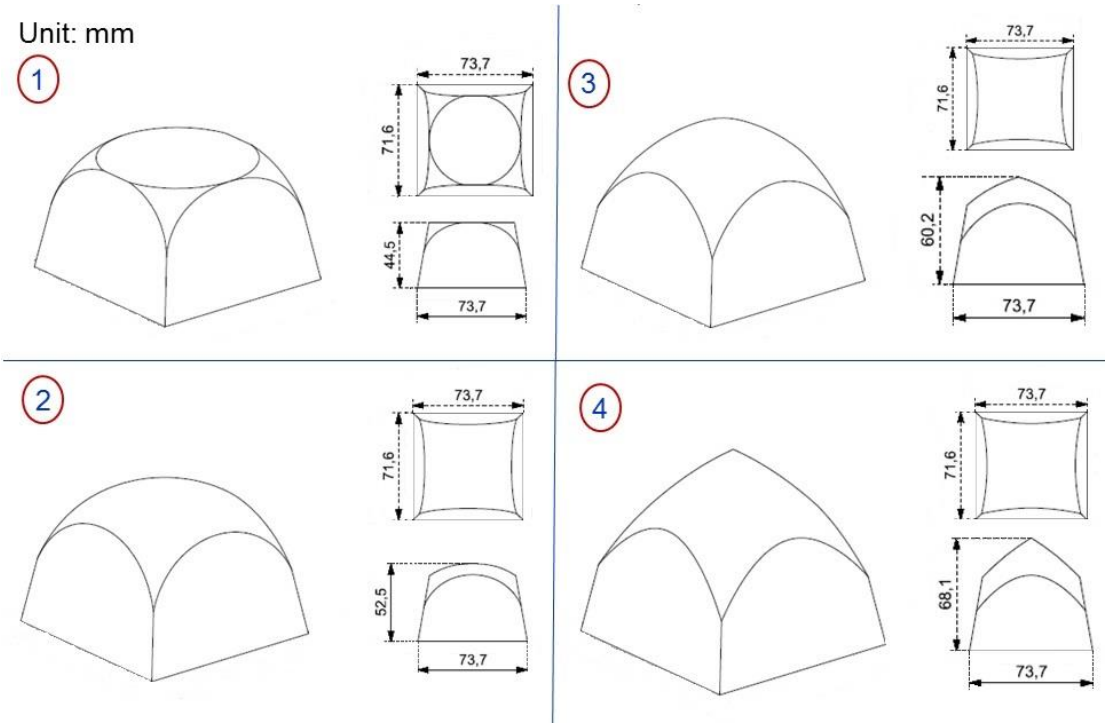

Figure 5-7: The designed pads dimensions. Four different pads are designed. Their differences are in the pad height, which leads to pad sharpness in the top point. Their behaviors will be evaluated in chapter 6 which relates to the simulation of the printing process.

Figure 5-8 and Figure 5-9 presents the positive form and the final products during the production process of pads. A stereolithografic 3D printer (Formlabs Form 2, PreForm software for pre-processing) prints the positive forms. They are used to prepare the pad molds with a more cost-efficient and innovative method. Then, four different designed pad molds are filled with silicone rubber material with four different hardnesses of 3, 6, 12 and 18 Shore A. In each case three times the same pads are molded. The preparation of pad molds and the silicone rubber pads are ordered at Tampo-Technik company. These pads are manufactured in the normal and completely similar production process same as other common pads on the market.

Figure 5-8: The 3D printed positive forms. They are printed after designing and drawing the desired pads.

Figure 5-9: The produced silicone rubber pads. The four designed pads are produced with four different hardnesses of 3, 6, 12 and 18 Shore A. In each case three times the same pads are molded. Totally, 48 pads are produced.

In a summary, the method of designing a pad was presented in this chapter. In this method, for the first time a mathematical method was introduced to design a pad. The method of getting the mathematical equations for designing rectangular pads is presented as a sample. For other types of pads, the same process can be performed to achieve their mathematical equations. In this case, novelty is the use of mathematical equations to design the desired pads according to the user's demands. Another novelty in the production procedure is the use of a 3D printer to produce the positive forms. Before introducing this method, the production process was expensive because of producing the positive forms in a complex procedure with metal (Lück, 2017a). These novelties lead to decrease the pad production price and designing a pad with an organized and more accurate method. This method is used for designing and manufacturing of a pad which was optimized according to printing condition. So, it leads to improve the automation level of indirect gravure printing process because of optimization of its process.

Further, totally, 48 pads are produced according to described case study. The pad height is changed in this case. Mathematically, the increase in pad height when other parameters are constants, will affect directly on the pad sharpness. The effect of the pad height on the pad surface displacement will be discussed in simulation results of chapter 6. They will be used to measure the force-displacement in the printing process for comparison of the printing process results with simulation results in chapter 6.

6 Simulation of the pad behavior

A process simulation is part of the automation execution on a process (Meyer et al, 2009; Tzafestas, 2010). The automation execution can lead to process optimization (Araújo et al, 2018; McClellan, 1997). Therefore, the simulation possibility in the indirect gravure printing will be investigated as an improvement in its automation level.

So in the first part, the general process of simulation is explained and specific parameters to simulate the indirect gravure printing are described. In the second part, a plan to perform the simulation process is defined. In the third part, the validation of simulation is examined and measured. In the fourth part, simulation results are studied. They are discussed as a case study with considering the displacement of pad surface during the printing process. Finally, an effect of the simulation process to improve the automation level of indirect gravure printing will be explained.

6.1 Simulation process

To get the mechanical behavior of pad in the printing process, two methods can be considered, experimental measurement of mechanical behavior of the pad during the printing process or simulating the printing process with investigation of the mathematical results of finite element analysis (FEA). The experimental measurements of parameters are not cost-efficient because of expensive measurement tools, consumable material and work force. So, in this dissertation, the simulation of printing process will be used to investigate the mechanical behavior of the silicone rubber pad in the indirect gravure printing process. It is explained in (Harish, 2018) that the finite element method (FEM) is a numerical technique used to perform FEA for solving problems of any physical phenomenon. It is useful for problems with complicated geometries and material properties where analytical solutions can not be used.

The silicone rubber is a hyperelastic material which can be defined by different material models described before such as Polynomial, Reduced Polynomial, Ogden and so on. Therefore, a simulation software should be selected which is able to support hyperelastic material models. In this case, there are different software such as

ABAQUS, ADINA, ANSYS, Autodesk Simulation Mechanical, Solidworks Simulation and so on. Here, ABAQUS is selected because of supporting more material models which are useful for silicone rubber simulation (Huri, 2018).

A simulation process in finite element method (FEM) software ABAQUS is divided into nine segments (Chen, 2016). Figure 6-1 shows these segments.

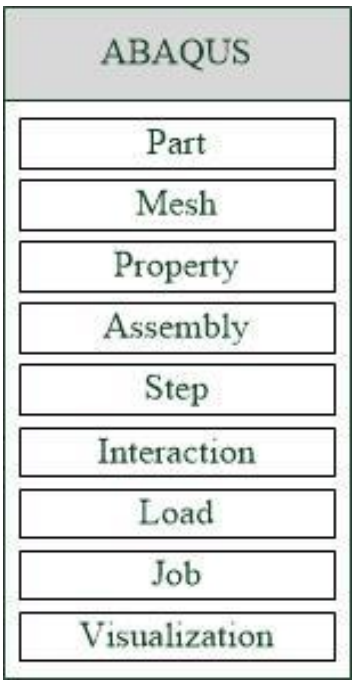

Figure 6-1: The simulation process of FEM software ABAQUS. The simulation segments (one to nine) are presented here. The figure is based on (Chen, 2016).

"Part" as a simulation segment is a geometry to investigate. Here, there are two parts: pad and substrate table. So, their geometries should be defined in the "Part" segment. Then, the parts volume is divided into discreate cells in the "Mesh" segment. This procedure is called meshing. Afterwards, material and mechanical properties of the parts are defined in the "Property" segment. Then, position of parts in the problem is determined in the "Assembly" segment. Physical steps of interaction between parts are defined in the "Step" segment. Then, interaction situations between parts are adjusted in the "Interaction" segment and a loading behavior for parts is described in the "Load" segment. "Job" is used to start the simulation calculations. Equations are solved during the execution of the "Job" segment. "Visualization" shows the results of simulation process. Analysis of the simulation results is possible in this segment.

The simulation of the indirect gravure printing process is performed with FEM software ABAQUS version 6.13. The pad and the substrate table are two parts in the simulation process. In literature (Wu et al, 2018), the silicone rubber material is simulated with mesh element type of C3D8RH. In this case, the experiment results and simulation results are in a good agreement with maximum error of less than 10%. So, the mesh element type C3D8RH is selected. It describes an eight node linear brick, hybrid, constant pressure, reduced integration, hourglass control mesh element for all elements. Further, in this case, a fine element size of 3 mm is selected to define the mesh's density.

The pad and substrate table materials are isotropic. It means their material properties in all directions are identical. The pad material is silicone rubber as a hyperelastic material. Here, the silicone rubber material with hardnesses of 3, 6, 12 and 18 Shore A were used. The material specifications of silicone rubber with these hardnesses were described in chapter 4. The substrate table material is steel C45 with Young's Modulus of 2.1E11 Pa and poisson's ratio of 0.3.

In the simulation process of the hyperelastic materials, the material model definition is the most important parameter. As the simulation model verification, the different material models were compared in chapter 4.4 and the fitted model with material test results was selected. The R-squared between the model and material test results for each hardness of silicone rubber was reported in chapter 4.

So, according to chapter 4.4, the polynomial order 2 model is selected as a strain energy potential model of material. The poisson's ratio values for silicone rubber with different hardnesses are selected according to the calculated values in Table 4-5.

6.2 Simulation plan

A plan can be designed to get a simulation goal. The simulation plan consists of different issues such as parameters, nodes, models and others which are investigated in the simulation results to get the goal.

The simulation results are useful to study effective parameters during the printing process. So, one possibility to simulate the indirect gravure printing process will be investigated in this chapter.

Figure 6-2 shows some cells and points on the pad surface which are called elements and nodes in the simulation results. They are produced after the meshing of the pad in the simulation process. Each point on the pad surface has a displacement in a 3D coordinate system during applying pressure on the substrate. The displacement can be described in XYZ Cartesian coordinate system.

The pad moves in Z-direction. A displacement in X-direction and Y-direction is occurred when the pad surface points have a contact with the substrate.

In the printing process, the pad surface transfers a 2D image on XY-plane of the substrate surface. So, a displacement of the pad surface points in X and Y directions affects on printing results distortion. The positions of pad surface points in X and Y directions before having a contact with the substrate are called initial positions or original positions in X and Y directions. During a pressing of the pad on the substrate, the surface points of the pad have a movement in comparison with their original position which is called pad displacement in X and Y directions.

So, as a case study a displacement of the pad surface during the printing process will be studied. A pad displacement depends on a force of the pad to the substrate which is called printing force. In this case study, the printing force for pad displacement is considered 100 N, because this is a typical value supported by four different pads of Figure 6-3 with four different hardnesses.

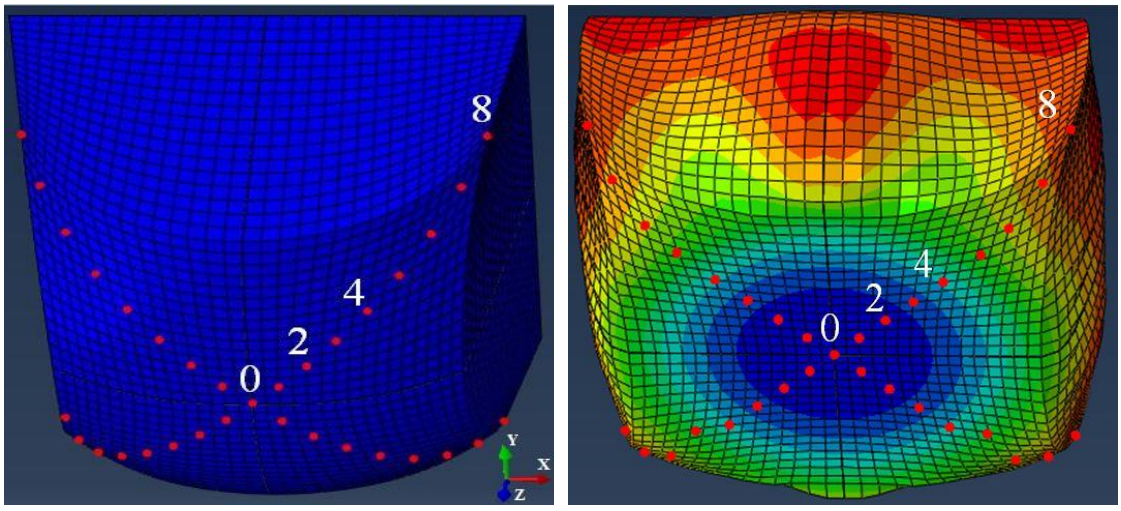

(a) (b)

Figure 6-2: The pad surface points for an undeformed pad (a) and the deformed pad under pressing (b) are shown. An arc between the pad tip and pad side is displayed here. Some points on

this path were numbered from 0 to 8 as an example. These points are some nodes in the simulation process with FEM software ABAQUS.

Further, the pad surface has a circular symmetric shape around Z-axis. The pad tip is located in the center of Z-axis. So, the displacement of the pad surface points located on a circle with the same radius from Z-axis (as a center of this circle), are similar to each other. So, the displacement behavior of the pad surface points located on an arc between the pad tip and a pad edge, can be a suitable sample to investigate the points displacement on the pad surface. Therefore, in this study, the displacement of points located on this arc will be investigated as a representative of the pad surface points.

Figure 6-2 shows eight points which are located on an arc between the pad tip and the pad edge as an example. The displacement of the pad surface in this area will be discussed in the simulation results of this chapter.

In addition, the pad displacement depends on the pad geometry and pad hardnesses. So, to evaluate this issue, four different pads and four different hardnesses are investigated. The pads with different geometries are called pad 1, pad 2, pad 3 and pad 4 which were shown in Figure 5-7 and their designing method was described in chapter 5.2. The equations in chapter 5.1 describe the designing parameters of a pad. In this case study, an effect of the pad height on the pad surface displacement is investigated. So, the pad height is considered as a variable and other designing parameters are considered constant. Figure 6-3 shows four different pads and related heights in a comparative view. According to Figure 6-3, changing of the pad height leads to pad sharpness changes. In this figure, the tip of the pad with H4 is sharper than other pads with smaller heights. For pads with different geometries, it is expected that points on the pad surface indicate different displacements during pressing.

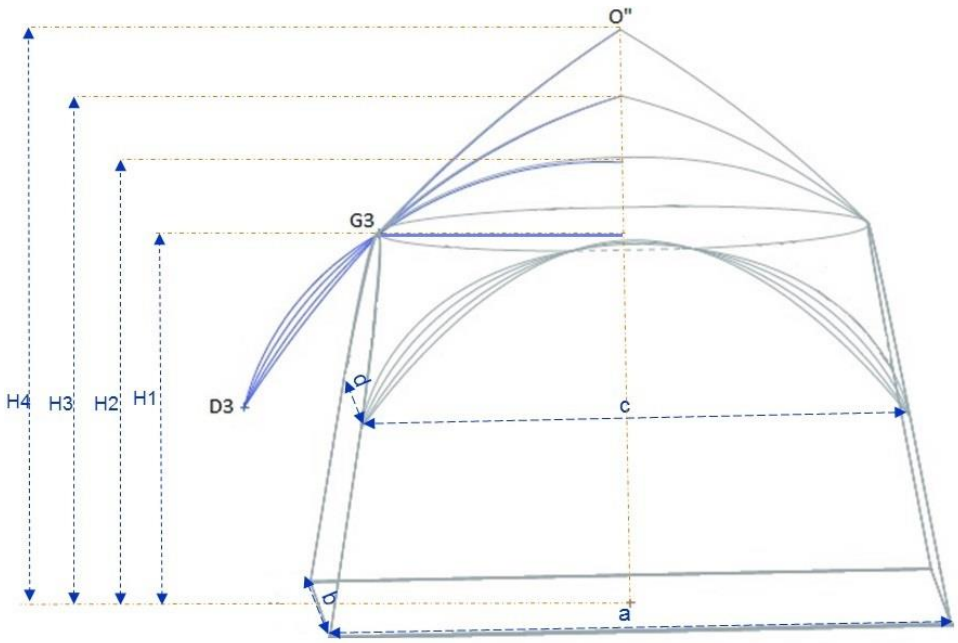

Figure 6-3: The comparative view of four different pads. H1, H2, H3 and H4 are the heights of pad 1, pad 2, pad 3 and pad 4 with amounts of 44.5, 52.5, 60.2 and 68.1 mm, respectively. Other parameters and single view of these pads were described in chapter 5.2.

The pad gets the ink from printing form cells and then transfers the ink to the substrate. The printed image in the indirect gravure printing method is made of small printed dots positioned together. The displacement of the pad surface in X and Y direction will affect displacement and deformation of printed dots' frame which can lead to a decrease in the printing results quality. In addition, the printed dots on a circle with the same radius from the center of the pad (pad tip) show the same displacement because of circular symmetry of the pad surface.

Therefore, X and Y Cartesian coordinate system is converted to Polar coordinate system. In a Polar coordinate system, the results are presented with a radius (R) which is a distance from a reference point and an angle (Theta) which is an angle from the reference direction. Here, the reference point is the pad tip, which is the contact point of X and Y axes. The reference direction is X-axis direction. So, in simulation results of this chapter, the results are presented with polar variables of R and Theta. R is a distance from the pad tip with the unit of millimeter (mm) and Theta is an angle from X-axis with the unit of degree which is shown with deg or °. Figure 6-4 shows schematically a concept of R and Theta variables.

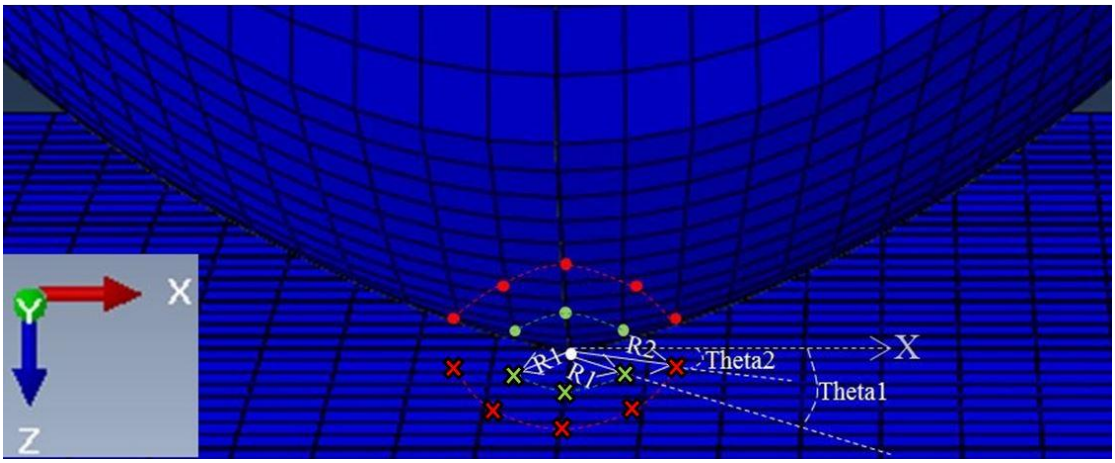

Figure 6-4: The schematic of pad surface points in a Polar coordinate system. The green and red points are located on circles with a radius of R1 and R2 from the pad center, respectively. Theta is an angle of each point from X-axis. The white point in the center is the pad center. The points with "X" markers which are located in the downward direction of the pad center, are a projection of pad surface points onto XY-plane.

In Figure 6-4, some points are marked in two circular positions on the pad surface with red and green colors. Their projections are displayed on the substrate surface with "X" markers and with the same color of the points on the pad surface. The distance between the projection of points and pad center is displayed with R.

6.3 Simulation validation

A comparison between simulation results and experiments is performed to validate the simulation results. In this case, the ability of the developed indirect gravure printing machine described in chapter 2.3, is considered to measure the printing force and pad displacement during a printing process.

Here, four different pad models of pad 1, pad 2, pad 3 and pad 4 with four different hardnesses of 3, 6, 12 and 18 Shore A are used in the experiments. They were produced according to the method described in chapter 5.2. For each pad model with a unique hardness such as pad 2 with hardness of 3 Shore A, three similar pads were produced. In total there are 48 pads for a test process execution.

The pad behavior during a printing process under pressure is tested. Force changes and pad displacement in Z-direction is measured during this test. Each test is repeated three times to increase the measurement certainty of the machine and measurement devices. The same test procedure is performed for three pads with the same model and the same

hardness to consider the possibility of measurement error because of the pad material or the pad production process. For example, nine tests with same procedure is performed for a pad with model pad 2 and hardness of 3 Shore A. Then, an average and a deviation between these nine test results (experiments) are calculated. Figure 6-5 shows average, minimum and maximum curves of nine tests (experiments) which were performed in the same procedure on a pad with model of pad 2 and hardness of 3 Shore A. It presents the force values in comparison with pad displacement in Z-direction during a pad pressing on the substrate in the indirect gravure printing process.

All tests are executed in the same air-conditioned laboratory where the material tests were performed (see chapter 4.2.1). Totally, 144 experiments are executed under the described conditions.

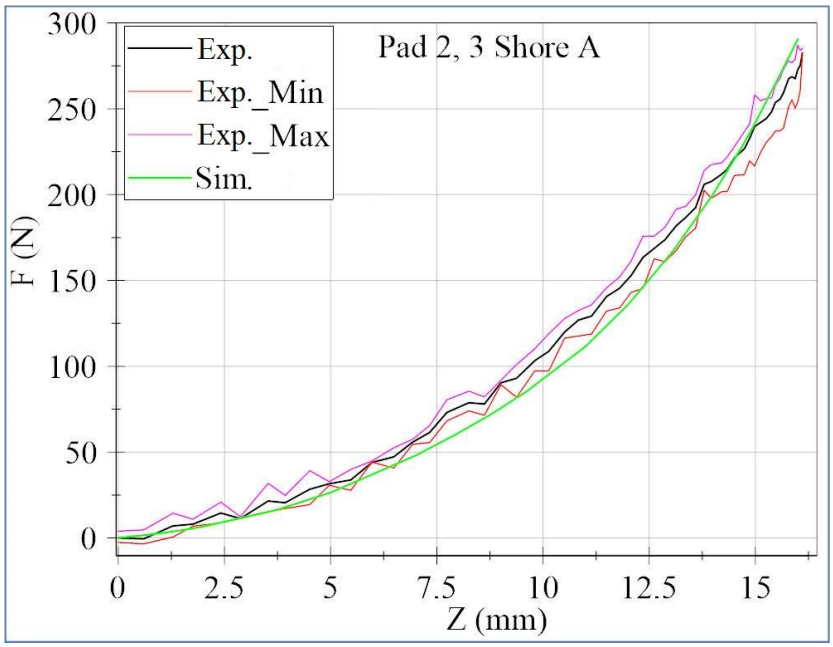

Figure 6-5: The force (F) versus the pad displacement (Z) during the pressing of the pad on the substrate for pad 2 with hardness of 3 Shore A is shown here. The black, red and violet colors present the average (Exp.), minimum (Exp._Min), maximum (Exp._Max) of experiment results. The green color displays simulation (Sim.) result.

Further, the simulation result is displayed in Figure 6-5. It is compared with average values of force achieved in the experiments to validate the simulation result. The comparison shows that the simulation result and the result of the experiments are matched with each other in a highly accurate condition with R-squared of 0.985. R-squared is the coefficient of determination. In this case, a more appropriate fitting between the simulation result and experiments is achieved while R-squared value is near

to one. Figure 6-6 shows the simulation results and experiments in different cases which will be discussed in this dissertation. It presents the force values in comparison with pad displacement in Z-direction during a pad pressing on the substrate in the indirect gravure printing process. Black, red, green and blue colors represent the pad models of pad 1, pad 2, pad 3 and pad 4. "Δ", "*", "□" and "x" markers on the curves represent the pad hardnesses of 3, 6, 12 and 18 Shore A. Solid and dashed lines indicate the experiments and simulation results, respectively.

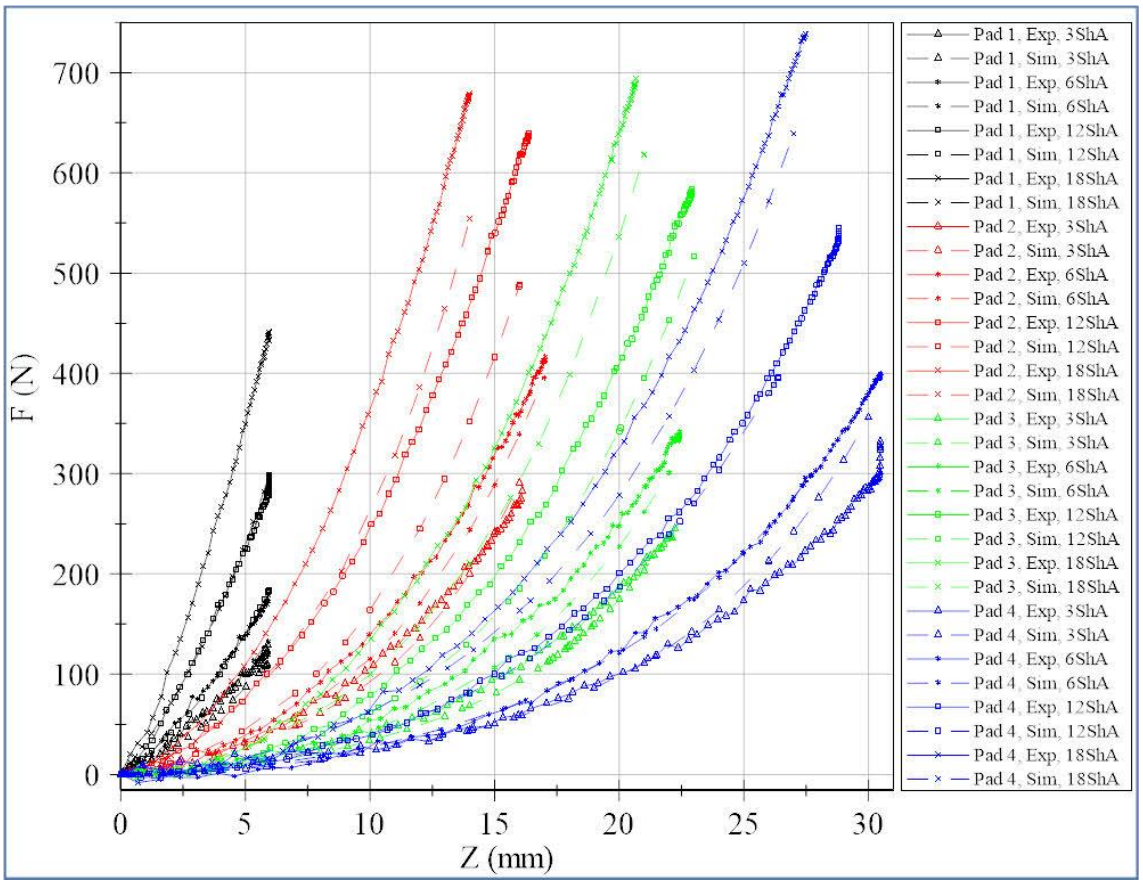

Figure 6-6: The pad force versus pad displacement in Z-direction is presented on the curves. Here, the simulation results with solid lines are compared with the experiments with dashed lines. The hardnesses of 3, 6, 12 and 18 Shore A are displayed by "Δ", "*", "□" and "x", respectively. Pad 1, pad 2, pad 3 and pad 4 are shown by black, red, green and blue colors, respectively.

According to Figure 6-6, the deviation between the curves of experiments and simulation results in the pads with model pad 1 is more than other models. The differences between the simulation results and experiments in pad model 4 with hardness of 12 Shore A is the smallest amount and they are fitted with each other.

Table 6-1 shows the fitting between the simulation results and experiments with R-squared parameter. It is the coefficient of determination. This parameter was described in chapter 4.4 and it is calculated by equations (4-5), (4-6) and (4-7). Table 6-1 structure was designed to make an easier comparison between different pad models and pad hardnesses. In the table, the quantitative parameters are described in a matrix format which each value is related to a special pad hardness and pad model. Columns and rows are related to pad hardnesses and pad model, respectively.

In Table 6-1, R-squared value describes how well the simulation results fit the experiments in each case. The value which is nearer to one, shows more fitting between simulation results and experiments. This is a quantitative parameter to describe the validation of simulation results.

For example, R-squared is 0.995 in the case of pad 4 with hardness of 12 Shore A. In this case, the simulation results can be considered nearly the same as experiments which were performed with this pad during the printing process. Oppositely, R-squared of 0.350 in the case of pad 1 with hardness of 12, shows a non suitable similarity between the simulation results and experiments.

Table 6-1: The accuracy of fit of simulation results with experiments in force-displacement behavior of pads is abstracted here. The R-squared is the coefficient of determination. They are related to pad 1, pad 2, pad 3 and pad 4 with hardnesses of 3, 6, 12 and 18 Shore A.

R-squared	3 Shore A	6 Shore A	12 Shore A	18 Shore A
Pad 1	0.9432	0.7865	0.3507	0.5191
Pad 2	0.9852	0.9791	0.7978	0.8094
Pad 3	0.9864	0.9749	0.9321	0.8988
Pad 4	0.8527	0.9077	0.9951	0.9637

The validation of simulation results was evaluated according to Figure 6-6 and Table 6-1. In this case, the simulation results of the two cases between 16 different cases are not as accurate as others and their R-squared is less than 0.79. They are pad 1 with hardnesses of 12 and 18 Shore A. In other cases, there is a high similarity between the simulation results and experiments. In pad 4 with hardness of 12 Shore A, R-squared value is in the highest value of 0.99. The results of pad 1 are not accurate because of special geometry of the pad. In this case, the pad was designed to observe its behavior

with minimum possible height. In real case, this geometry never will be used in the printing process. So, it is validated that the simulation represents the real pads behavior.

6.4 Simulation results discussion

As described in chapter 6.2, a point on the pad surface is defined by R and Theta parameters. R is a distance (radius) from the tip point of the pad and Theta is the angle from X-axis. In Figure 6-8, generally there are two types of figures. The figures which are related to R_d as a pad displacement amplitude and the figures which are related to Theta_d as a pad displacement angle. They are displayed in Figure 6-7. The pad displacement amplitude shows the displacement magnitude of a point on the pad surface after pad pressing with 100 N in the indirect gravure printing process. The pad displacement angle shows the angular changes of a point on the pad surface after pressing the pad with a force of 100 N in comparison to the original angle. The horizontal axis in these figures is R_o. It is related to the original (before displacement) position of the points. This position is the amplitude of the pad points selected from the tip of the pad to the pad angle, before having a contact of the pad with the substrate. The original angle Theta_o of these points is 44 deg. Shortly, the points on the pad surface are projected on a two dimensional plane which is parallel to XY-plane of the coordinate system and it passes through the pad tip.

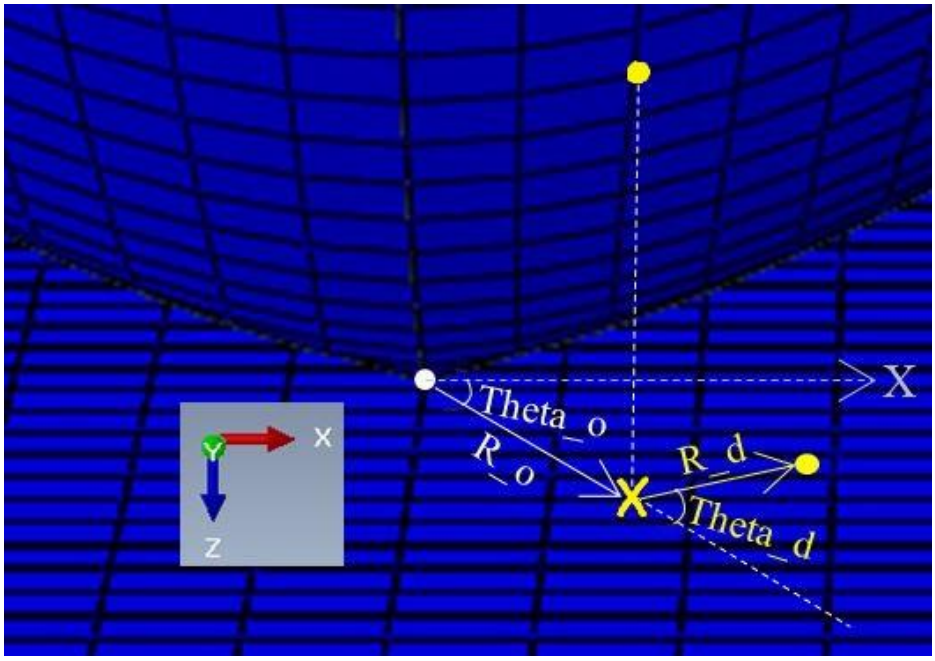

Figure 6-7: The concept of R_o, Theta_o, R_d and Theta_d parameters. The white point is a point on the pad surface. The point with "X" marker is a projection of pad surface point onto XY-plane. The yellow point is the position of pad surface point onto XY-plane after printing.

Figure 6-8 shows the amplitude and angle displacements versus the original position of the points on the pad surface on a defined path. The path starting point is the pad tip. The last point of the path is located on the pad edge. Each figure relates to a special pad geometry with four different hardnesses of 3, 6, 12 and 18 Shore A.

Figure 6-8 (a) and (b) is related to the simulation results of pad 1 with a height of 44.5 mm which was shown in Figure 5-7. The surface of this pad is flat. The use of a flat surface in a printing process is unusual. It is selected as a minimum height to complete the range of changes in the pad height. Its surface geometry leads to a maximum R_o 30 mm while it is 45 mm for pad 2, pad 3 and pad 4. In Figure 6-8 (a), an increase in displacement amplitude (R_d) is observed with increase of distance from the pad tip (R_o). The range of R_d as displacement in pad 1 in comparison with other pads is very small. The maximum displacement is 0.007 mm, because of its flat geometry. So, the amplitude of displacement in this case can be ignored. The displacement angle in Figure 6-8 (b) shows a large amount of variation in angle values in pad 1 with hardness of 3 Shore A. For pads with model pad 1 and different hardnesses, the angle changes are increased for the points of the pad that are located at a distance of more than 15 mm from the pad tip point.

Figure 6-8 (c) and (d) are related to the simulation results of pad 2 with a height of 52.5 mm. The pad geometry was shown in Figure 5-7. Figure 6-8 (c) shows an increase in the displacement amplitude with an increase in the distance from the pad tip. Also, the enhance of pad hardness leads to a decrease of the pad displacement in pad 2. The effect of pad hardness on displacement amplitude is more sensible in the pad surface area which its distance is more than 20 mm from the pad tip. In this case, the printing results with the use of a harder pad such as 18 Shore A, is deformed less than the printing results of a softer pad such as 3 Shore A. The pad with hardness of 3 Shore A as a soft pad shows more changes in displacement angle while pads with other hardnesses don't show major changes. The maximum displacement angle is 5 deg. So, the effect of the displacement angle (Theta) is small and can be ignored in the pad 2 and other pads with similar geometry.

Figure 6-8 (e) and (f) is related to the simulation results of pad 3 with a height of 60.2 mm which was shown in Figure 5-7. Figure 6-8 (e) shows a growth of displacement amplitude with an enhancement of the distance from the pad tip. The growth of pad hardness, reduces the amplitude of displacement and it leads to less deformation of print results. In Figure 6-8 (f), an increase in the displacement angle of pad with 3 Shore A hardness is observed. There is a maximum angle change of 15 deg in a small area of pad surface for pad 3 with other hardnesses. For other areas on the pad surface, there is not a large amount of changes in the displacement angle. So, the amplitude of the displacement is more effective on deformation of printing results in comparison with displacement angle. According to the curves of displacement amplitude for different hardnesses, it can be concluded that printing with a harder pad in the model of pad 3 shows less deformation in printing results.

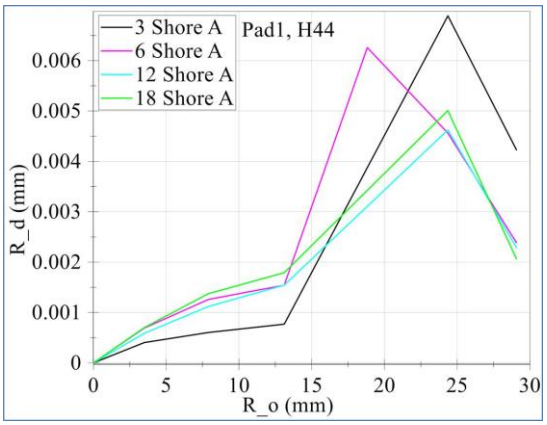
3 Shore A
6 Shore A
12 Shore A
18 Shore A
Pad1, H44
R_d (mm)
R_o (mm)

(a)

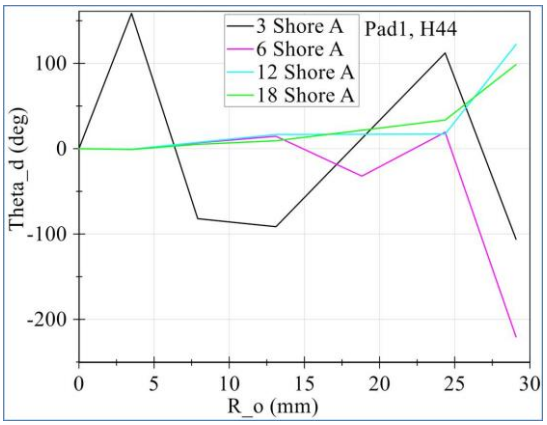
3 Shore A
6 Shore A
12 Shore A
18 Shore A
Pad1, H44
Theta_d (deg)
R_o (mm)

(b)

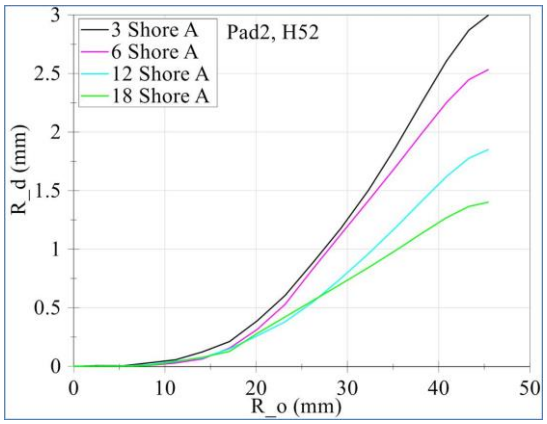
3 Shore A
6 Shore A
12 Shore A
18 Shore A
Pad2, H52
R_d (mm)
R_o (mm)

(c)

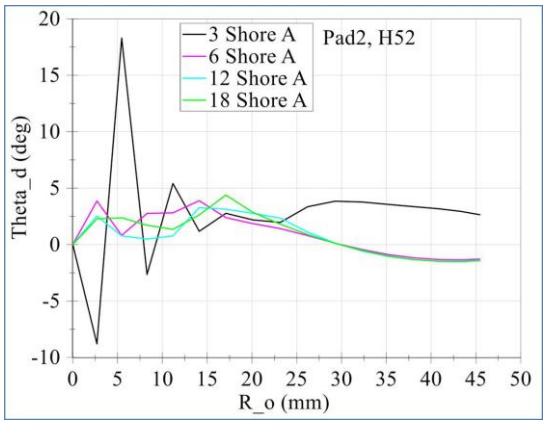
3 Shore A
6 Shore A
12 Shore A
18 Shore A
Pad2, H52
Theta_d (deg)
R_o (mm)

(d)

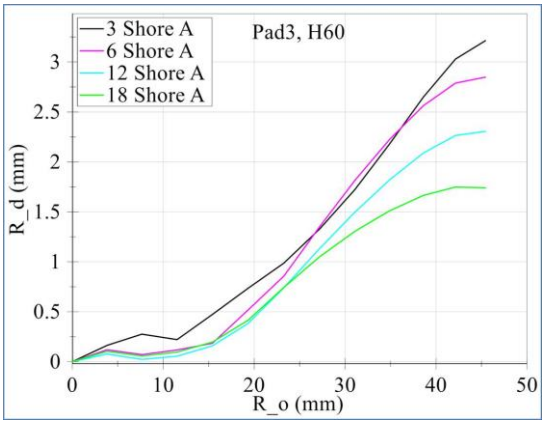
3 Shore A
6 Shore A
12 Shore A
18 Shore A
Pad3, H60
R_d (mm)
R_o (mm)

(e)

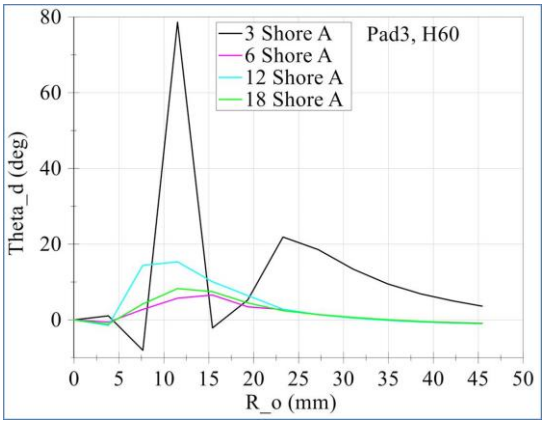
3 Shore A
6 Shore A
12 Shore A
18 Shore A
Pad3, H60
Theta_d (deg)
R_o (mm)

(f)

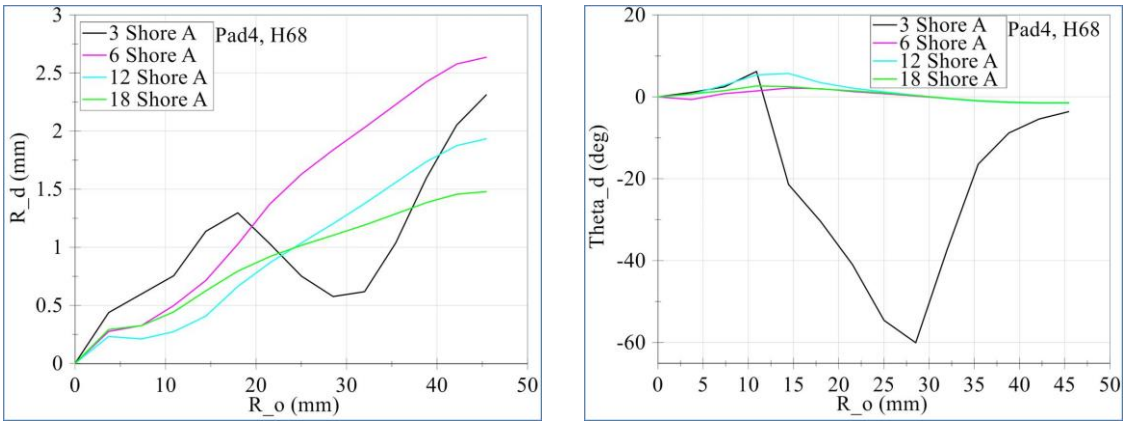

(g) (h)

Figure 6-8: The displacement amplitude of pad 1 (a), pad 2 (c), pad 3 (e) and pad 4 (g) and the displacement angle of pad 1 (b), pad 2 (d), pad 3 (f) and pad 4 (h) are shown here. The black, pink, turquoise and green lines are related to the pads with hardness of 3, 6, 12 and 18 Shore A, respectively. The horizontal axis relates to the original position R_o of the points. It is the distance between a point on the pad surface and pad tip projected on XY-plane. R_d is the displacement in amplitude during pressing the pad with 100 N and Theta_d is the displacement in angle during pressing the pad with 100 N. The height of each pad is mentioned after "H" in the legend with a unit of mm.

Figure 6-8 (g) and (h) are related to the simulation results of pad 4 with a height of 68.1 mm which was shown in Figure 5-7. Pad 4 is the highest and sharpest one of the pads described. Figure 6-8 (g) shows the displacement amplitude of pad 4 with 3, 6, 12 and 18 Shore A hardnesses. Figure 6-8 (h) displays the displacement angle of this case. Here, on the one hand there are more changes in displacement angle of pad 4 with hardness of 3 Shore A in comparison with other hardnesses, but on the other hand the displacement amplitude R_d with the same R_o values presents less changes in R_d values for pad 4 with hardness of 3 Shore A. It is interpreted as more angular displacement in comparison with radial displacement. This behavior happens in this case because of high sharpness in geometry and softness in material of pad which leads to more freedom for angular displacement.

To sum this up, the pad surface displacement is an important issue because the magnitude of displacement of pad surface points effects on the dimensions of the printed dot and the angle of displacement deflects the printed dot position.

According to simulation results, it can be concluded that the displacement of the pads in an area near to the pad tip is smaller than in other parts. Generally, the displacement in harder pads is less than in softer pads. The simulation results help to detect the suitable

printing area in different pads to get the printed dots with less deformation and deflection.

6.5 Improvement of automation level

The automation levels were described in chapter 2.1.3. The automation level of conventional indirect gravure printing processes is located at level 1. Part of the improvement in the automation level of indirect gravure printing process was presented in chapter 3.5. Here, the effect and the condition of the process simulation to improve the automation level of this printing process are described.

Computer aided engineering (CAE), computer aided manufacturing (CAM) and computer aided flow planning are part of automation level 3 (Meyer et al, 2009). According to (Meyer et al, 2009), CAE consists of all possibilities of computer support in the development of a product. So, a modeling of product and a simulation of the production process are basis to use the results in CAE. Further, the simulation of work steps can be considered as basic knowledge to perform the work planning in CAM. So, the simulation of production process leads to achieve the automation level 3.

According to chapter 2.1.3 and Figure 2-5, the automation level 3 is related to optimization of production processes. The manufacturing execution system (MES) is located at this level. MES leads to improve a production output with optimization of current conditions in a production process (McClellan, 1997). Here, the production process is the process of indirect gravure printing that should be optimized. So, in order to improve the automation level of indirect gravure printing process, printing conditions should be optimized in different cases.

Figure 6-9 shows an optimization process for each printing case in an indirect gravure printing process. Here, each printing case is considered as a problem with variables of the printing conditions that should be optimized. The different parts to solve this problem are described in the following.

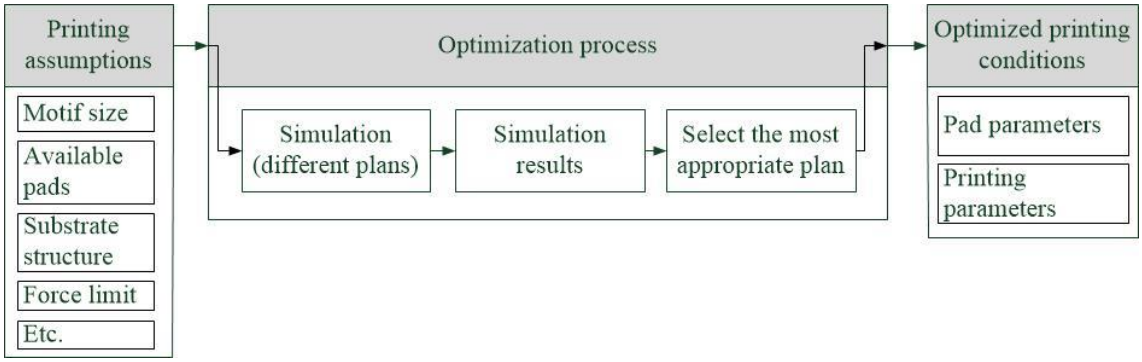

Figure 6-9: The optimization of printing process with use of simulation. Each arrow direction shows a sequence to next optimization step.

In each problem, there are some assumptions. Here, the assumptions of the problem are related to the printing case situation such as motif size, available pads for printing and so on. The optimization process is performed with simulation of the printing process. The simulation is executed in the method described in this chapter. According to the assumptions, different simulation plans can be executed. So, there are different simulation results. According to the results of different simulation plans, the most appropriate simulation plan will be selected. In this case, the appropriate simulation plan is one of the plans with minimum displacement in amplitude and angle. Then, the optimized printing conditions can be achieved according to the results of the selected simulation plan.

The optimized printing conditions are the adjustable parts of printing process which can be set according to problem solution. In this case, the printing conditions are divided into printing parameters and pad parameters. The printing parameters relate to the printing machine set points such as printing speed, pad displacement, printing force and so on. The relevant pad parameters are pad geometry and pad hardness.

So, the optimized printing parameters and pad parameters vary according to the assumptions in each printing case. These optimized parameters are the parameters of printing and pad which lead to the appropriate simulation plan described above.

For example, there is a motif with a maximum size of 8 mm. It should be printed on a flat substrate and the substrate withstanding force of 100 N. This is a printing case which printing conditions should be optimized according to this case. The optimization process is described in the following.

As a note, according to the expert's experiments the position of a motif should be located on a side of a pad and the center of the pad should not have a contact with motif

area. In this case, the position of printing area (motif) is considered from 2 mm to 10 mm from the original position R_o while R_o of the pad center is 0 mm. So, the farthest point of the motif is located in a radius of 10 mm from the pad center. According to the simulation results in Figure 6-8 (a, c, e and g), the displacement amplitude is less in pad 2 with hardnesses of 3, 6, 12 and 18 Shore A and pad 3 with hardnesses of 6, 12 and 18 Shore A compare to others. Then, according to Figure 6-8 (d and f), the displacement angle in pad 2 with hardness of 3 Shore A and pad 3 with hardness of 12 Shore A are high and because of that not suitable. So, in this case, the pad geometry and hardness can be selected between pad 2 with hardnesses of 6, 12 and 18 Shore A and pad 3 with hardnesses of 6 and 18 Shore A. According to Figure 6-6 and Table 6-1, pad 2 with hardness of 6 Shore A is selected because of more accurate fitting between the simulation results and experiments with R-squared of 0.979. Therefore, the pad parameters are properly selected for this case.

Then, according to the printing force of 100 N and Figure 6-6, pad 2 with hardness of 6 Shore A should move 8.5 mm in Z-direction. This is a printing parameter. This value as a set point is entered into the printing position field of SP_UI of the developed indirect gravure printing machine described in chapter 2.3.

So, the printing process can be optimized for different printing cases with the help of the simulation. Therefore, the automation level 3 for the indirect gravure printing is achieved by the use of the methods shown in this study.

7 Conclusion and Outlook

Conclusion

The main goal of this dissertation is the improvement in the automation level of the indirect gravure printing process with a focus on the mechanical characteristics of the silicone rubber pads. According to above goal, two main actions are presented in this dissertation. They are machine structure development and simulation of the printing process. A conclusion of these actions and their effects on the automation level is given in the following.

First, an indirect gravure printing machine structure is developed with the goal of highly accurate data measurement, processing and controlling with a high speed data transferring. So, some developments are applied such as use of a force sensor, National Instrument CompactRio hardware and Kollmorgen servo drives over EtherCAT data transferring protocol. The purpose of this development is the measurement and control of the effective parameters during the printing process. In this case, the printing velocity, the printing position, printing time and printing force are measured and can be controlled online. They are effective parameters that are related to the role of the pad during the printing process. The developed indirect gravure printing machine explained here is able to monitor online the printing process and printing parameters. It displays these parameters online on the user interface of the machine. So, it leads to achieve the automation level 2 in the process. In addition, saving and reuse of printing parameters for next times, according to feedbacks of the monitored data, are possible. Also, the user is able to store, handle and trace data with the use of DIAdem. These important improvements can establish the basis of an information management system for the indirect gravure printing. So, these developments lead to the improvement of the automation level of indirect gravure printing to level 3.

Second, in order to perform the simulation of the indirect gravure printing process the silicone rubber pad material model and the geometry of the pad are essential issues that should be considered.

The silicone rubber material model is achieved by execution of different mechanical tests which are described under the chapter of silicone rubber characteristics. In this dissertation, the uniaxial tensile, compression and planar tests are performed in an air-conditioned laboratory with a high accurate test condition according to the related standards. The test specimens are produced with the same material and by the producer of the pads. The hardnesses of test specimens are 3, 6, 12 and 18 Shore A. The test results of these test specimens led to achieve the hyperelastic material model of the silicone rubber pads to use in the simulation process.

In this dissertation a mathematical method to calculate the rectangular pad dimensions is presented for the first time. According to these equations, a calculator is programed by LabVIEW to calculate the geometrical parameters of pads. After using this calculator to get the parameters for the designing of pads, four different pads are designed. These pads are designed with four different heights while other parameters are considered the same to check the height effect on the displacement of the pad surface. The designed pads are designed in CAD (Computer Aided Design) software such as NX to get the pad geometry. Then, it is considered as a part to get transferred into the FEM software ABAQUS to execute the simulation process. Further, the pad geometries are used to prepare the pad molds. In this dissertation, a cost-efficient method to produce the pad molds by use of stereolithografic 3D printer is presented for the first time.

A method to perform a simulation of the printing process is described in the last chapter. Further, the validation of simulation results for different pads is evaluated. There are different parameters of a pad that effects on printing process results. As a case study, the effects of pad height and pad hardnesses on the displacement of pad surface are examined in simulation results of the last chapter. The results show that different positions on the pad surface have different amounts of displacements. Further, these values vary for different shape of pads and different hardnesses of pads. So, pad parameters should be optimized according to printing case. In this case, the simulation process of indirect gravure printing is executed and the effect of different pads on printing process is evaluated. Afterwards, the pad with most suitable results is selected and its mold can be prepared with e.g. a stereolithografic 3D printer. So, a unique pad according to a certain printing case is produced. Also, the related printing parameters such as pad speed, pad position and printing time can be achieved from the simulation results. These parameters are set in the indirect gravure printing machine developed in this dissertation. So, the printing process is optimized. To sum up, the printing process

can be optimized for different printing cases with the help of the simulation and designing of appropriate pad. So, the indirect gravure printing machine can be developed according to these conditions. Further, manufacturing execution system (MES), as part of the automation level 3, is a system which improves a production output with optimization of current conditions in a production process. Here, the production process is the process of indirect gravure printing that is optimized. These optimizations can be considered as basic knowledge to be integrated with MES. Therefore, the automation level 3 for the indirect gravure printing can be achieved in this study. It should be considered that mixing of process simulation and pad designing abilities in addition to developed indirect gravure printing machine lead to a complete optimization of the printing process. The method to achieve these abilities is described in this dissertation. Further, computer aided engineering (CAE) consists of all possibilities of computer support in the development of a product and it is part of automation level 3. So, a modeling of product and a simulation of the production process are basic knowledges to be integrated with CAE at level 3.

According to the outcomes of this dissertation the objective questions are answered in the following.

Is it practicable to improve the automation level of indirect gravure printing in the described direction? Yes, it is practicable to improve its automation level. It is improved from a basic level to level 3. It is achieved according to the basis of developments gained in different chapters of this dissertation.

Is it possible to investigate the mechanical behavior of pad in the printing process? Yes, the investigation of its behavior is possible with simulation of the mechanical behavior of the pad in the printing process. It is explained in chapter 6 of this dissertation.

What are the mechanical characteristics of the material of the pad (silicone rubber)? The mechanical characteristics of silicone rubber pad for different hardnesses are described in chapter 4. The hyperelastic material model is considered and the parameters of the model are achieved with execution of different tests. Finally, this model is used to simulate the process.

What is the geometry of the pad? Or how should the pad geometry and model be designed? For the first time, a method to design the geometry of the pad is introduced in this dissertation. In chapter 5, the calculation and designing method of rectangular pads

are described. These are applied to design pads with the rectangular geometries to use in the simulation process.

The scientific impact of this work is shortly described as follows. The development of indirect gravure printing machine structure, realization of the pad designing method, detecting a cost-efficient method for the preparation of pad molds with the use of the stereolithografic 3D printer and simulation of the printing process lead to improve the automation level of indirect gravure printing from level 1 (before this dissertation) to level 3.

Outlook

This scientific investigation gives the basis for level 3 but there are further subjects at this level which can be performed. They are described as follows. The method of designing a pad described in this dissertation can be applied to formulate other geometries of the pads such as saddle, round and so on. The possibility of increment of accuracy in some simulation results such as pad 1 with 12 and 18 Shore A can be investigated. Going from objects with flat surfaces to more uneven surfaces to investigate the pad behavior in the printing process can be evaluated. These subjects are interesting issues at this level for further researches.

Recently, new pads called hollow pads are presented to the market. There is a hole in the middle of those pads which cause the occurrence of a different mechanical behavior in the printing process. The simulation and evaluation of their mechanical behavior can be presented as a future work.

There is one type of anti-electrostatic silicone rubber pads which are used to decrease the hair effect defects in printing quality. The evaluation of this material and getting its material model is a useful research subject, to optimize this technique further.

Research on silicone rubber material with a wider range of hardnesses such as 1 Shore A until 30 Shore A, with steps of 2 Shore A is an interesting subject. Then, a statistical comparison between their tensile, compression and planar test results should be executed. So, a mathematical relationship between the silicone rubber hardness and related test results could be detected. This task is useful to predict the material parameters of silicone rubber for different hardnesses according to mathematical calculations.

Bibliography

(Amabili et al, 2016) Amabili, M., Balasubramanian, P., Breslavsky, I. D., Ferrari, G., Garziera, R. & Riabova, K., 2016. *Experimental and numerical study on vibrations and static deflection of a thin hyperelastic plate*. Journal of sound and vibration, 385, pp. 81-92.

(Anon., 2014) Anon., 2014. *PADS.* Engineered printing solutions. Available online: http://www.epsvt.com/Pads [Accessed Dec. 2014].

(Anon., 2018) Anon., 2018. *SHORE-Härte – Grundlagen.* Polymer service GmbH Merseburg. Available online: http://wiki.polymerservice-merseburg.de/index.php/SHORE-H%C3%A4rte [Accessed May 2018].

(Araújo et al, 2018) Araújo, A. F., Varela, M. L. R., Gomes, M. S., Barreto, R. C. C. & Trojanowska, J., 2018. *Development of an intelligent and automated system for lean industrial production, adding maximum productivity and efficiency in the production process*. In: Hamrol, A., Ciszak, O., Legutko, S. & Jurczyk, M. (eds), *Advances in manufacturing*. Cham: Springer international publishing. pp. 131-140.

(ASTM D412, 2016) ASTM D412, 2016. *Standard test methods for vulcanized rubber and thermoplastic elastomers - tension* ASTM International.

(ASTM D575, 2012) ASTM D575, 2012. *Standard test methods for rubber properties in compression.* ASTM International.

(ASTM D638, 2014) ASTM D638, 2014. *Standard test method for tensile properties of plastics.* ASTM international.

(ASTM D1349, 2014) ASTM D1349, 2014. *Standard practice for rubber - standard conditions for testing.* ASTM International.

(ASTM D2240, 2015) ASTM D2240, 2015. *Standard test method for rubber property - durometer hardness.* ASTM International.

(Azolibe et al, 2015) Azolibe, I., McGookin, E. W., Houston, J. & Winton, C., 2015. *Serving the data needs of multiple applications with one data source: an industry application case study*. Symposium on Information Control Problems in Manufacturing (INCOM). Ottowa, Canada, May 2015. IEEE.

(Bauman, 2012) Bauman, J. T., 2012. *Fatigue, stress, and strain of rubber components: guide for design engineers.*Carl Hanser Verlag GmbH Co KG.

(Beda, 2007) Beda, T., 2007. *Modeling hyperelastic behavior of rubber: A novel invariant-based and a review of constitutive models*. Journal of Polymer Science Part B: Polymer Physics, 45(13), pp. 1713-1732.

(Benedikt et al, 2017) Benedikt, F., Daniel, H.-Z., Matthias, M., Simon, S., Juliane, W. & Sven, W., 2017. *Optimierung einer Zugprüfmaschiner mit videobasiertem Extensometer zur Untersuchung von additiven Zugproben*. ADP, Supervisor: Arash Hakimi-Tehrani, Vinzenz Nienhaus. Technische Universität Darmstadt, July 2017.

(Bergstroem, 2015) Bergstroem, J. S., 2015. *Mechanics of solid polymers: theory and computational modeling.*William Andrew.

(Berselli et al, 2011) Berselli, G., Vertechy, R., Pellicciari, M. & Vassura, G., 2011. *Hyperelastic modeling of rubber - like photopolymers for additive manufacturing processes, Rapid prototyping technology - principles and functional requirements*. Rijeka: INTECH.

(Bodenstein, 2018) Bodenstein, C., 2018. *ELSE project.* Institute of printing science and technology, Technische Universität Darmstadt. Available online: http://www.idd.tu-darmstadt.de/re_search/projekte_1/aktuelle_projekte_1/else.en.jsp [Accessed Jul. 2018].

(Bodenstein et al, 2018) Bodenstein, C., Sauer, H. M., Hirmer, K. & Dörsam, E., 2018. *Influence of printing parameters in fully pad-printed electroluminescence panels on curved surfaces*. 19th international society of coating science and technology (ISCST). Long Beach, Sep. 2018.

(Casner et al, 2017) Casner, D., Houssin, R., Renaud, J. & Knittel, D., 2017. *An optimization - based embodiment design approach for mechatronic product development*. The open automation and control systems journal, 9(1), pp. 27-47.

(Chen, 2016) Chen, J., 2016. *Investigation on the mechanical behavior of paper and paper stacks in the out-of-plane direction*. PhD Thesis. Technische Universität Darmstadt, Nov. 2016.

(DECO, 2018) DECO, T. G., 2018. *Introduction to pad printing - pad printing 101*. DECO Technology Group. Available online: http://www.decotechgroup.com /library/pad-printing/tech-bulletin-pad-print-101/ [Accessed Aug. 2018].

(Dispersyn et al, 2017) Dispersyn, J., Hertelé, S., Waele, W. D. & Belis, J., 2017. *Assessment of hyperelastic material models for the application of adhesive point-fixings between glass and metal*. International journal of adhesion and adhesives, 77, pp. 102-117.

(ETG, 2014) ETG, 2014. *Ethercat - the ethernet fieldbus*. EtherCAT Technology Group. Available online: http://www.ethercat.de/pdf/english/ETG_Brochure_EN.pdf [Accessed March. 2015].

(Fahimi et al, 2018) Fahimi, S., Baghani, M., Zakerzadeh, M.-R. & Eskandari, A., 2018. *Developing a visco-hyperelastic material model for 3D finite deformation of elastomers*. Finite elements in analysis and design, 140(Supplement C), pp. 1-10.

(Flory & Volkenstein, 1969) Flory, P. & Volkenstein, M., 1969. *Statistical mechanics of chain molecules. 8*. New York: Wiley online library.

(Ga Eul et al, 2016) Ga Eul, K., Kyoohee, W., Dongwoo, K., Yunseok, J., Young-Man, C., Moon, G. L., Taik-Min, L. & Sin, K., 2016. *A study on the enhancement of the reliability in gravure offset roll printing with blanket swelling control*. Journal of micromechanics and microengineering, 26(10), pp. 1-7.

(Golovanov et al, 1996) Golovanov, V., Solis, J. L., Lantto, V. & Leppävuori, S., 1996. *Different thick-film methods in printing of one-electrode semiconductor gas sensors*. Sensors and actuators B: Chemical, 34(1–3), pp. 401-406.

(Hahne, 2001) Hahne, P., 2001. *Innovative Drucktechnologien: Siebdruck - Tampondruck.* Germany: Verlag Der Siebdruck.

(Hahne et al, 2001) Hahne, P., Hirth, E., Reis, I. E., Schwichtenberg, K., Richtering, W., Horn, F. M. & Eggenweiler, U., 2001. *Progress in thick-film pad printing technique for solar cells*. Solar energy materials and solar cells, 65(1–4), pp. 399-407.

(Hakimi Tehrani et al, 2016) Hakimi Tehrani, A., Dörsam, E. & Neumann, J., 2016. *Improving automation and process control of an indirect gravure (pad) printing machine*. Acta Polytechnica Hungarica, 13(4), pp. 221-240.

(Harish, 2018) Harish, A., 2018. *Finite element method – What is it? FEM and FEA explained.* SIMSCALE. Available online: https://www.simscale.com/blog/2016/10/what-is-finite-element-method/ [Accessed Aug. 2018].

(Hirmer et al, 2016) Hirmer, K., Schuster, P., Keil, F. & Hofmann, K., 2016. *Low-cost high-voltage arbitrary waveform generator for broad lifetime measurements of electroluminescent devices*. Power electronics conference (SPEC), IEEE annual southern. IEEE.

(Hoss & Marczak, 2010) Hoss, L. & Marczak, R. J., 2010. *A new constitutive model for rubber-like materials*. Mecánica computacional, 29, pp. 2759-2773.

(Huri, 2018) Huri, D., 2018. *Finite element software for rubber products design*. International journal of engineering and management sciences (IJEMS), 3(1), pp. 13-20.

(Isermann, 2008) Isermann, R., 2008. *Mechatronic systems-Innovative products with embedded control*. Control engineering practice, 16(1), pp. 14-29.

(ISO 37, 2012) ISO 37, 2012. *Rubber, vulcanized or thermoplastic - Determination of tensile stress-strain properties.* The British Standards Institution.

(ISO 7743, 2011) ISO 7743, 2011. *Rubber, vulcanized or thermoplastic - Determination of compression stress-strain properties.* The British Standards Institution.

(Izumi et al, 2018) Izumi, K., Yoshida, Y. & Tokito, S., 2018. *Improved fine layer patterning using soft blanket gravure printing technology*. Flexible and printed electronics, 3(1), pp. 015011.

(Kiel, 2008) Kiel, E., 2008. *Drive solutions: mechatronics for production and logistics.* Heidelberg: Springer science & business media.

(Kipphan, 2000) Kipphan, H., 2000. *Handbook of print media*. Germany: Springer.

(Knobloch, 2003) Knobloch, A., 2003. *Mikroelektronikschaltungen aus gedruckten Polymeren*. PhD Thesis. Friedrich Alexander Universitaet.

(Kollmorgen, 2010) Kollmorgen, C., 2010. *AKD servo drive datasheet*. Kollmorgen. Available online: www.kollmorgen.com [Accessed Sep. 2010].

(Konami et al, 2017) Konami, I., Yasunori, Y. & Shizuo, T., 2017. *Soft blanket gravure printing technology for finely patterned conductive layers on three-dimensional or curved surfaces*. Japanese journal of applied physics, 56(5S2), pp. 1-4.

(Krebs, 2009) Krebs, F. C., 2009. *Pad printing as a film forming technique for polymer solar cells*. Solar energy materials and solar cells, 93(4), pp. 484-490.

(Kuhn & Grün, 1942) Kuhn, W. & Grün, F., 1942. *Beziehungen zwischen elastischen Konstanten und Dehnungsdoppelbrechung hochelastischer Stoffe*. Colloid & polymer science, 101(3), pp. 248-271.

(Kuscharski, 2017) Kuscharski, T., 2017. *Tampondruckmaschinen-Aufbau und Unterschiede*. Innovation Tampondruck Seminar. Bietigheim Bissingen, Germany. Oct. 2017.

(Levassort et al, 2006a) Levassort, F., Filoux, E., Lethiecq, M., Lou-Moler, R., Ringgaard, E. & Nowicki, A., 2006a. *P3Q-3 curved piezoelectric thick films for high resolution medical imaging*. Ultrasonics symposium, IEEE. Oct. 2006.

(Levassort et al, 2006b) Levassort, F., Filoux, E., Lethiecq, M., Lou-Moler, R., Ringgaard, E. & Nowicki, A., 2006b. *P3Q-3 Curved Piezoelectric Thick Films for High Resolution Medical Imaging*. Ultrasonics Symposium, 2006. IEEE. 2-6 Oct. 2006.

(Li et al, 2017) Li, J., Yan, X., Zhu, B., Xu, J., Ou-Yang, J. & Yang, X., 2017. *Synthesis of cylindrically-concaved PMN–PT thick films by pad printing process*. Journal of alloys and compounds, 695 (Supplement C), pp. 859-862.

(Loukil et al, 2018) Loukil, M. T., Corvec, G., Robin, E., Miroir, M., Le Cam, J. B. & Garnier, P., 2018. *Stored energy accompanying cyclic deformation of filled rubber*. European polymer journal, 98, pp. 448-455.

(Lück, 2017a) Lück, J. P., 2017a. *Drucktampons Seminar*. Innovation Tampondruck Seminar. Bietigheim Bissingen, Germany. Oct. 2017.

(Lück, 2017b) Lück, J. P., 2017b. *High performance printing pads*. Tampo-technik GmbH. [Gesamtkatalog]. Available online: http://katalog.tampotechnik.de/ [Accessed Jun. 2018].

(Mansouri et al, 2017) Mansouri, M. R., Darijani, H. & Baghani, M., 2017. *On the correlation of FEM and experiments for hyperelastic elastomers*. Experimental mechanics, 57(2), pp. 195-206.

(McClellan, 1997) McClellan, M., 1997. *Applying manufacturing execution systems.*CRC Press.

(Merilampi et al, 2011) Merilampi, S., Björninen, T., Ukkonen, L., Ruuskanen, P. & Sydänheimo, L., 2011. *Characterization of UHF RFID tags fabricated*

directly on convex surfaces by pad printing. The international journal of advanced manufacturing technology, 53(5-8), pp. 577-591.

(Meyer et al, 2009) Meyer, H., Fuchs, F. & Thiel, K., 2009. *Manufacturing execution systems (MES): Optimal design, planning, and deployment.* New York: McGraw Hill.

(Micro Print, 2012) Micro Print, C., 2012. *Pad printing book.* Schaffhausen: Micro print LC GmbH.

(Micro Print, 2014) Micro Print, C., 2014. *Pad printing catalog*. Micro print LC GmbH. Available online: http://www.microprint.ch/pdf/Padprintingcatalog.pdf [Accessed March. 2015].

(Morlock, 2018) Morlock, 2018. *Printing pads*. Available online: http://www.morlock.de/cms/attachments/Tamponkatalog.pdf [Accessed March. 2018.

(Morlock, 2012) Morlock, T., 2012. *Tampondruck GFG 100.* Dornstetten: ITW MORLOCK GmbH.

(National Instruments, 2012a) National Instruments, T., 2012a. *Applications for EtherCAT RIO*. National Instruments. Available online: http://www.ni.com /white-paper/14083/en/ [Accessed March. 2015].

(National Instruments, 2012b) National Instruments, T., 2012b. *NI EtherCAT RIO: Deterministic expansion for LabVIEW RIO systems.* National Instruments. Available online: http://www.ni.com/white-paper/7299/en/ [Accessed Apr. 2015].

(National Instruments, 2014) National Instruments, T., 2014. *CompactRIO integrated systems with real-time controller and reconfigurable chassis NI cRIO-907x.* National Instruments. Available online: http://sine.ni.com/ds/app/doc/p/id/ds-204/lang/en [Accessed March. 2015].

(Proell, 2014) Proell, T., 2014. *Pad printing theory and practice.* Weissenburg: Proell company.

(Pudas, 2002) Pudas, M., 2002. *Gravure-offset printing in the manufacture of ultra-fine-line thick films for electronics*. PhD thesis. University of Oulu.

(Pudas et al, 2004) Pudas, M., Hagberg, J. & Leppävuori, S., 2004. *Printing parameters and ink components affecting ultra-fine-line gravure-offset printing for electronics applications*. Journal of the european ceramic society, 24(10), pp. 2943-2950.

(Putnam et al, 1988) Putnam, T. P., Sunter, R. A., Kearney, D. A. & Lothrop, R. J., 1988. *Programmable pad printing apparatus and method*. Google Patents.

(Raupach, 2016) Raupach, B., 2016. *Extensometers*. Oct. 2016, email.

(Robles et al, 2015) Robles, T., Alcarria, R., Martın, D., Navarro, M., Calero, R., Iglesias, S. & López, M., 2015. *An IoT based reference architecture for smart water management processes*. Journal of wireless mobile networks, ubiquitous computing, and dependable applications (JoWUA), 6(1), pp. 4-23.

(SAS, 2013) SAS, I., 2013. *ANSYS mechanical APDL theory reference.*

(Schoinas et al, 2017) Schoinas, S., Guamra, A.-M. E., Moreillon, F. & Passeraub, P., 2017. *A flexible pad-printed fluxgate sensor*. Eurosensors. Paris, Sep. 2017. Multidisciplinary digital publishing institute (MDPI). pp. 1-4.

(Shahzad et al, 2015) Shahzad, M., Kamran, A., Siddiqui, M. Z. & Farhan, M., 2015. *Mechanical characterization and FE modelling of a hyperelastic material*. Materials research, 18(5), pp. 918-924.

(Sharp, 2013) Sharp, D., 2013. *Printed composite electrodes for in-situ wound pH monitoring*. Biosensors and bioelectronics, 50(1), pp. 399-405.

(Shen et al, 2017) Shen, Y. H., Cheng, H. C., Chen, Y. W., Lu, S. T., Lin, S. M. & Chen, W. H., 2017. *Temperature effects on ink transfer performance of gravure offset printing for fine-line circuitry*. International conference on electronics packaging (ICEP). Apr. 2017. pp. 475-478.

(Simulia, 2013a) Simulia, A. V., 2013a. *6.13 Documentation.* Dassault systemes.

(Simulia, 2013b) Simulia, A. V., 2013b. *Hyperelasticity, 6.13 Documentation*. Dassault systemes.

(Steinmann et al, 2012) Steinmann, P., Hossain, M. & Possart, G., 2012. *Hyperelastic models for rubber-like materials: Consistent tangent operators and suitability for Treloar's data*. Archive of applied mechanics, 82(9), pp. 1183-1217.

(Taik-Min et al, 2010) Taik-Min, L., Seung-Hyun, L., Jae-Ho, N., Dong-Soo, K. & Sangki, C., 2010. *The effect of shear force on ink transfer in gravure offset printing*. Journal of micromechanics and microengineering, 20(12), pp. 1-8.

(TampoCanada, 2018) TampoCanada, 2018. *Pad printing vs. screen printing – the differences explained.* Tampo Canada Inc. Available online: https://www.tampocanada.com/pad-printing-vs-screen-printing [Accessed Aug. 2018].

(Tampoprint, 2018) Tampoprint, 2018. *Pad database*. Korntal-Münchingen: TAMPOPRINT AG. Available online: https://www.tampoprint.de/en/support /pad-database.html [Accessed Jun. 2018].

(Tampoprint, 2014) Tampoprint, C., 2014. *Pad printing machines*. TAMPOPRINT AG. Available online: http://www.tampoprint.de/en/download_en/pdf_en /brochuren_en/tsm_serie_2014_web_en.pdf [Accessed Sep. 2014].

(Tzafestas, 2010) Tzafestas, S. G., 2010. *Human and Nature Minding Automation.*Springer.

(Ücüncü, 2015) Ücüncü, M. A., 2015. *Untersuchung der Einflussparameter auf das Drucken von Strukturen mittels indirektem Tiefdruck*. M.Sc. Thesis, Supervisor: Arash Hakimi-Tehrani. Technische Universität Darmstadt, May 2015.

(Wacker, 2018) Wacker, 2018. *Technical data sheet for ELASTOSIL RT 623 A/B*. [Technical data sheet]. Wacker chemie AG. Available online: https://www.wacker.com/cms/en/products/product/product.jsp?product=10467 [Accessed Feb. 2018].

(Wada et al, 2018) Wada, S., Zhang, R., Mannava, S. R., Vasudevan, V. K. & Qian, D., 2018. *Simulation-based prediction of cyclic failure in rubbery materials using nonlinear space-time finite element method coupled with continuum damage mechanics*. Finite elements in analysis and design, 138 (Supplement C), pp. 21-30.

(Wu et al, 2018) Wu, J., Zhang, C., Su, B., Dong, J., Wang, Y. & Gond, B. K., 2018. *New method for studying the macro-micro contact properties between smooth metal and silicone rubber*. The international journal of advanced manufacturing technology, 96(5), pp. 1761-1767.

(Xenos et al, 2015) Xenos, D. P., Cicciotti, M., Kopanos, G. M., Bouaswaig, A. E. F., Kahrs, O., Martinez-Botas, R. & Thornhill, N. F., 2015. *Optimization of a network of compressors in parallel: Real Time Optimization (RTO) of compressors in chemical plants – An industrial case study*. Journal of applied energy, 144(1), pp. 51-63.

(Ye & Zengchao, 2011) Ye, X. & Zengchao, Q., 2011. *Antenna 3D pad printing solution evaluation*. IEEE international symposium on antennas and propagation (APSURSI). Jul. 2011. pp. 2773-2776.

(Zwick, 2018) Zwick, 2018. *Calibration and accuracy in accordance with ISO 7500-1*. Zwick company. Available online: http://www.zwick.si/sl/produkti/xforce-load-cells/calibration-and-accuracy.html [Accessed Apr. 2018].

Own publications

Recent publications:

Arash Hakimi Tehrani, Edgar Dörsam, Jann Neumann, "Improving Automation and Process Control of an Indirect Gravure (pad) Printing Machine", Journal of Applied Sciences, Acta Polytechnica Hungarica, Vol. 13, No. 4, 2016.

Jian Chen, Edgar Dörsam, Dieter Spiehl, Arash Hakimi Tehrani, "Elastic model of paper stacks by considering the paper structure", Nordic Pulp & Paper Research Journal (NPPRJ), Vol. 31, No. 4, 2016.

Jian Chen, Edgar Dörsam, Dieter Spiehl, Arash Hakimi Tehrani, Jun Da, "Stress-strain behavior of paper affected by the actual contact area", Progress in Paper Physics Seminar, Germany, 2016.

Former publications:

Arash Hakimi Tehrani, "Studying on the tidal power stations and different kinds of tidal power turbines", Conference on Electrical Engineering Technology (TEEC 2008), Iran, 2008.

Arash Hakimi Tehrani, Ghazanfar Shahgholian, Sepehr Moalem, "Control of electrical motor maximum speed in two-mass resonance ratio controller by fuzzy self-organized Controller ", 1st Regional Conference on Research in Electrical Technology (RETC 2010), Iran, 2010.

Arash Hakimi Tehrani, Mohamad Ali Zanjani, "Harmonic effects of power factor correction capacitors", 2nd National Electrical Engineering Conference (NEEC 2010), Iran, 2010.

Arash Hakimi Tehrani, Jawad Faiz, Ghazanfar Shahgholian, "Simulation and operational results of DPFC", 3rd National Electrical Engineering Conference (NEEC 2012), Iran, 2012.

Arash Hakimi Tehrani, Jawad Faiz, Ghazanfar Shahgholian, "Operational comparing of PID and fuzzy controllers for wind turbine", 3rd National Electrical Engineering Conference (NEEC 2012), Iran, 2012.

Jawad Faiz, Arash Hakimi Tehrani, Ghazanfar Shahgholian, "Current control techniques for wind turbines - A Review", ELECTROMOTION Journal, Vol. 19, No. 3-4, 2012.

Jawad Faiz, Arash Hakimi Tehrani, Ghazanfar Shahgholian, Amir M. Takbash, "Speed Control of Wind Turbine through Pitch Control Using Different Control Techniques", Journal of Renewable Energy and Environment, Vol. 3, No. 2, 2016.

Supervised student projects

Master thesis

Meliksah Ücüncü: Untersuchung der Einflussparameter auf das Drucken von Strukturen mittels indirektem Tiefdruck. Engl. Investigation of influence parameters on printing of structures by means of indirect gravure printing. May 2015. Supervisor: Arash Hakimi Tehrani

Advanced design project

Benedikt Fertig, Daniel Höh-Zaid, Matthias Müller, Simon Silge, Juliane Weitz, Sven Winter: Optimierung einer Zugprüfmaschiner mit videobasiertem Extensometer zur Untersuchung von additiven Zugproben. Engl. Optimization of a tensile test machine with video extensometer for tensile investigation of additive manufactured specimens. July 2017. Supervisor: Vinzenz Nienhaus and Arash Hakimi Tehrani.

Appendix

A1. Comparison of different hyperelastic material models of 6, 12 and 18 Shore A silicone rubber

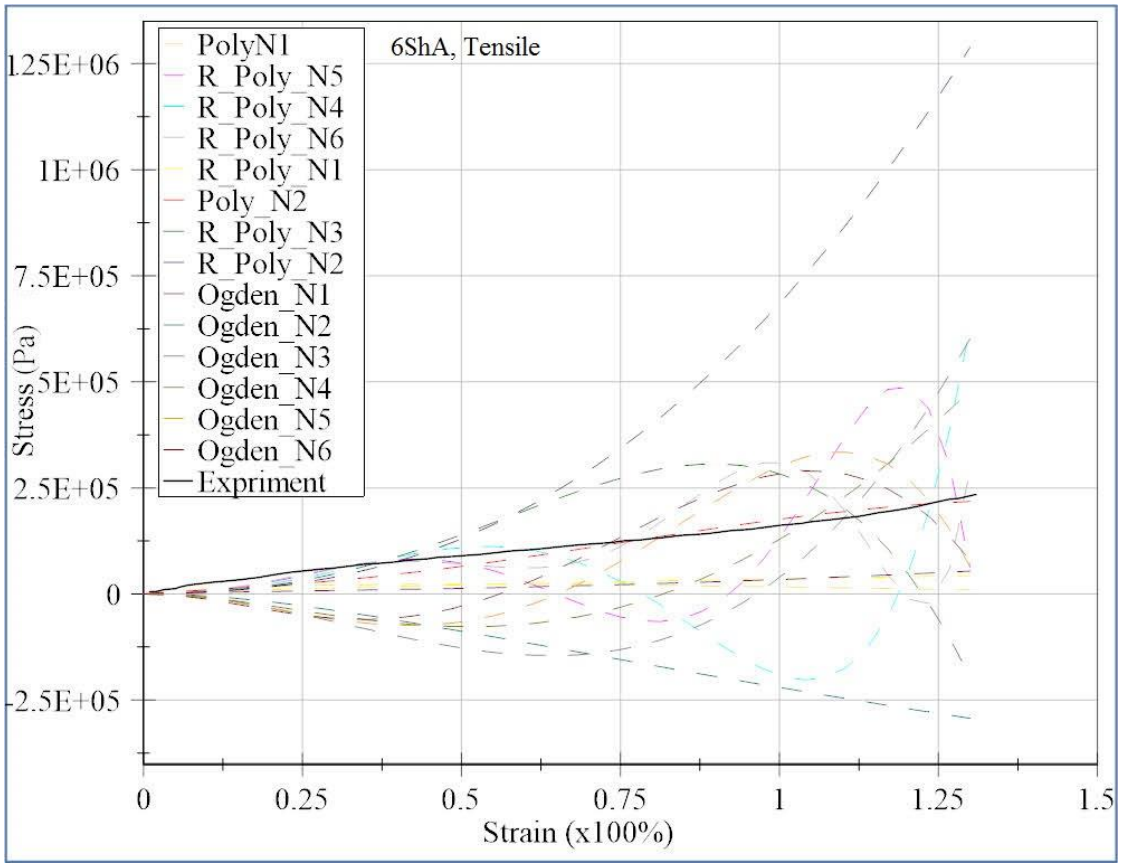

Figure A-1: The different hyperelastic material models in comparison with the uniaxial tensile experiment results of 6 Shore A silicone rubber. The stress-strain behavior of different models and related curves in uniaxial tensile behavior are described here. The black solid line is related to uniaxial tensile test results of 6 Shore A. The dashed lines describe different model results. The Poly_N2 (red dashed line) is the nearest model to experiment results, in this case.

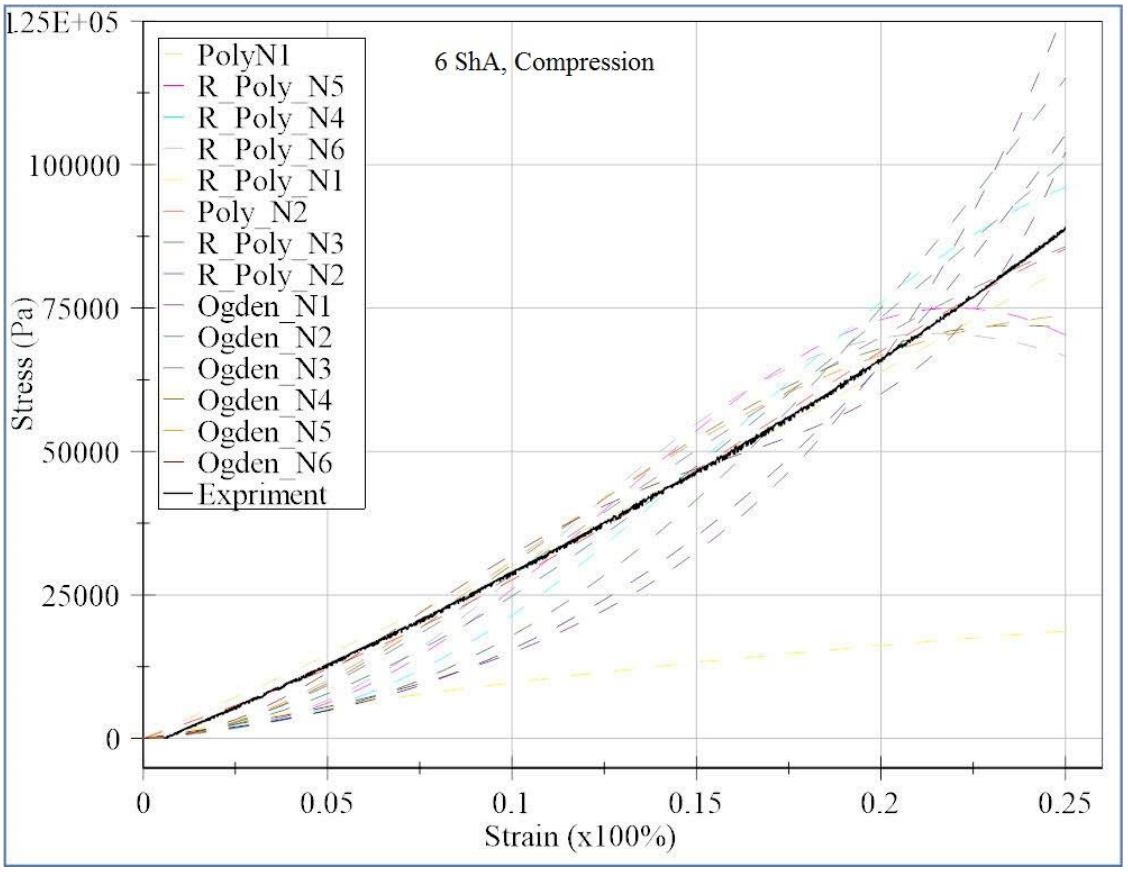

Figure A-2: The different hyperelastic material models in comparison with the compression test results of 6 Shore A silicone rubber. The stress-strain behavior of different models and related curves in compression behavior are described here. The black solid line is related to uniaxial compression test results of 6 Shore A. The dashed lines describe different model results. The Poly_N2 (red dashed line) is the nearest model to experiment results, in this case.

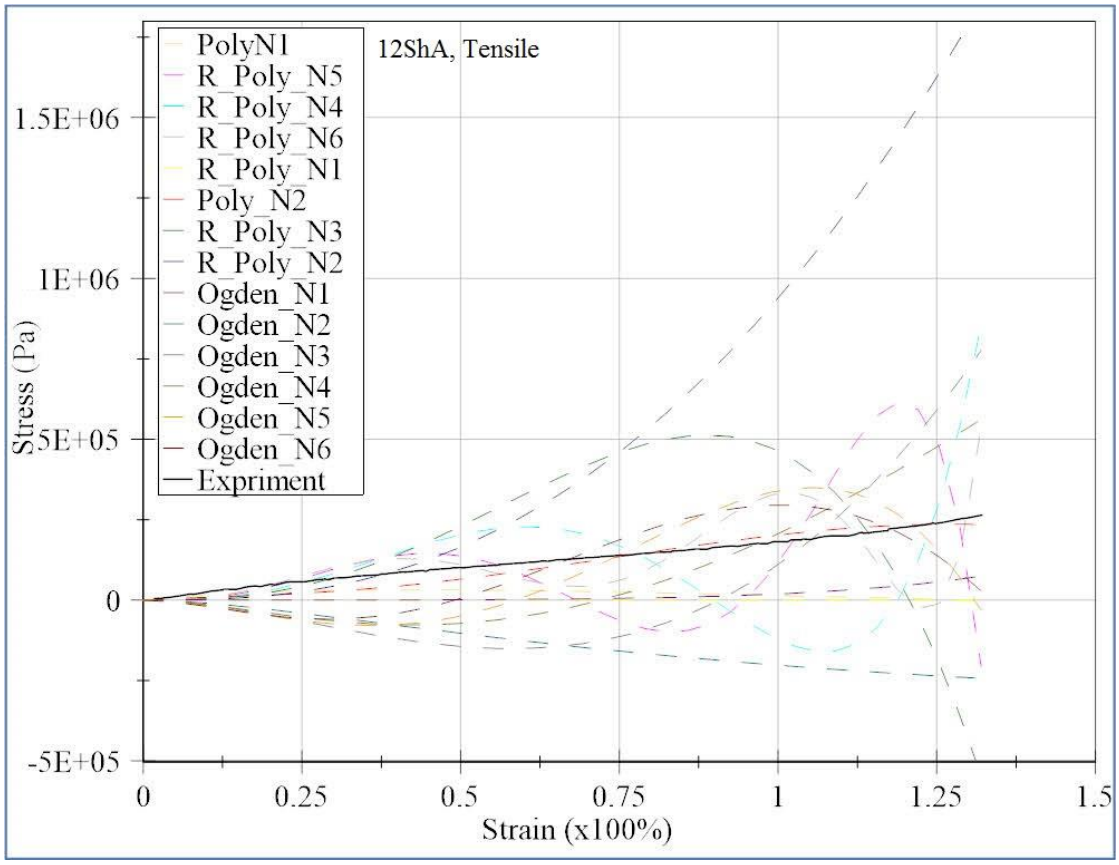

Figure A-3: The uniaxial tensile test results and the hyperelastic material models of 12 Shore A silicone rubber. The stress-strain behavior of different models and related curves in uniaxial tensile behavior are described here. The black solid line is related to uniaxial tensile test results of 12 Shore A. The dashed lines describe different model results. The Poly_N2 (red dashed line) is the nearest model to experiment results, in this case.

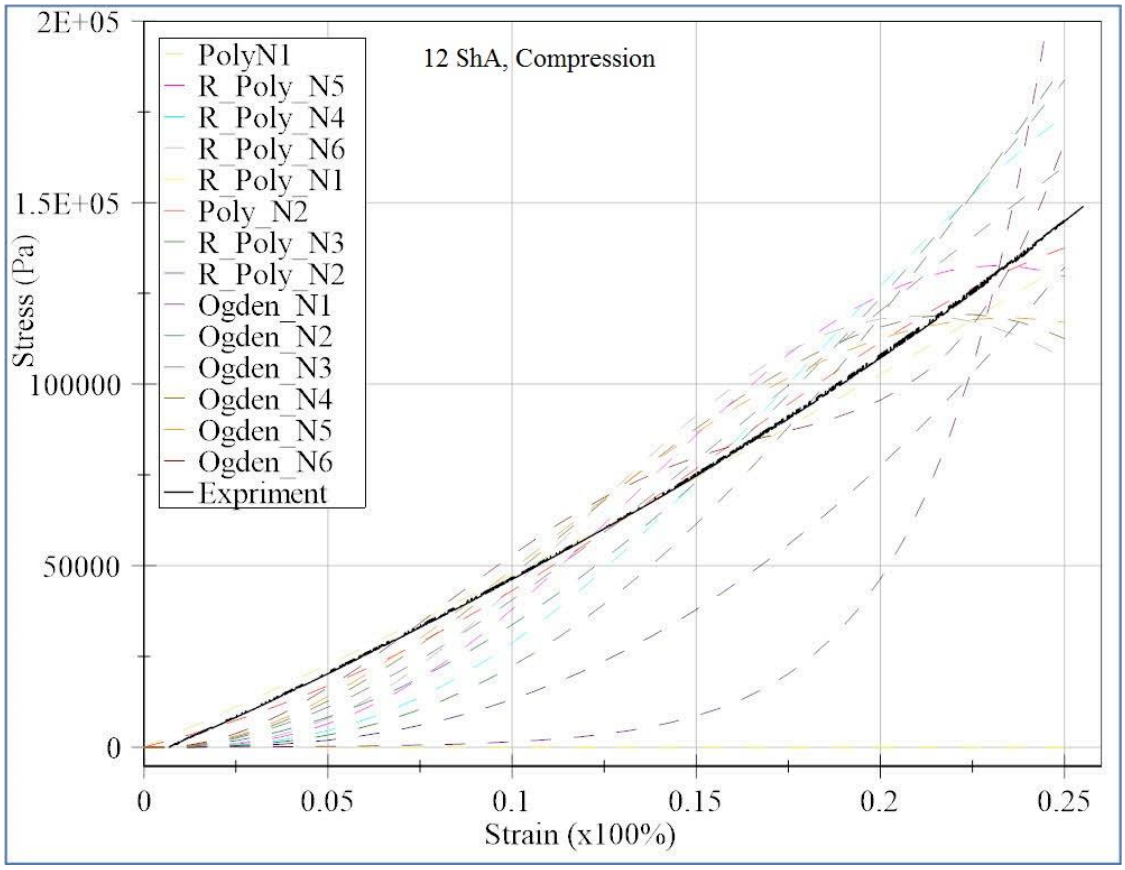

Figure A-4: The different hyperelastic material models in comparison with the compression test results of 12 Shore A. The stress-strain behavior of different models and related curves in compression behavior are described here. The black solid line is related to compression test results of 12 Shore A. The dashed lines describe different model results. The Poly_N2 (red dashed line) is the nearest model to experiment results, in this case.

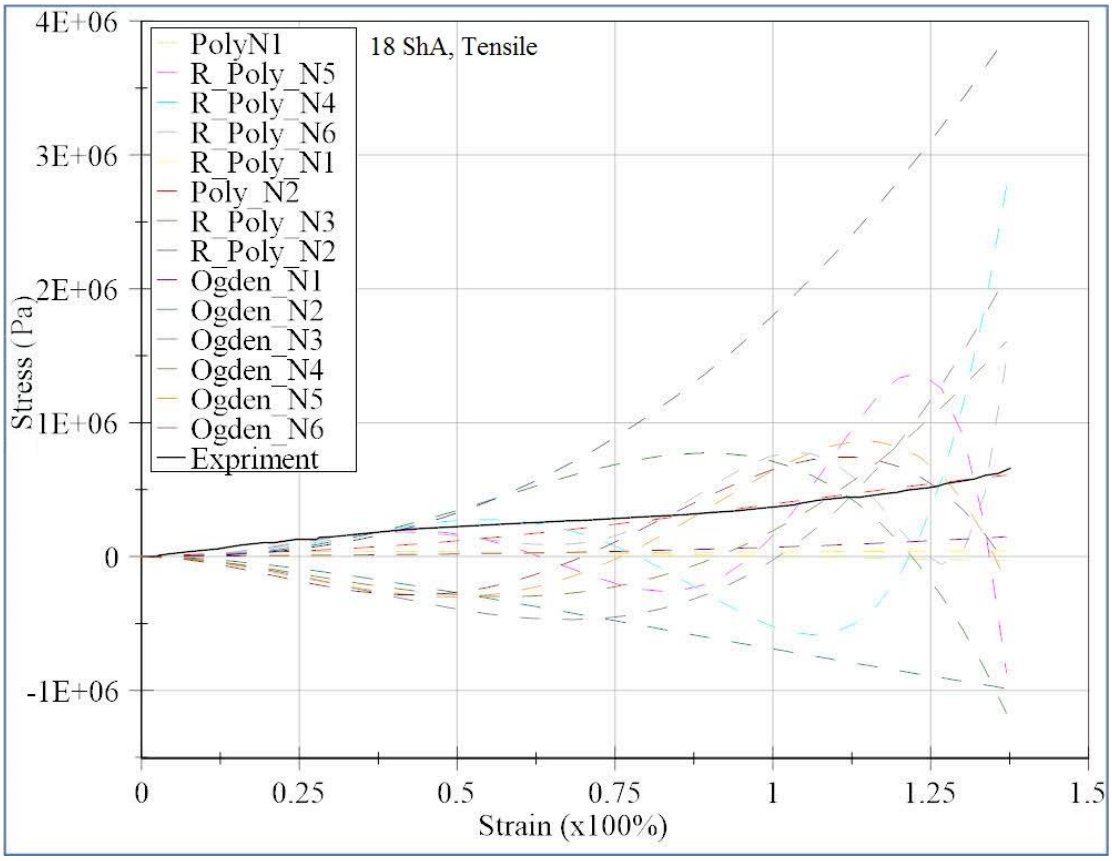

Figure A-5: The different hyperelastic material models and the uniaxial tensile experiment results of 18 Shore A silicone rubber. The stress-strain behavior of different models and test results in tension status are described here. The black solid line is related to uniaxial tensile test results of 18 Shore A. The dashed lines describe different model results. The Poly_N2 (red dashed line) is the nearest model to experiment results, in this case.

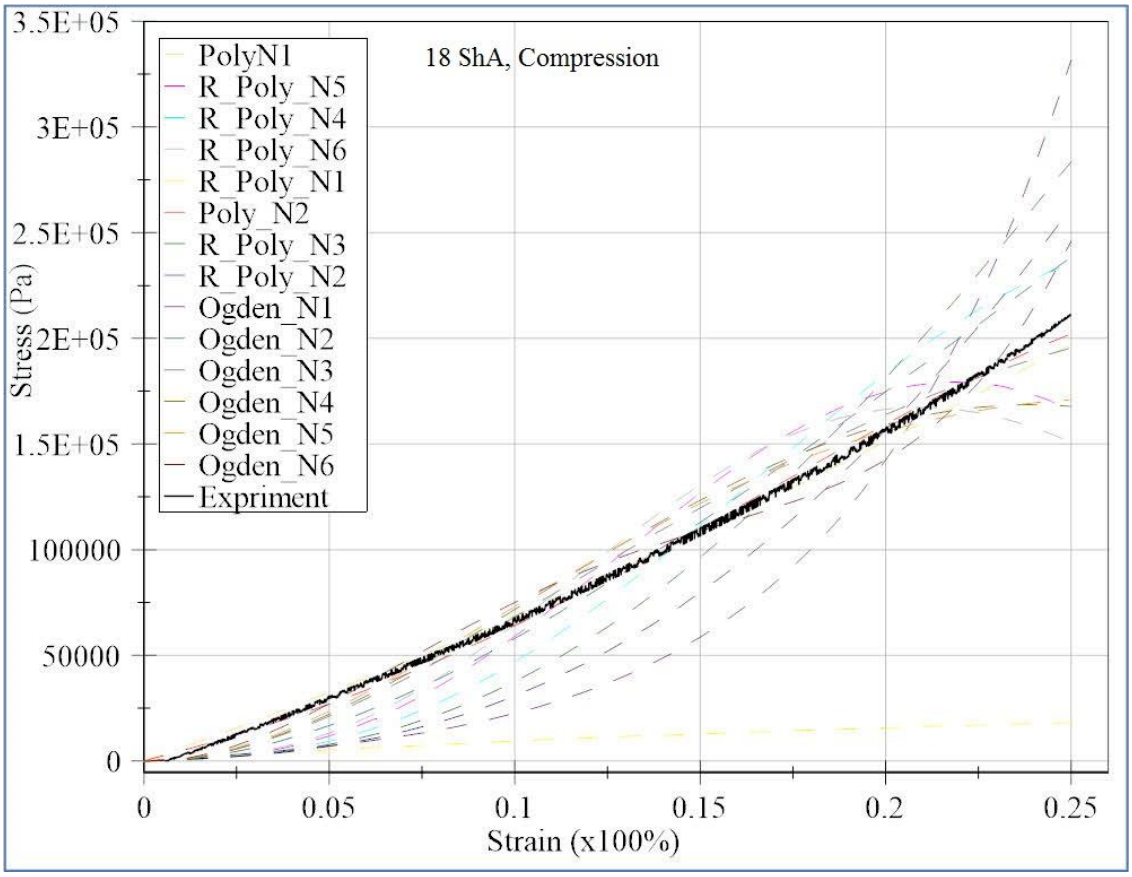

Figure A-6: The different hyperelastic material models and the compression test results of 18 Shore A silicone rubber. The stress-strain behavior of different models and test results in compression position are described here.The compression test results of 18 Shore A is shown with a black solid line. The dashed lines describe different model results. The Poly_N2 (red dashed line) is the nearest model to experiment results, in this case.

A2. Pad calculator program structure